STRUCTURAL PHASE TRANSITIONS AND PHONON ANOMALIES IN ALKALINE NIOBATE BASED FUNCTIONAL MATERIALS

By

MRINAL JAUHARI

PHYS01201504026

BHABHA ATOMIC RESEARCH CENTRE, MUMBAI

A thesis submitted to the

Board of Studies in Physical Sciences

In partial fulfilment of requirements

for the Degree of

DOCTOR OF PHILOSOPHY

of

HOMI BHABHA NATIONAL INSTITUTE

December 2019

Homi Bhabha National Institute

Recommendations of the Viva Voce Committee

As members of the Viva Voce Committee, we certify that we have read the dissertation prepared by Mr. Mrinal Jauhari entitled "Structural Phase Transitions and Phonon Anomalies in Alkaline Niobate Based Functional Materials" and recommend that it may be accepted as fulfilling the thesis requirement for the award of Degree of Doctor of Philosophy.

Chairman – Dr. S. L. Chaplot	S. L. Chaplot 29-09-2020.
Guide / Convener – Dr. R. Mittal	Ranjan Mittal
Examiner - Prof. Rajeev Ranjan	Rajeev
Member 1- Dr. P. U. Sastry	PUSastry
Member 2- Dr. S. N. Achary	S. N. Achary
Member 3- Dr. P. D. Babu	

Final approval and acceptance of this thesis is contingent upon the candidate's submission of the final copies of the thesis to HBNI.

I hereby certify that I have read this thesis prepared under my direction and recommend that it may be accepted as fulfilling the thesis requirement.

Date: 01.10.2020

Place: MUMBAI

Signature Ranjan Mittal

Guide R. MITTAL

Homi Bhabha National Institute

Recommendations of the Viva Voce Committee

As members of the Viva Voce Committee, we certify that we have read the dissertation prepared by Mr. Mrinal Jauhari entitled "Structural Phase Transitions and Phonon Anomalies in Alkaline Niobate Based Functional Materials" and recommend that it may be accepted as fulfilling the thesis requirement for the award of Degree of Doctor of Philosophy.

Chairman – Dr. S. L. Chaplot	S. L. Chaplot 29-09-2020.
Guide / Convener – Dr. R. Mittal	Ranjan Mittal
Examiner - Prof. Rajeev Ranjan	Rajeev
Member 1- Dr. P. U. Sastry	PUSastry
Member 2- Dr. S. N. Achary	S. N. Achary
Member 3- Dr. P. D. Babu	

Final approval and acceptance of this thesis is contingent upon the candidate's submission of the final copies of the thesis to HBNI.

I hereby certify that I have read this thesis prepared under my direction and recommend that it may be accepted as fulfilling the thesis requirement.

Date: 01.10.2020

Place: MUMBAI

Signature Ranjan Mittal

Guide R. MITTAL

STATEMENT BY AUTHOR

This dissertation has been submitted in partial fulfilment of requirements for an advanced degree at Homi Bhabha National Institute (HBNI) and is deposited in the Library to be made available to borrowers under rules of the HBNI.

Brief quotations from this dissertation are allowable without special permission, provided that accurate acknowledgement of source is made. Requests for permission for extended quotation from or reproduction of this manuscript in whole or in part may be granted by the Competent Authority of HBNI when in his or her judgment the proposed use of the material is in the interests of scholarship. In all other instances, however, permission must be obtained from the author.

MRINAL JAUHARI
(PHYS01201504026)

DECLARATION

I, hereby declare that the investigation presented in the thesis has been carried out by me. The work is original and has not been submitted earlier as a whole or in part for a degree / diploma at this or any other Institution / University.

MRINAL JAUHARI

(PHYS01201504026)

DECLARATION

I, hereby declare that the queries raised by the examiners of the thesis as well as the corrections suggested by examiners have been incorporated.

Ranjan Mittal
29.9.2020

Ranjan Mittal

(Guide)

List of Publications arising from the Thesis

Journals:

1) "Effect of chemical pressure on competition and cooperation between polar and antiferrodistortive distortions in sodium niobate", **Mrinal Jauhari**, S. K. Mishra, R. Mittal, P. U. Sastry, S. L. Chaplot; Physical Review Materials, 2017, 1, 074411.
2) "Evidence for existence of functional monoclinic phase in sodium niobate based solid solution by powder neutron diffraction", S. K. Mishra, **Mrinal Jauhari**, R. Mittal, P. S. R. Krishna, V. R. Reddy, and S. L. Chaplot; Appl. Phys. Lett., 2018, 112, 182905
3) "Probing of structural phase transitions in barium titanate modified sodium niobate using Raman scattering" **Mrinal Jauhari**, S. K. Mishra, R. Mittal and S. L. Chaplot; J. Raman Spectrosc.2019; 50:1177- 1185, doi.org/10.1002/jrs.5618
4) "Evidence of low-temperature phase transition in $BaTiO_3$ modified $NaNbO_3$: Raman Spectroscopy Study", **Mrinal Jauhari**, S. K. Mishra, H. K. Poswal, R. Mittal and S. L. Chaplot, J. Raman Spectrosc.2019; 50:1949-1955. doi.org/10.1002/jrs.5739

Conferences:

1) "Effect of $BiFeO_3$ doping in $KNbO_3$", **Mrinal Jauhari**, S. K. Mishra, R. Mittal, S. L. Chaplot; 16th Asia Oceania Neutron Scattering Association (AONSA) School, Mumbai, India [15-19 November, 2016].
2) "High-temperature neutron diffraction study of modified $KNbO_3$", **Mrinal Jauhari**, S. K. Mishra, R. Mittal, S. L. Chaplot; 6th Conference on Neutron Scattering, Mumbai, India [21-23rd November, 2016].

3) " Structural and dielectric studies of modified $KNbO_3$", **Mrinal Jauhari**, S. K. Mishra, R. Mittal, S. L. Chaplot; DAE Solid State Physics Symposium, Bhubaneswar, India [26-30th December 2016].

4) "Effect of chemical pressure on phase stability of $NaNbO_3$", **Mrinal Jauhari**, S. K. Mishra, R. Mittal, Rekha Rao, S. L. Chaplot; DAE Solid State Physics Symposium, Mumbai, India [26-30th December, 2017].

5) "Low-temperature Structural Phase Transitions in Lead-Free Piezo-ceramic NNBT10", **Mrinal Jauhari**, S. K. Mishra, H. K. Poswal, R. Mittal, Rekha Rao, S. L. Chaplot; 47th National Seminar on Crystallography, Mumbai, India [19-22nd June, 2019].

MRINAL JAUHARI
(PHYS01201504026)

Dedicated to my Guide.

ACKNOWLEDGEMENTS

I would like to express my deepest gratitude to my Ph. D. guide Dr. Ranjan Mittal, for his valuable guidance, patience, encouragement given to me in carrying out research work. Apart from the technical knowledge, the discipline, which I learned from my guide is indispensable to my growth as a researcher and as a person. I considered myself to be honoured and fortunate to be associated with him.

Besides my guide, I would like to thanks to Dr. S. K. Mishra for introducing me to the world of crystallography and performing Rietveld refinements. Without his precious support, it would not have been a wonderful journey for me to conduct this research. He has been a great inspiration throughout this work. I would like to express thanks to Mr. P. S. R. Krishna and Mr. A. B. Shinde for providing the good quality neutron diffraction data from Dhruva Reactor Facility, Bhabha Atomic Research Centre. I also want to express thanks to Mr. Jayakrishnan V. B., Mr. Swayam Kesari and Dr. Himanshu Kumar Poswal for the help during the X-ray diffraction and Raman spectroscopic measurements. I would like to thank our collaborator, Dr. V. R. Reddy for low-temperature ferroelectric loop measurements.

I am greatful for my doctoral committee members: Chairman of the committee Dr. S. L. Chaplot, Dr. P. U. Sastry, Dr. P. D. Babu, Dr. S. N. Achary for their insightful comments and encouragement, but also the hard questions, which incented me to widen my research from various perspectives.

I sincerely thank my all teachers who taught me various lessions at different stage of life. I want to specially thank to Dr. A. K. Ray, Dr. S. Sinha, Dr. S. Kundu, Dr. S. R. Jain, and Dr. Zafar Ahmad to share their personal experiences and help in taking various decisions.

I convey my heartfelt thank to Dr. Saibal Basu for immense help in chosing the project and revival of SRF fellowship stopped due to some technical issues.

I sincerely thank to Dr. S. M. Yusuf for constant support and encouragement in carrying out the research work and help during the various administrative works.

My research would never be completed without the cooperation and support of my friends and Seniors, Dr. Utpal Dutta, Dr. Nirmalendu Patra, Dr. Raman Khurana, Dr. Avinash Singh, Dr. Ananya Kundu, Mrs. Poornima Gupta, Ms. Ankita Pathak, Mr. Vikas Dhiman, Mr. Poojan Gharat, Mr. Madan , Mr. Vashram, Mrs. P. S. Kamble, Mrs. Shabana Khan, Dr. Mayanak Gupta, Dr. Baltej Singh, Dr. Charanpreet Kaur, Mr. Pulkit Prakash, Mr. Purushottam Dubey, Mr. Harish S., Mr. Harsh Bhatt, Mr. Ankur, Ms. Madhu Ghanate, Dr. Yogesh Kumar, Dr. Anup Bera, Mr. Rahul Kumar, Mr. Vinod B., Dr. A. Shelke, Dr. Virendra Sharma, Dr. Amit Kumar, Mr. Rohit Chandak, Dr. P. S. Goyal, and other friends and staff members for the many fruitful discussions and merry memories.

I would like to thank all Homi Bhabha National Institute Dean, Academic Dean, administration and staff members for their constant cooperation in all administrative activities related to my PhD.

Thanks all for your encouragement and motivation. This journey would not have been completed without every each one of you.

TABLE OF CONTENT

Chapter 1: Introduction and Litrature Review

Materials possess intrinsic functional properties such as piezoelectricity, ferroelectricity, magnetism or energy storage, etc. are called functional materials. We are dealing with piezoelectric materials. These convert the mechanical energy to electrical energy and vice versa[8-10]. The phenomena of accumulation of charge on the surface of the piezoelectric materials due to mechanical pressure is called direct piezoelectric effect [11]. The reverse effect in which the application of external electric field changes the dimensions of the piezoelectric body is called inverse piezoelectric effect. Piezoelectricity occurs in only those crystals which possess the non-centrosymmetric structure i.e. the atomic arrangement in the crystals doesn't have a centre of inversion[11]. Hence, piezoelectricity has a direct link with the structure of the piezoelectric crystals.

On the application point of view, these materials can be classified in the four main categories as actuator, sensors, transducers, and generators in various devices such as mobile phones, microphones, sonar, accelerometer, fuel jet valves, piezoelectric motors, transformers, non-volatile RAM, and energy harvesting devices [11-13]. These piezoelectric devices have a global market of about 38.4 billion US dollars by 2017 with the compound annual growth rate of 13.2 % [14].

Piezoelectric materials along with their subclasses such as pyroelectrics and ferroelectrics provide a prospect of materials that can harvest energy from multiple sources including vibration, thermal fluctuations, and light. Piezoelectric materials are dominant in the market are lead-based such as lead zirconate titanate PZT: $Pb_{(x)}Zr_{(1-x)}TiO_3$, PMN-xPT: (1-x)$PbMn_{(1/3)}Nb_{(2/3)}O_3$-$x$$PbTiO_3$, and PZN-$x$PT: (1-x)$PbZn_{1/2}Nb_{1/2}O_3$-x$PbTiO_3$ are the most dominating in technological applications due to their best piezoelectric performance[2, 11, 15-

19]. Lead is a toxic element and contaminates the environment due to the volatile nature of lead oxide (PbO_2) during material processing[2, 16]. Lead oxide remains in the air for a long time. It accumulates in the human body and causes various diseases[2, 17]. Due to these disadvantages, many countries have taken legal initiation to ban these lead-based products[20]. To overcome these issues, there is a need to develop an environment-friendly piezoelectric material.

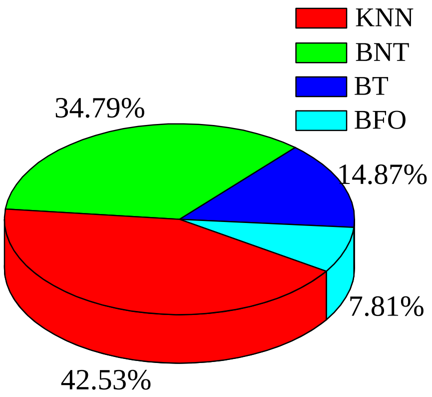

Figure 1.1 Publications on lead-free piezoelectric materials in the period 2000-2017[10].

Various lead -free piezoelectric materials such as $Na_{0.5}Bi_{0.5}TiO_3$ (NBT), $K_{0.5}Bi_{0.5}TiO_3$ (KBT), $K_{1/2}Na_{1/2}NbO_3$ (KNN) and $BaTiO_3$ (BT) based systems are investigated most intensely in the past few years (see Figure 1.1)[2, 10, 17, 20-22]. However, the search to make them practically useful is continuing [23, 24]. The physical properties of these functional materials closely related to their crystal structures. These properties can be enhanced by tailoring the structure employing chemical substitution and by changing external conditions i.e. temperature, pressure, electric field, etc[2, 25, 26]. The knowledge of precise crystal structure and structural phase transitions remains a big challenge to understand the deep physical insight of enhanced electromechanical properties and to develop new high-performance piezoelectric materials[2, 5, 27]. Thus, understanding of the crystal structure is necessary to design new materials from a fundamental physicochemical perspective. In the present work, we have tried to identify the structural phase transitions in an alkaline niobate based solid solutions NNBT*x*: [(1-*x*)$NaNbO_3$-*x*$BaTiO_3$], which possess a perovskite structure.

1.1 Perovskites

Perovskites are the compounds which have general formula ABX_3, where 'A' is mostly an alkali or alkaline earth metal cation (with ionic charge 1+ or 2+), 'B' is a transition metal cation and 'X' is an anion (with ionic charge 4+ or 5+). The first naturally occurring perovskite $CaTiO_3$ was discovered in 1839 by the Russian mineralogist Gustav Rose and named after the Russian mineralogist Count Lev Alekseevich von Perovski [1, 28]. The importance of these compounds is due to their relatively simple crystal structure and enormously important physical properties such as dielectric, ferroelectric, ferroelastic, magnetic, and superconductivity, etc. Piezoelectricity in crystals is directly related with their crystal structure. Perovskite class of piezoelectric materials becomes fascinating after the discovery of important dielectric properties of the $BaTiO_3$ in early 1940s[1, 28]. It was discovered that the high permittivity of $BaTiO_3$ is due to ferroelectricity, which shows the highest value of permittivity near the ferroelectric transition[1, 11]. These materials come in the category of polar piezoelectrics, i.e. they show spontaneous polarization in absence of any electric field, and also show ferroelectricity. Ferroelectricity in the polar solids is property to switch the polarization on the application of the external electric field. All ferroelectric materials are piezoelectric but not all piezoelectrics are ferroelectric such as GaN (wurtzite structure) is polar and shows piezoelectricity but the polarization in this material can't be reversed by application of the external electric field[1, 8]. The particular advantage of polarization switching and simple crystal structure make perovskites the most fascinating materials for the search of exceptionally high functionality[1].

1.2 Perovskites Structure

The aristotype crystal structure of perovskites is cubic with space group $\mathbf{Pm\bar{3}m}$ and it is adopted by the room temperature phase of $SrTiO_3$[1, 8]. Atoms in this ideal cubic cell can be located in two general ways. In the first configuration, 'A' type atoms sit at the corner of the cubic unit cell and 'B' type cation occupies the body centred position. The oxygen atoms occupy the face centred positions (Figure 1.2).

A: 1*a* (0,0,0); **B**: 1*b* (½, ½, ½);

O: 3*c* (½, ½, 0), (½, 0, ½) and (0, ½, ½);

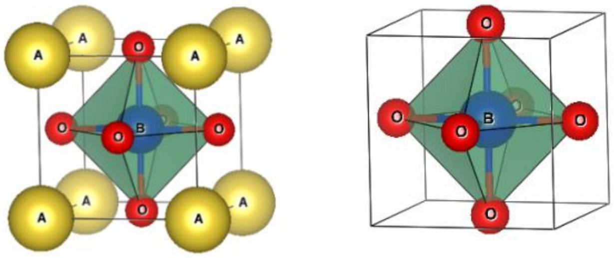

(a) **(b)**

Figure 1.2 (a) The first setting of the ABO_3 cubic unit cell and (b) centred oxygen octahedra BO_6.

In the second configuration, the 'A' type cation sits at the cell centre and coordinated by twelve O^{-2} ions (Figure 1.3).

A:1*b* (½, ½, ½); **B**:1*a* (0, 0, 0);

O:3*d* (½, 0, 0), (0, ½, 0) and (0, 0, ½);

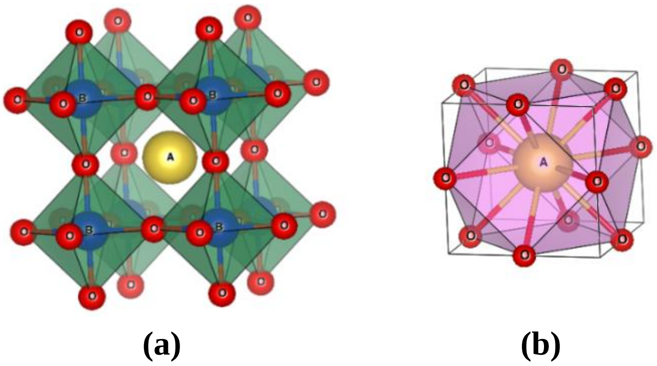

Figure 1.3 (a) The second conventional setting of the cubic unit cell and (b) AO_{12} polyhedra**.**

1.3 Structural Phase Transition (SPT) in Perovskite

In general, the phase transitions in the solid materials are accompanied by the structural changes, which means that the crystallographic configuration i.e. space group, lattice parameters, occupied positions, atomic coordinates, changes after phase transition[29]. The structural phase transitions in perovskites are mainly of two types namely, ferrodistortive and antiferrodistortive. In the case of **"ferrodistortive phase transitions",** the number of formula units (Z) in the primitive unit cell of the low symmetry phase is same as the number of formula units in the primitive unit cell of high symmetry (parent) phase. However, in the case of "**antiferrodistortive phase transitions",** the number of formula units (Z) in the primitive unit cell of the low symmetry phase is an integral multiple of the number of formula units in the primitive unit cell of the high symmetry phase[30]. These structural phase transitions in this ABO_3 system generally governed by the main three mechanisms as described below.

1.3.1 Cationic Displacement

When external perturbations (temperature, pressure and chemical composition) are applied to materials having a cubic perovskite structure, the cubic perovskite structure get slightly distorted in the sense that the cations ‘A’ or ‘B’ type (or both) get displaced from their original positions in a particular direction concerning oxygen octahedra (Figure 1.4).

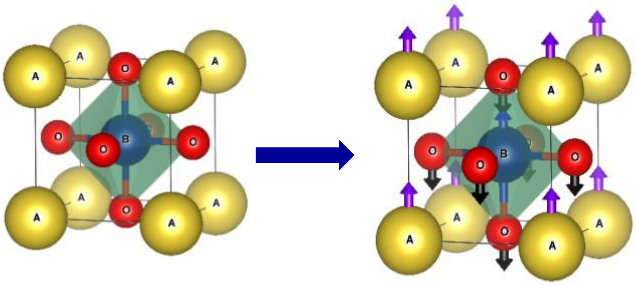

Figure 1.4 Schematic of the cubic to tetragonal phase transition in general ABO_3 compounds.

Due to the relative displacement of cations with respect to oxygen octahedra, the structure becomes non-centrosymmetric and acquires a spontaneous polarisation due to the formation of dipoles. However, the alignment of such electric dipoles leads to ferroelectric or antiferroelectric ordering in these materials. The ferroelectric structure adopts a non-centrosymmetric space group.

For example[1], in the case of $BaTiO_3$ the highest temperature cubic phase (a= 3.9732 Å) which contains equally bounded Ti^{+4} ions with oxygen O^{-2}.

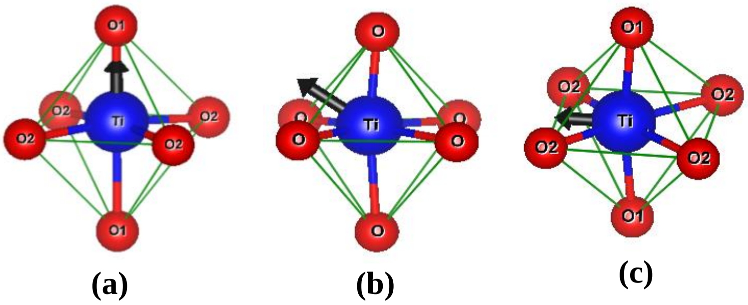

Figure 1.5 Cationic displacement in BO_6 octahedra along (a) tetrad axis, (b) triad axis [111] and (c) diad axis [011][1].

Below 393 K, the Ti^{+4} ions get displaced towards one of the oxygen atoms (along O1) from the centre of the unit cell, which leads to distortions of the oxygen octahedra due to cationic displacement as shown in Figure 1.5. This results the crystal structure transforms from cubic

$Pm\bar{3}m$ to tetragonal **P4mm** (a=b= 3.9910 Å, c= 4.0352 Å) and structure gets elongated along the c-axis. Due to the formation of electric dipoles, crystal acquires spontaneous polarization[31].

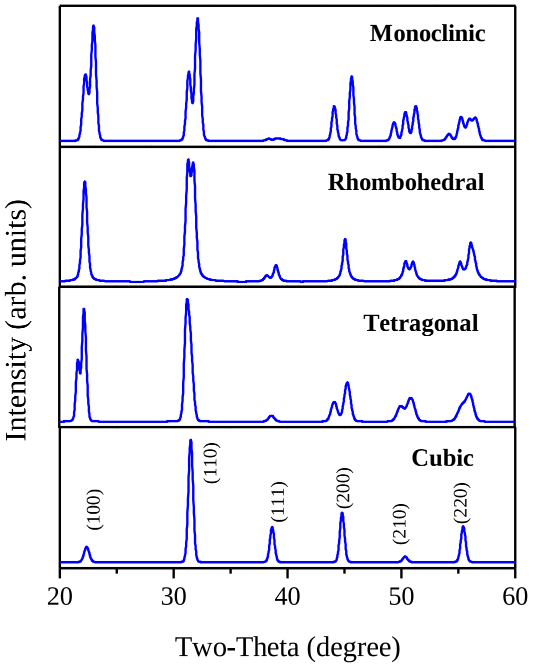

Splitting of the main perovskite reflection provides information about the lattice type.

Tetragonal / Orthorhombic distortion

h00 type ⇒ split into two
hhh type ⇒ singlet

Rhombohedral distortion

hhh type ⇒ split into two
h00 type ⇒ singlet

Monoclinic distortion

Splitting of both hhh and h00 reflections

Figure 1.6 A schematic representation of the splitting of the Bragg peaks in the diffraction patterns on changing the symmetry of the crystal structure in perovskites.

Other phase transitions on further lowering the temperature in $BaTiO_3$ also involve the same mechanism and the structure get transformed into orthorhombic (cationic displacement along triad axis) **Amm2** (at 268 K) and finally, structure becomes rhombohedral (cationic displacement along diad axis) with space group **R3m** at low temperature (T< 223 K).

These distortions are easily detected by the diffraction technique. Since the crystal structure becomes lower in symmetry and there is a change in the structural parameters. Therefore, these distortions lead to the splitting in the main perovskite peaks in diffractograms (see Figure 1.6). For example, a tetragonal distortion of the cubic unit cell would result in splitting of the h00 pseudo-cubic reflections into two but the hhh type of reflections would remain a singlet. Rhombohedral distortion, on the other hand, would lead to the splitting of the hhh type pseudo-cubic reflections into two while the h00 type reflections will remain a singlet. In the case of monoclinic distortion, we expect splitting of both the hhh and h00 reflections.

1.3.2 Rotation and/or Tilting of Oxygen Octahedra

The structure of perovskites can be considered as a rigid BO_6 octahedron joint with hinges at each corner with slight flexibility and there is a void in between the octahedra which contains ‘A’ type cation[1]. If the ‘A’ site cation is smaller than the void spacing and does not fit completely then the ideal cubic structure becomes unstable i.e. energetically unfavorable. In most of the cases of ABO_3 compounds, the structure does not retain in the ideal cubic symmetry at room temperature and the rigid BO_6 octahedra get tilted around any of the tetrad, triad and diad axes to reduce the free energy of the system and these rotations and/or tilting stabilizes the crystal structure[1]. These tilts lead to an increase in the multiplicity of the unit cell of the low symmetry phase. As a consequence of this, additional reflections appear in the powder diffraction patterns, which are called as superlattice reflections.

The nomenclature of these tilted systems first given by A. M. Glazer (1972) and he discovered a total 23 possible tilt systems in perovskites[32]. In Glazer notations, the tilts of the octahedron are considered about the x, y, and z directions of the ideal cubic structure. We have used Glazer notation throughout the work and these are well described in the famous article by A. M. Glazer 1972[32]. As pointed out by Glazer [1972, 1975], rotation of BO_6 octahedra about one of the tetrad axes (say [001]) of the pseudo-cubic cell in, say, clockwise direction will force the neighbouring octahedra in the two perpendicular directions (i.e., [100] and [010]) to undergo rotation in the anticlockwise direction. The adjacent neighboring octahedra along the rotation axis, on the other hand, may rotate in the same sense (**in-phase**) i.e., both in a clockwise or anticlockwise direction. The neighbouring octahedra along the rotation axis may also undergo rotation in the opposite sense (**anti-phase**) i.e., rotation of one in a clockwise manner whiles the other in an anticlockwise manner (see Figure 1.7). The B-O-B bonds become staggered in the two directions perpendicular to the rotation axis.

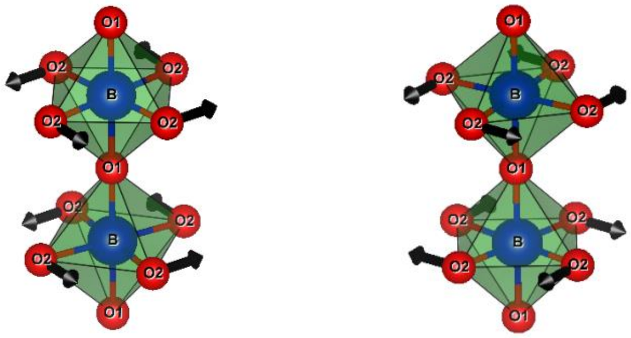

In-phase tilting **Anti-phase tilting**

Figure 1.7 In-phase and Anti-phase tilting of the oxygen octahedral in perovskites.

- **Example for in-phase octahedra tilting:** At high temperature (T>950 K) structure of $NaNbO_3$ is a cubic (a=b=c=3.9507 Å) **Pm$\bar{3}$m**. On lowering the temperature, it undergoes an antiferrodistortive phase transition and the NbO_6 octahedron get tilted in-phase about z-axis and become tetragonal (a=b=5.56816 Å, c= 3.93976 Å) with space group **P4/mbm** and the new cell parameters become $\sqrt{2}a_p\times\sqrt{2}a_p\times a_p$ i.e. unit cell size get doubled[33]. This tilt system is denoted by $a^0a^0c^+$.
- **Example for anti-phase octahedra tilting:** $SrTiO_3$ has a cubic structure at room temperature and it undergoes a structural phase transition from cubic **Pm$\bar{3}$m** (a=b=c= 3.905 Å) to tetragonal phase (a=b= 5.5134 Å, c= 7.8072 Å) with space group **I4/mcm** below 105 K[34]. The unit cell becomes two times along <001> with respect to the parent cubic structure. The tilt system is denoted by $a^0a^0c^-$.

Another example is an orthorhombic phase with space group **Pnma** in $CaTiO_3$ in which both in-phase and anti-phase tilting exist[35]. The tilt system in glazer notation is a^+b^- b^-. In the same way, many complex tilts are possible. These tilts change the crystal structure and affect the physical properties.

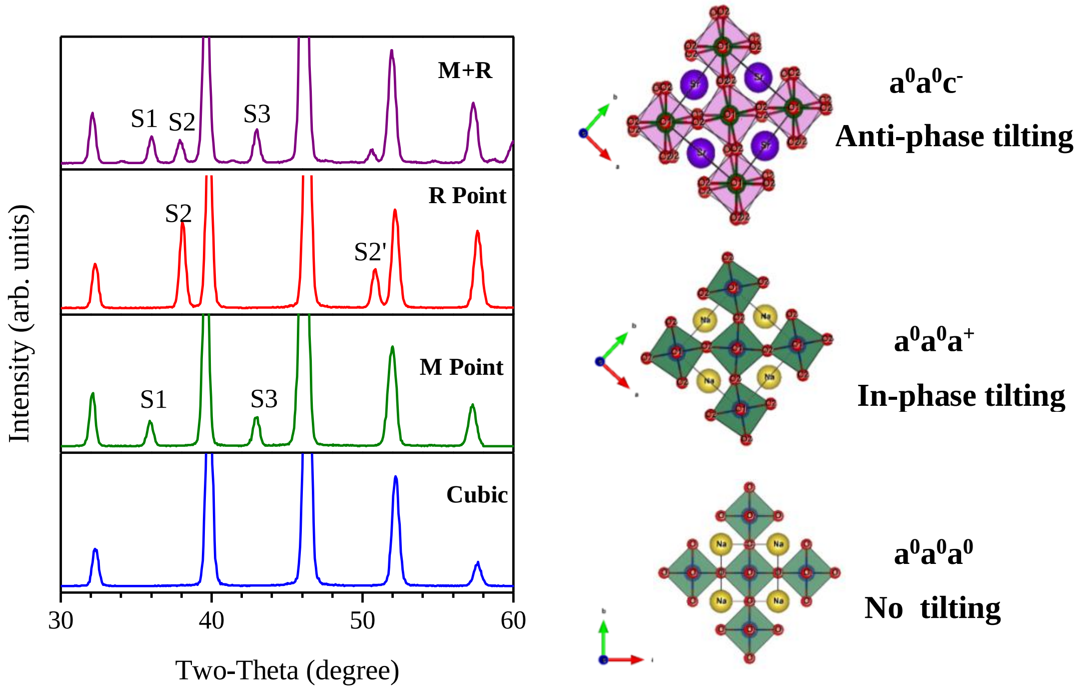

Figure 1.8 Schematic representation of the appearance of the superlattice reflections due to tilting of the oxygen octahedra in the diffraction patterns.

Figure 1.8 shows the schematic representation of the appearance of superlattice reflections S1, S2 and S3 in the diffraction pattern due to various octahedral rotation distortions. The Miller indices of the superlattice reflections based on the doubled pseudo-cubic perovskite cell carries information about the nature of the octahedral tilts in the structure. All odd integer (i.e., ‘ooo’ type indices) superlattice reflections correspond to the anti-phase (- tilt) tilts of the adjacent octahedra, whereas the presence of superlattice reflections with two odd and one even integer indices (i.e., ‘ooe’ type) implies the presence of in-phase (+tilt) tilt of the adjacent octahedra[32]. Often one also observes superlattice reflections with two even and one odd integer indices (i.e., ‘oee’ type). Such types of reflections are due to antiparallel cationic shifts in the structure[32].

1.3.3 Jahn-Teller Octahedral Distortion

According to Jahn-Teller theorem, “A molecule (nonlinear) with symmetrical atomic configuration and a degenerate electronic ground state is unstable and undergoes distortion to remove the degeneracy”[1]. In the case of perovskite compounds the (first-order) Jahn-Teller effect applies on the octahedrally coordinated transition metal ion B. If the B cation consists of d-shell electrons then to remove the degeneracy of the d-atomic orbitals, the cubic structure gets distorted and elongated about a particular axis[1, 31]. The best example of Jahn-Teller distorted perovskite is $KCuF_3$[36]. However, in the present work, we have not dealt with any such distortion because all the B cations in our systems have d^0 electronic configuration[9].

The most promising approach for the structure identification of perovskites with octahedral tilting and ferrodistortions is to consider first the possible tilting patterns and then to find the corresponding space groups. To identify the structures, the details of the group-theoretical analysis of octahedral tilting in ferroelectric perovskites can be found using the software ISOTROPY[37]. The article published by H. T. Stokes *et al.* [37] contains most of the information and group-theoretical analysis for possibilities of cationic displacement and octahedra tilt systems.

1.4 Role of Phonons in Structural Phase Transitions

Ferroelectric and antiferroelectric phase transitions represent a special class of the structural phase changes where the transition from the high to low symmetry phase is accompanied by the appearance of spontaneous polarisation or a sublattice polarisation[31]. The appearance of long-range polar or anti-polar order is the main characteristic of ferroelectric or antiferroelectric transition. These transitions involve distortion of the unit cell of the paraelectric phase.

In soft mode picture, the ferroelectric state is characterised by a macroscopic spontaneous polarization, the soft phonon must be both polar (i.e. infrared active) and of long-wavelength ($\bar{q}\approx 0$). On the other hand, the antiferroelectric state is characterised by the appearance of two opposite sublattice polarization and an increase in the size of the unit cell, so that the antiferroelectric soft phonon has a finite wavelength. More especially, **'ferroelectric ordering'** involves the instability of a phonon at Brillouin zone centre, $\bar{q} = 0$, whereas **'antiferroelectric ordering'** involves the instability of a Brillouin zone boundary, $\bar{q} = \bar{k}/2$, where $\bar{k}$ is a reciprocal lattice vector[38]. The instability with respect to a polar phonon of more general $\bar{q}$ involves 'sinusoidal' antiferroelectric ordering.

In the ABO_3 perovskite, the vibration of an R_{25} and M_3 phonon mode at R and M point of the simple cubic Brillouin zone is associated with anti-phase and in-phase tilt of octahedra[38]. As Figure 1.7 depicts the displacement patterns of ions involved in the vibration of an R_{25} and M_3 phonon modes. The adjacent octahedra vibrate in the opposite sense (180 degrees out of phase) in the R_{25} mode whereas they vibrate in the same sense (in-phase) in M_3 mode.

1.5 Soft Mode Theory and Displasive Phase Transitions

The crystal lattice is defined as an array of lattice points arranged in a periodic manner. There may be one or group of atoms can reside at each lattice point. In the crystals, atoms vibrate in a coherent manner and form a collective wave or excitations, these excitations are called phonons. The lattice dynamical calculations provide insight about the mechanisms of structural phase transitions in perovskite compounds and the role of phonons in terms of softening and freezing of phonon modes at high symmetry points with respect to the cubic Brillouin zone. Lots of studies have been done in this regard on various simple as well as complex systems such as $BaTiO_3$, $PbTiO_3$, $PbZrO_3$, and $NaNbO_3$[9, 31, 38]. However, the calculations of phonon dispersion relations could be performed using density functional theory

(DFT) at T=0 K but the theory is well established and show good agreement with the experimental results[31]. If the lattice dynamic calculations are performed for high-temperature phase of the materials that arise due to a displacive phase transition then the phonon dispersion shows freezing and/or softening of the phonon mode at zone boundary and/or zone centre in the Brillouin zone. According to these predictions, the structural phase transitions in perovskite compounds arise due to the competing interactions between various phonon instabilities occurring in the cubic phase. The ferrodistortive phase transitions involve the freezing of the zone centre phonon mode with respect to the cubic phase and the softening of the zone boundary phonon mode induces the antiferrodistortive phase transitions which result an increase in the multiplicity of the unit cell.

In this work, we are dealing with the phase transitions which are displacive type. In this kind of phase transitions, the crystal structure of the final phase will be the distorted form of parent phase and these phase transitions are accomplished by small displacement of atoms. These small displacements of atoms cause loss or inclusion of some symmetry elements[39]. For example in the case of perovskite family of structures, the ferroelectric phase transition occurs when there is a displacement of central metal cation and symmetry of the crystal reduces from cubic $\mathbf{m\bar{3}m}$ to tetragonal **4mm**[40]. This phase transition involves loss of three-fold rotation axis and centre of inversion. These phase transitions could be successfully explained in terms of corresponding phonon mode softening at any point (i.e. at any value of wave vector $\bar{k}$) in the Brillouin zone[9, 40]. In general, all the phonon modes are stable in the high-temperature symmetric phase. On cooling certain phonon mode frequency decreases (getting soft) and becomes zero at a critical temperature. At this temperature, the crystal gets destabilized due to freezing of such phonon mode and structural phase transition occurs.

1.5.1 Ferroelectric Phase Transition

Ferroelectric phase transitions occur when the symmetry breaking displacements of the atoms form dipoles and crystal attains a spontaneous polarization in the materials in the absence of an external electric field[40]. These transitions can be identified by the divergence in the dielectric susceptibility. The divergence in the static dielectric susceptibility was predicted by the Lyddane-Sachs-Teller (**LST**) relation[40]. This relates the limiting values of the longitudinal optic (**LO**) and transverse optic (**TO**) mode at $\bar{q}\rightarrow 0$ to the dielectric constants for the static electric field (with zero frequency) and with infinite frequency[40]. For simple cubic ionic solids,

$$\frac{\varepsilon\,(\omega = 0)}{\varepsilon\,(\omega = \infty)} = \frac{\omega^2(\mathrm{LO})}{\omega^2(\mathrm{TO})} \tag{1.1}$$

As predicted by the **LST** relation that for $\boldsymbol{\omega^2\,(\mathrm{TO})\rightarrow 0}$, the static dielectric constant $\boldsymbol{\varepsilon(\omega=0)\rightarrow \infty}$. Hence, these phase transitions could be explained on the basis of softening of zone centre transverse optic phonon mode [i.e. Γ-point phonon mode $\bar{q} = (0,0,0)$]. Due to the freezing of such phonon mode, the phase transition involves cationic displacement in such a way that the crystal structure becomes non-centrosymmetric and crystal attains a spontaneous polarization (P_s)**.** It is important to note here that if the phase transition is of first-order then the frequency will not become exactly zero. The most important thing is that this spontaneous polarization direction can be reversed by the application of an electric field in the opposite direction of the spontaneous polarization.

As we have already discussed, the case of non-polar cubic to polar tetragonal phase transitions in $PbTiO_3$ and $BaTiO_3$. In these systems the cationic displacement can be reversed by application of the external electric field. This reversal of the direction of spontaneous polarization is called polarization switching. The most important feature of the ferroelectric materials are that they show loop kind of behaviour of polarization against the electric field, which is known as **P-E hysteresis loop** (Figure 1.9). This ferroelectric loop comes due to the attainment of spontaneous reversible polarization (intrinsic) and movement of various domain walls (extrinsic) under the application of an external electric field.

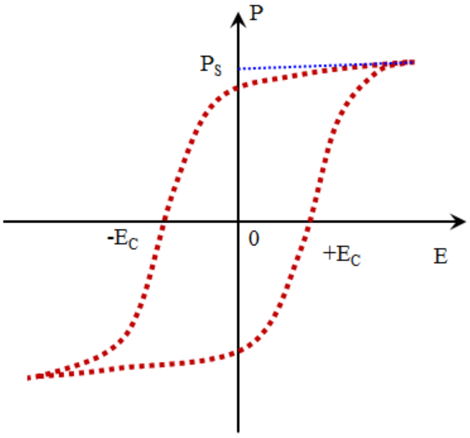

Figure 1.9 Schematic of the standard P-E loop of the ferroelectric materials.

1.5.2 Antiferroelectric Phase Transition

These phase transitions involve the anti-phase cationic displacements and the final structure contain net-zero spontaneous polarization. In general, an antiferroelectric phase consists of two or more sublattice polarizations of antiparallel nature leads to multiplying the unit cell of the antiferroelectric phase with respect to high symmetry phase. This gives rise to superlattice reflections in the diffraction pattern. These phase transitions involve the softening of zone boundary phonon mode with respect to the cubic phase[31]. The most famous examples for the antiferroelectric phase at the room temperature are $NaNbO_3$ and $PbZrO_3$ in which the spontaneous dipoles of the neighbouring unit cells get cancelled resultant with zero polarization.

1.5.3 Ferroelastic Phase Transition

A crystal is ferroelastic if it has two or more stable orientation states in the absence of mechanical stress and if it can be reproducibly transformed from one to another of these states by application of mechanical stress. Realizations are few: gadolinium molybdate $Gd_2(MoO_4)_3$ has a combined ferroelectric-ferroelastic transition; lead phosphate $Pb_3(PO_4)_2$ has a pure ferroelastic transition. Several crystals have combined the ferroelectric-ferroelastic transition[41-43].

1.6 Literature Review

This section consists of a brief review based on the past studied lead-based and lead-free piezo-ceramics with various important terms such as morphotropic phase boundary (MPB) and polymorphic phase boundary (PPB), etc.

1.6.1 Lead-based Piezo-Ceramics

Lead-based piezoelectric materials are the most suitable piezo-ceramics in terms of performance, cost, precursor availability and preparation[20]. The only drawback is they contain lead which is toxic. On the structural phase transition point of view, the theory of the high-performance of these Pb-based systems (PZT) is reported in the literature[44]. The phase diagram of PZT contains a morphotropic phase boundary (MPB) between the tetragonal and rhombohedral (monoclinic) phases[24], which provide easy polarization rotation and extension. These mechanisms are manily responsible for high electromechanical performance[2, 10, 24, 44].

1.6.2 Lead-free Piezo-Ceramics

There are three main families of lead-free piezoelectrics have been investigated namely KNN, BNT and $BaTiO_3$ based piezo-ceramics [2, 16, 17, 20, 21, 23, 24, 45, 46]. These systems are the most promising materials to develop lead-free piezoelectric ceramic with a comparative piezoelectric response as PZT.

1.6.2.1 Mechanism of Enhanced Physical Properties of Lead-Free Piezo-Ceramics

The most widely investigated lead-free modified KNN system (K, Na, Li)(Nb, Ta)O_3 showed large electromechanical properties at room temperature[10, 16, 17, 47, 48]. The enhanced properties were understood on the basis of the temperature-induced phase transition (Polymorphic Phase Boundary (PPB)) between tetragonal to orthorhombic phase near ambient temperature[24]. The temperature of this polymorphic phase transition can be altered by changing the composition. This shows mixed MPB and PPB character because this boundary is not vertical in the composition temperature phase diagram. Due to this behaviour, the properties are very much temperature-dependent and hence show fluctuations when the sample is heated or cooled. This is the serious problem of this system. The non-modified KNN has a vertical MPB between pseudo orthorhombic phases at 50:50 ratio of Na:Ka[20, 24]. However, it is found that there is no much enhancement in the properties near the MPB in this system as compared to the PZT [49]. It is also reported in some of the studies that the pseudo-orthorhombic phase in this system belongs to monoclinic symmetry. This concludes that it is not the criteria that the monoclinic phase always helps to get good electromechanical properties [20, 24].

The BNT based solid solutions show more complex phase transitions[2, 24]. The solid solution $Bi_{0.5}Na_{0.5}TiO_3$-x$BaTiO_3$: BNT-BT phase diagram consists of ferroelectric, relaxor and nonpolar phases that are not resolved yet[50]. There is a transition between rhombohedral to tetragonal phase at x~5-7% near room temperature[20, 24]. The structure on both sides of the MPB is pseudo-cubic. It is also reported that the piezoelectric d coefficient of BNT-BT ceramic is much smaller than the PZT and KNN across the MPB region.

The differences between the KNN, BNT-BT and PZT solid solutions can be interpreted in terms of the behaviour of MPB[24]. The MPB in the PZT separates well developed rhombohedral and tetragonal phases. The MPB ends at the tricritical point where rhombohedral, tetragonal and cubic phase coexist. However, in BNT and KNN based solid solutions don’t show such tricritical behaviour[20, 24].

Barium Titanate based lead-free piezoelectric materials are extensively studied in last few decades such as $(1-x)Ba(Zr_{0.2}Ti_{0.8})O_3$-$x(Ba_{0.7}Ca_{0.3})TiO_3$:BZT-xBCT, $(Bi_{0.5}Na_{0.5})TiO_3$-$BaTiO_3$:BNT-BT etc. Liu and Ren *et al.*[51] have been reported the value of piezoelectric coefficient ~620 pC/N and dielectric constant~3600 at room temperature for BCT-BZT at x=0.5 which is comparable to PZT. This high piezoelectric response in this material is explained in terms of easy polarization rotation and extension due to the coexistence of Cubic, Rhombohedral and Tetragonal phases at the same composition and temperature (Tricritical point) where the free energies of all the three phases become equal[2]. The behaviour of MPB between the rhombohedral and the tetragonal phases is similar to the PZT. However, the solid solution shows the good dielectric and piezoelectric response but low T_C < 100 ˚C is the major issue of these $BaTiO_3$ based piezo-ceramics.

1.6.2.2 Sodium Niobate ($NaNbO_3$)

Sodium niobate is one of the most studied perovskite material due to its good dielectric properties[52] and complex structural phases transitions. It shows a very rich phase transition sequence as shown in Figure 1.10. At room temperature, it has an antiferroelectric phase with orthorhombic structure (space group: **Pbcm**). The phase diagram with temperature of the pure sodium niobate contains total seven structural phases[53]. The high-temperature (T>950 K) structure of $NaNbO_3$ is cubic (U phase) with space group: **$Pm\bar{3}m$**. At lower temperature, it undergoes a series of antiferrodistortive phase transitions. First, it transforms to the paraelectric tetragonal T_2 phase (space group: **P4/mbm**). On further lowered temperatures it becomes orthorhombic T_1 (space group: **Cmcm**), S phase (space group: **Pbnm**), R phase (space group: **Pbnm**), and at room temperature, it transforms into P phase (space group: **Pbcm**). At lowest temperature, it undergoes a first-order transition and transforms into a ferroelectric rhombohedral N phase (space group: **R3c**)[54].

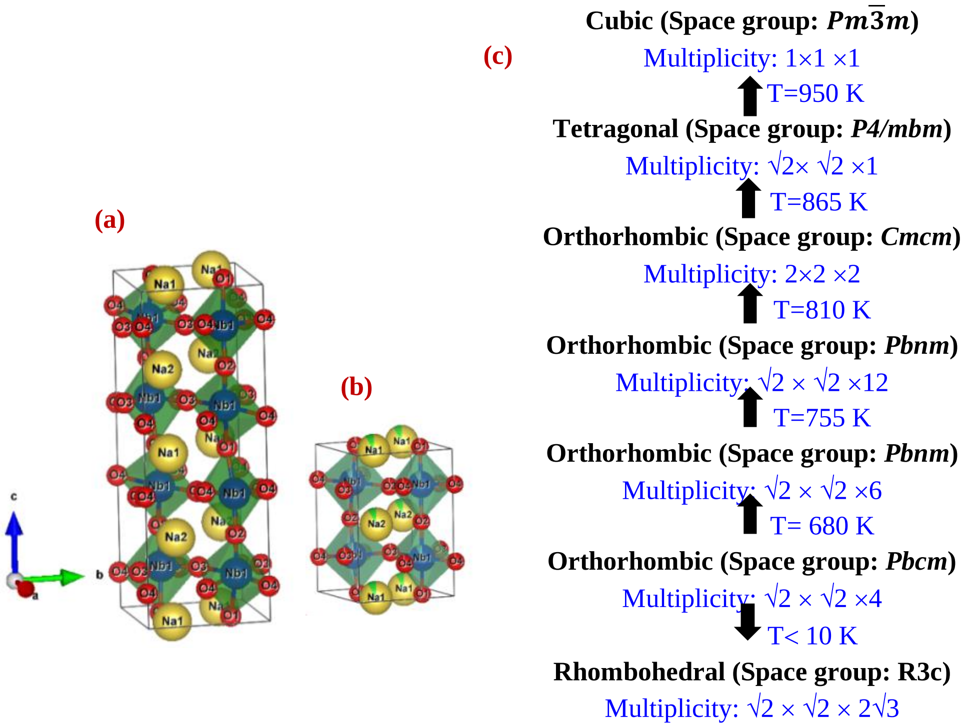

Figure 1.10 The (a) antiferroelectric orthorhombic phase (space group: **Pbcm**) can be transformed to (b) ferroelectric orthorhombic phase (space group: **$Pmc2_1$**) by the application of external electric field or substitution of A or B site atom for the $NaNbO_3$. (c) is the sequence of phase transitions obtained in $NaNbO_3$ with temperature after Mishra et al.[54]

The structural phase transitions at high pressure have also been reported. At high pressure, the room temperature antiferroelectric orthorhombic phase transforms into a paraelectric orthorhombic phase (space group: **Pbnm**)[55]. These phase transitions have been extensively reviewed by various researchers and probed by different techniques including dielectric spectroscopy, X-ray diffraction, neutron diffraction and Raman spectroscopy [33, 38, 52, 54, 56].

Along with structural complexity, it has a very good dielectric constant ~ 1500 near T_C (648 K). However, at room temperature, its electrical response is not sufficient (dielectric constant ~300) for the device applications[56]. The room temperature antiferroelectric phase of pure $NaNbO_3$ can be transformed into ferroelectric phase (space group: $\mathbf{Pmc2_1}$) on the application of external electric field[26] and on small substitution at A and B sites (see Figure 1.10 (a) and (b)). It is found that the small doping of other ferroelectric perovskite material in the $NaNbO_3$ matrix shows competing behaviour[54] which enables good electrical response at room temperature. Also, it alters the phase transition sequence as a function of temperature.

1.6.2.3 Barium Titanate ($BaTiO_3$)

Barium Titanate is the first synthetic perovskite compound which shows ferroelectricity at room temperature. This is the most widely studied perovskite compound in the pure and with the dopant[2, 20, 57]. The most important property is its good dielectric (ε'~1900) and piezoelectric (d_{33}~190 pC/N) properties at room temperature[15]. However, the problem is it has low T_C~ 393 K[2]. The structural phase transitions of this compound are well known and studied by various researchers. At high temperature, it has a paraelectric cubic structure with space group:$\mathbf{Pm\bar{3}m}$. On cooling, it undergoes three first-order ferrodistortive structural phase transitions[2]. First, it transforms from the cubic phase to the ferroelectric tetragonal phase.

(space group: **P4mm**) at 393 K. Further lowering the temperature (T<273 K), its structure becomes orthorhombic with space group **Amm2** and finally, it acquires rhombohedral structure (space group: **R3m**) below 183 K. Due to the low Curie temperature it is not directly applicable and used in doped or solid solution form with other perovskites.

1.6.2.4 Solid Solution of $NaNbO_3$-$BaTiO_3$

Lead-free solid solution [$(1-x)NaNbO_3$-$xBaTiO_3$]: NNBTx is studied by various researchers with the aim of searching good electrical properties and relatively high T_C in the $NaNbO_3$ rich compositions. This solid solution is similar to KNN except that the $KNbO_3$ has been replaced by $BaTiO_3$. The main problem with KNN is the poor densification of ceramic due to the high volatility of alkaline oxides which significantly affects the functional performance of this ceramic[58]. As suggested by Zeng *et al.*[58] the problem of poor densification of KNN can be resolved by doping of $BaTiO_3$ instead of $KNbO_3$ in the $NaNbO_3$ matrix because both show similar structural phase transitions. It is also observed that the $BaTiO_3$ based piezo-ceramics show very good electromechanical properties. Raveskii *et al.*[59] and other researchers have studied the various compositions in the full composition range. They have reported extensive electro-physical properties of this solid solution with expected structures. Figure 1.11 provides the value of temperature at dielectric constant maxima for the different compositions of the NNBT solid solution as available in the literature. It is reported that on increasing the $BaTiO_3$ composition, the dielectric maximum shifts to the lower temperatures and reaches to near room temperature for x=0.25. They also found the P-E hysteresis loops with good saturation for x=0.10 (NNBT10). For the same sample, they observed coercive field E_C (11 kV/cm), the spontaneous polarization P_S (15 $\mu C/cm^2$) and residual polarization P_R (13 $\mu C/cm^2$) at 50 Hz.

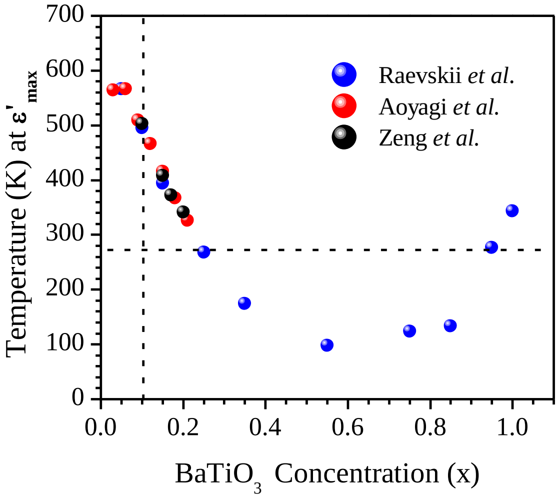

Figure 1.11 The variation of the temperature at dielectric maxima ε'_{max} with composition[58, 60, 61].

To keep this dielectric behaviour in mind, people mainly studied the compositions at the $NaNbO_3$ end in the search of good electrical and piezoelectric properties. Shih Xie *et al.* [60] have done the detailed study of microstructure, ferroelectric loop, and other electromechanical properties and showed well-saturated P-E loops for x=0.09 to 0.14. Zeng *et al.*[58] have also reported the electromechanical properties and dielectric behaviour of the different compositions. They reported that on increasing the concentration of $BaTiO_3$ the value of piezoelectric coefficient d_{33}, and electromechanical coupling constant k_p increases and shows maxima at x~0.10. On further increasing the BT concentration, the electromechanical response decreases (Figure 1.12). The reported value of d_{33} for the NNBT10 is about 147 pC/N at room temperature, which is much higher than the air fired KNN ceramic[58].

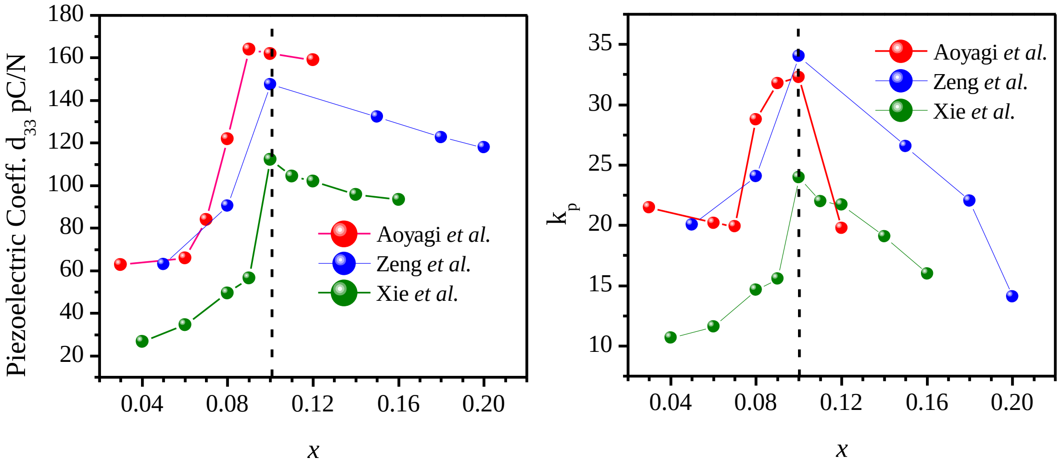

Figure 1.12 The variation of the Piezoelectric coefficient d_{33} (Left Panel), Electromechanical coupling factors k_p (Right Panel) with composition[58, 60, 61].

Zuo *et al.*[62] have thoroughly studied the temperature-dependent dielectric behaviour and electrostrictive effect for the compositions x=0.15 to 0.25. Along with piezoelectricity, electrostriction offers unique advantages such as no strain hysteresis, fast response speed, no poling requirement and reduced aging effects which are useful for high precision actuators. In this study they proposed that the addition of $BaTiO_3$ into the $NaNbO_3$ matrix disrupts the long-range ordered ferroelectric state and there is a formation of polar nano-regions (PNRs), which are responsible for dielectric relaxation i.e. relaxor ferroelectric behaviour in these samples. This relaxor ferroelectric behaviour has been found to be responsible for high electromechanical performance in various lead-based piezoelectric ceramics at high temperature such as in PMN. They also found that the sample of x=0.25 show hysteresis free P-E loop and strain vs. electric field (S-E) curve which is related to the enhanced dynamics and reduction in the size of polar nano regions. They reported the high dielectric constant (~6000 at 1 kHz) and very high electrostrictive coefficient Q_{33}~0.046 m^4/C^2 for x=0.25, which is almost twice of the Bi and Pb-based relaxor ceramics[62].

Since the properties of the NNBT10 are good as compared to other compositions. Few researchers have doped this composition with a small amount of the other perovskites such as $CaZrO_3$, $NaSbO_3$ and found morphotropic phase boundary (MPB) at very small doping. Zuo *et al.[63]* have also shown that the replacement of small amount of the $NaNbO_3$ from $CaZrO_3$ [(0.9-x)$NaNbO_3$ -0.1$BaTiO_3$-x$CaZrO_3$:NN-0.1BT-xCZ)] in this composition shows very good electromechanical properties (d_{33}=231 pC/N, k_P =35%, T_C=148 ˚C) and low hysteresis in the strain in the wide temperature range. They also claimed MPB in the (0.9-x)NN-0.1BT-xCZ ceramic at around x=0.025 between the end structures, tetragonal with space group **P4mm** and the rhombohedral with space group **R3c**[63]. The similar investigation is done by He Qi *et al.*, in which they prepared the solid solutions [(0.9-x)$NaNbO_3$-0.1$BaTiO_3$-x$NaSbO_3$][64]. They reported that there is an MPB at around x=0.03-0.04 and the excellent electromechanical properties (d_{33}=252 pC/N, k_P=36%, Q_m =168, $\varepsilon_r'/\varepsilon_0$ =2063 and T_C=109 ˚C) for x=0.035.

However, the electromechanical properties of the NNBTx solid solution are exceptionally remarkable. The literature contains very little information about the structural phase transition with composition and temperature. Most of the reports contain only knowledge of expected room temperature structures probed using X-ray diffraction studies. Raveskii *et al.* [59]have proposed the monoclinic structure of the compositions x~0.05-0.07 at room temperature. The further increase of $BaTiO_3$ transforms it into the tetragonal phase and the compositions x~0.20 to 0.98 are characterized by a slightly distorted pseudo-cubic structure. Finally the further increase in concentration x>0.98, the structure becomes again tetragonal. Recently, similar findings have reported by Xu Lu *et al.*[65]. They observed a ferroelectric tetragonal phase (space group: **P4mm**) to the paraelectric cubic phase (space group: $\mathbf{Pm\bar{3}m}$) on increasing the concentration of $BaTiO_3$ from x=0.10 to 0.27 at x~0.22.

1.7 Scope of the Thesis

Solid solution of (1-x) $NaNbO_3$-$xBaTiO_3$ (NN-xBT) is analogous to (1-x) $PbZrO_3$-$xPbTiO_3$, where one end-member is antiferroelectric while the other end-member is ferroelectric in nature and expected to show anomalous behaviour. The antiferroelectric state of pure sodium niobate can be suppressed by doping of $BaTiO_3$. The mismatch in ionic radii of different atoms causes chemical pressure and perturb various interactions present in the system. In addition to this, the formation of long-range polar order is inhibited by random field and random bonds in the solid solutions having multiple cations with different sizes, valences or polarizabilities occupying crystallographic equivalent sites. As a result, the short-range ordered relaxor (R) state is expected to form. Relaxor-based solid solutions are used in a wide variety of piezoelectric applications owing to their excellent electromechanical properties. So far, the NN-xBT solid solutions have been studied with the main focus on their dielectric properties and relaxor behaviour. Other than their technological applications, one of the end-member, sodium niobate, is a very important system for understanding the mechanism of structural phase transitions. The doping of a small amount of $BaTiO_3$ is expected to distort the sodium niobate lattice and show a variety of structural phase transitions as a function of composition and temperature.

To investigate, the effect of chemical pressure on competition and cooperation between polar and antiferrodistortive distortions, which arises from the substitution of $BaTiO_3$ in the $NaNbO_3$ matrix, we carried out a detailed study using a combination of experimental tools likes X-ray, neutron diffraction, Raman spectroscopy, dielectric and ferroelectric measurements. The phase purity and structural phase transition were investigated by powder X-ray and neutron diffraction studies. The Raman spectroscopy is used to provide information about the role of the zone centre phonons during the structural phase transitions. Dielectric and ferroelectric measurements are used for electrical properties studies.

1.8 Organization of the Thesis

The entire work is presented into a total seven chapters. The present **Chapter 1** contains basic definitions and review of the relevant literature. **Chapter 2** describes the details of sample synthesis, experimental tools, and technique used to accomplish the structural and phonon studies for proposed materials**. Chapter 3** describes the X-ray diffraction based study of NNBTx solid solution as a function of composition and temperature. Studies on phase stabilities and nature of structural phase of compositions x=0.03 and 0.05 below room temperature using powder neutron diffraction techniques are presented in **Chapter 4. Chapter 5** contains the results of antiferrodistortive phase transition studies for compositionally modified [(1-x) $NaNbO_3$-x$BaTiO_3$:NNBTx] for x=0.0 to 0.15 and room temperature using Raman Scattering. The results for the identification of the involvement of phonons during the structural phase transition for NNBT05 as a function of temperature from 83 K to 298 K, using Raman scattering experiments are presented in **Chapter 6.** A summary of the main finding of this work and suggestions for future work are presented in **Chapter 7.**

Chapter 2: Experimental Tools and Techniques

To study the behaviour of structural phase transitions in compositionally modified NNBTx. Samples were prepared using solid-state reaction method. The prepared samples were characterised using various techniques such as dielectric impedance spectroscopy, X-ray diffraction, neutron diffraction, and P-E loop measurements, etc. The present chapter comprises the brief introduction of the experimental techniques and analysis methods used in the sample synthesis and characterization.

2.1 Sample Synthesis

There are various techniques, which involve different approaches such as physical and chemical routes for the synthesis of bulk powder samples of our interest such as solid-state reaction, co-precipitation, sol-gel method, etc[57]. We used solid-state reaction method to prepare the bulk ceramic samples.

2.1.1 Solid-State Reaction Method

The basic principle of solid-state reaction is based on the diffusion and rearrangement of the ions of the two or more oxides. Since the method is based on the diffusion in solids, so, the process requires very high temperature (>1073 K) heat treatment for several hours. As schematically shown in Figure 2.1, diffusion in the two types of oxides namely AO and BO_2 and after the heat-treatment at appropriate temperature and time, there is a formation of the final product ABO_3. This process of the reaction between the solid oxides via high-temperature diffusion is called calcination. Since the calcination involves the chemical reaction, the driving force of calcination is minimization of Gibbs free energy and gets the most stable atomic arrangement in the crystal. After the calcination, we get the compound in the reacted powder form. The further processing is needed to increase the density of the samples. The calcined powders were packed into the solid body form and then heated at elevated temperatures. This process is called ***sintering***.

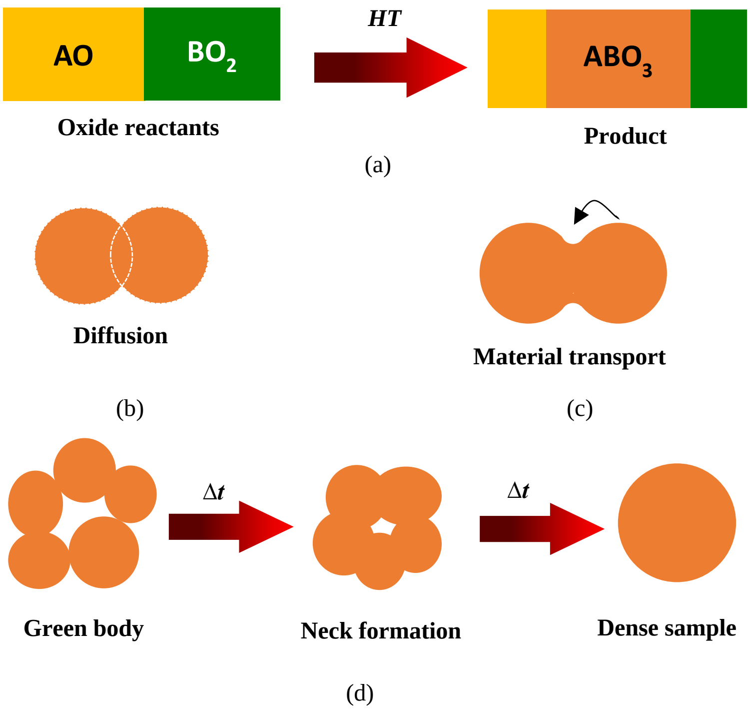

Figure 2.1 Schematic representation of the (a) calcination procedure in which two oxides get reacted and form a final product. The mechanism of (b) solid-state diffusion and (c) material transport via evaporation from the high vapour pressure to low vapour pressure and condensation during sintering. (d)The whole procedure of sintering involving neck formation to pores filling with time at fixed temperature with time. (Courtesy: Understanding the Solids:The Science of Materials , R. J. D.Tilley ISBN: 9780470852767)

The sintering process does not involve any reaction of the reactants so the only driving force of this process is minimization of the surface area. As a result, the pores in the packed powder body reduce and we get pellets with increased density. These pellets are used for further characterization.

2.1.2 Experimental Procedure for Sample Synthesis

The conventional solid-state reaction method consists of the following step during sample synthesis:

- **Weighing of the raw materials:** Analytical reagent grade (AR) of Sodium carbonate (Na_2CO_3), Barium carbonate ($BaCO_3$), Titanium oxide (TiO_2), and Niobium oxide (Nb_2O_5) were weighed in the stoichiometric ratios.
- **Mixing of the raw powders:** The weighed powders were mixed using the agate mortar and pestle thoroughly by hand mixing. The mixed powder was ball milled using the planetary ball mill in which the sample containers and balls were made up of zirconia (ZrO_2) with the acetone as a wet medium. The wet mixed powder was dried completely and used for the calcination.
- **Calcination:** The mixed dried powder was poured into the alumina crucibles and fired into the box furnace in the presence of air for 6 hrs., at the temperature of around 1323-1373 K. The heating and cooling rate were maintained 3 K/min.

  The following reaction takes place during the calcination process,

  $(1\text{-}x)BaCO_3 + (1\text{-}x)TiO_2 + (x/2)\ Na_2CO_3 + (x/2)\ Nb_2O_5 \rightarrow Ba_{(1-x)}Ti_{(1-x)}Na_xNb_xO_3 + CO_2\uparrow$

  $BaCO_3 \rightarrow BaO + CO_2\uparrow$
  $Na_2CO_3 \rightarrow Na_2O + CO_2\uparrow$
  $BaO \rightarrow Ba^{2+} + O^{2-}$; $Na_2O \rightarrow 2Na^{+} + O^{2-}$
  $Nb_2O_5 \rightarrow 2Nb^{+5} + 5O^{2-}$; $TiO_2 \rightarrow Ti^{4+} + O^{2-}$
  $(1\text{-}x)[Ba^{2+} + Ti^{4+}] + x[Na^{+} + Nb^{+5}] + 3O^{2-} \rightarrow Ba_{(1-x)}Ti_{(1-x)}Na_xNb_xO_3$
- **Pelletization:** The calcined powder was mixed again after calcination and some binder solution (PVA/ Glysrol) was added into the powder for the formation of solid bodies. The binder mixed powder was poured into the stainless steel dies and the cylindrical shaped pellets were made using the uniaxial pellet press.

- **Sintering:** The green pellets were put on the platinum disc and heat-treated at 773-873 K for 8-10 hrs., with the rate of 2 K/min to remove the binder and then heated at higher temperatures at ~ 1423-1523 K for 6 hrs. The heating and cooling rates were fixed at 2-3 K/min.
- **Confirmation of phase purity and further characterization:** Some of these pellets were crushed thoroughly and then again heated at 873 K for 8 hrs. for the removal of the strain. Then used for the X-ray diffraction measurement to confirm the phase purity of the prepared samples. The other pellets were used for the Raman and electrical measurements.

2.2 Characterization Techniques

The crystal structure and structural phase transition behaviour of compositionally modified NNBTx were investigated using powder X-ray and neutron diffraction techniques as a function of compositions and temperatures.

2.2.1 Diffraction

The diffraction pattern arises due to the superposition of the scattered waves from the scattering object. The theory of diffraction of radiation (X-rays, Neutrons, electrons) from crystals is very important to carry out the diffraction experiments and to understand the results. The most common phenomenon of the scattering is elastic scattering in which incident radiation (X-rays, neutron or electron beam, etc.) with the wave vector $\overline{k_i}$ falls on the scattering object and get scattered with the same energy (i.e. $E_i = E_f$) in a particular scattering angle direction with the wave vector $\overline{k_f}$ (see Figure 2.2). In the complete event, there is no energy exchange between the scattering object and incident radiation. However, due to the change in the direction, there is a change in the momentum, which is denoted by $\overline{Q}$. This is known as wave vector transfer or scattering vector and its magnitude is $|\bar{Q}| = (4\pi/\lambda)\ sin\theta$. This is a natural variable for the elastic scattering event.

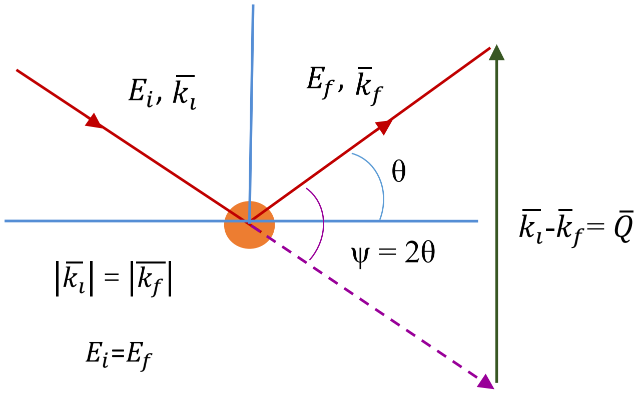

Figure 2.2 Schematic of the elastic scattering geometry.

During the elastic scattering, there is no change in the energy of the radiation. However, in the case of inelastic scattering, the energy of the incident radiation does not conserve and the scattering object and incident radiation may exchange the energy. Here, we are dealing with the *elastic scattering* of the X-rays and neutrons from crystals.

2.2.2 Diffraction from Crystals:

A crystal is a periodic array of atoms or molecules. The diffraction of radiations (X-rays, neutrons, and electrons) are the most successful tools to determine the crystal structure of the materials. When any radiation falls on the crystalline materials, it gets scattered from the periodic array of atoms (Figure 2.3) present in the crystals depending upon the type of interaction and each atom behaves like an independent source of spherical waves. In the far-field region, these waves follow the superposition principle and form a diffraction pattern. These diffraction patterns contain all the information about the location of each atom present in the crystal and their periodicity in the crystal structure.

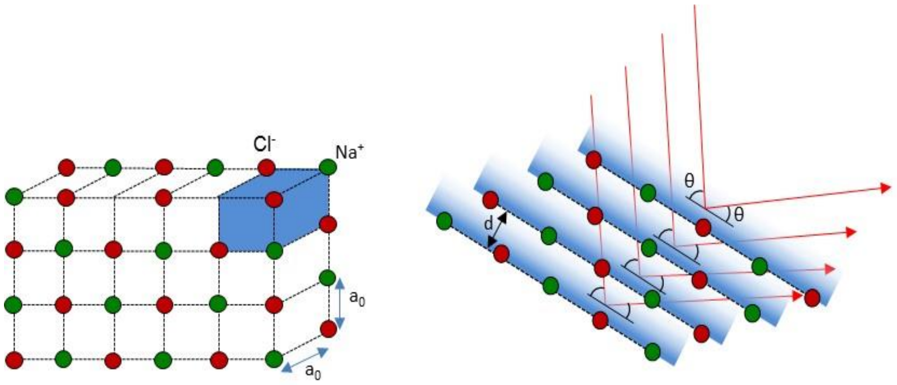

Figure 2.3 Schematic of periodic arrangement molecules and presence of lattice planes in crystals.

Since crystals have periodicity, so there exists a repetitive unit called unit cell. The contribution of all atoms in a unit cell in the scattering termed as structure factor. For the unit cell containing atoms with a form factor $f_j\,(Q)$ for the j^{th} atom at position vector $\bar{r}_j$ then structure factor for the unit cell is given by,

$$\boldsymbol{F}^{unit\ cell} = \sum_{j=1}^{n} f_j\,(Q) e^{i\bar{Q}.\bar{r}_j} \tag{2.1}$$

The scattering amplitude for the crystal containing n number of unit cells is defined as,

$$\boldsymbol{F}^{cystal} = \sum_{j} f_j\,(Q) e^{i\bar{Q}.\bar{r}_j} \sum_{n} e^{i\bar{Q}.\bar{R}_n} \tag{2.2}$$

Where, $\bar{R}_n = n_1\bar{a}_1 + n_2\bar{a}_2 + n_3\bar{a}_3$ are the lattice translation vectors with n_1, n_2, n_3 integers and $\bar{a}_1, \bar{a}_2, \bar{a}_3$ basis vectors in real space.

2.2.2.1 Bragg's Law

In 1913, Lawrence Bragg and his father William Henry Bragg proposed a model to describe the diffraction patterns arise during X-ray scattering through crystals[66]. They proposed that the crystals can be supposed to have planes of the electron cloud and the X-rays of the wavelength comparable to the interplanar spacing are reflected through these planes and form an interference pattern (Figure 2.4).

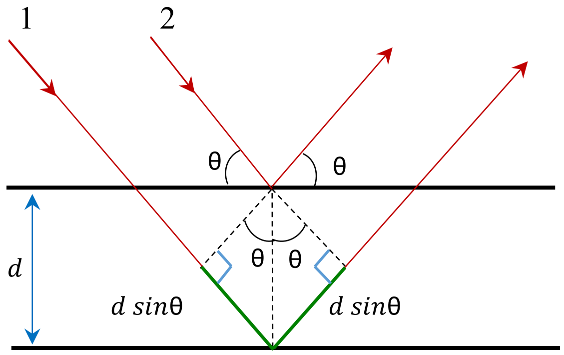

Figure 2.4 Diffraction from crystal planes and derivation of Bragg's law.

This model successfully explains the complete information of diffraction patterns arise during X-ray, neutrons and electron diffraction and very important in determining the crystal structure. Based on this model they obtained a relation between the wavelength of the incident radiation λ, the interplanar distance of the crystal planes d and angle of reflection θ,

$$2d\ sin\theta = n\lambda \tag{2.3}$$

$$2d_{hkl}\ sin\theta = \lambda \tag{2.4}$$

Where *n* is the order of reflection and *h*, *k* and *l* are the Miller indices of the particular family of planes.

The structure factor for particular reflection (hkl) can be written as,

$$\boldsymbol{F_{hkl}} = \sum_{j=1}^{n} f_j\,(Q) e^{2\pi i(hx_j+ky_j+lz_j)} \tag{2.5}$$

In the case of neutron diffraction the above relation becomes,

$$\boldsymbol{F_{hkl}} = \sum_{j=1}^{n} b_j e^{2\pi i(hx_j+ky_j+lz_j)} \tag{2.6}$$

Where, b_j is the neutron scattering length of the nucleus of the j^{th} atom.

2.2.2.2 Elastic X-Ray Scattering

Firstly, we are dealing with the diffraction of X-rays. X-ray is electromagnetic radiation. These mainly interact with the electrons present in the material and get scattered through Coulomb potential. In classical theory, electromagnetic radiation exerts a force on the charged particles, which accelerates it. As a result, the charged particle emits radiation in the form of the scattered waves. This scattering is called *Thompson scattering*[67].

2.2.2.3 Elastic Neutron Scattering

Neutrons are the charge-neutral nuclear quantum particles, which show wave-particle duality. The wavelength of the neutrons is dependent on their velocity and given by de Broglie formula, $\lambda = h/(mv)$. The beam of neutrons shows scattering with the materials similar to electromagnetic radiation. The difference is that the neutrons primarily interact due to the strong nuclear force during the interaction with the nuclei of the atoms present in the materials. The neutron interacts with the nucleus and form a compound nucleus and then it gets shattered in the scattering direction. Enrico Fermi approximated the interaction potential of the neutron scattering and known as Fermi pseudo-potential[66, 68].

The neutron scattering cross-section for single nucleus is given by,

$$\left(\frac{d\sigma}{d\Omega}\right) = b^2 \tag{2.7}$$

Where, b is the nuclear scattering length. Since we are discussing here the scattering of thermal neutrons from the nucleus, which is very tiny as compared to the wavelength. So, it is considered as s-wave scattering, which is isotropic in all directions. The total scattering cross-section is $4\pi b^2$ in barns. The value of nuclear scattering length b for neutrons is independent of the atomic number of the elements and shows variations for the different isotopes and it does not have any $\overline{Q}$ dependence. Neutrons also interact with the unpaired electrons of the atoms because both the particles have a magnetic moment. This interaction contributes to the magnetic scattering and its scattering length falls on increasing the $\overline{Q}$ value due to the finite size of atoms.

2.2.3 Powder Diffraction Experiments

The powder diffraction experiments are most commonly used for the crystal structure determination of the materials. The main advantage of the powder diffraction measurement over the single crystal measurements is easy sample synthesis. It is always easier to synthesize powder samples for most of the materials than their single crystals. However, we observe very much overlap and difficulty in indexing the powder diffraction patterns. Nevertheless, this is a very easy and reliable technique for structure determination. In the powder diffraction experiment, the monochromatic (sometimes polychromatic) radiation interacts with randomly oriented powder crystals which give all possible orientations of the crystal planes. The scattered beam of radiation form cones called “Debye cones” and the 2-D or 1-D diffraction patterns are detected in the form of rings or lines depending upon the type of detector.

2.2.3.1 X-Ray Powder Diffraction

The primary phase analysis of the prepared powder sample is done using the X-ray diffraction technique. We have used rotating anode based X-ray diffractometer with Cu target and curved crystal graphite monochromator working in the Bragg-Brentano geometry. The theta-theta continuous scan mode is employed with time step size 0.02˚ with scan speed 2 ˚/min with the help of Sodium Iodide (NaI) scintillation point detector. Sintered pellets of the sample were crushed and annealed at 873 K for 8 hrs. to check the phase purity. Along with ambient measurements, we also performed X-ray powder diffraction measurements at low and high temperatures. The low-temperature setup is CCR based and provides a temperature environment from12 K to 300 K with temperature stability of ± 1 K. For high-temperature measurements, there is a furnace attachment with the dynamic vacuum to provide a temperature range 300 K to 1200 K.

2.2.3.2 Powder Neutron Diffraction

The powder neutron diffractometer PD2 in the Dhruva Research Reactor is used for the neutron diffraction experiments with Debye-Scherer geometry. The monochromatic beam of wavelength 1.2443 Å was used to probe the sample. The schematic diagram of the PD2 is shown in the (Figure 2.5). The finely crushed powder samples were packed in the cylindrical Vanadium container. To get the diffraction data, this instrument contains five position-sensitive linear detectors (PSDs) made up of wire of Ni-Cr alloy (10 μm radius) with the specific resistance of 9 Ω/mm, covering wide angular range $4° < 2\theta < 140°$. The Brass tube of radius

36.5 mm is used for filling the ^{3}He and Kr gas at a partial pressure of 10 atm. and 2 atm. respectively. The instrumental parameters of PD2 are given in Table 2.1.

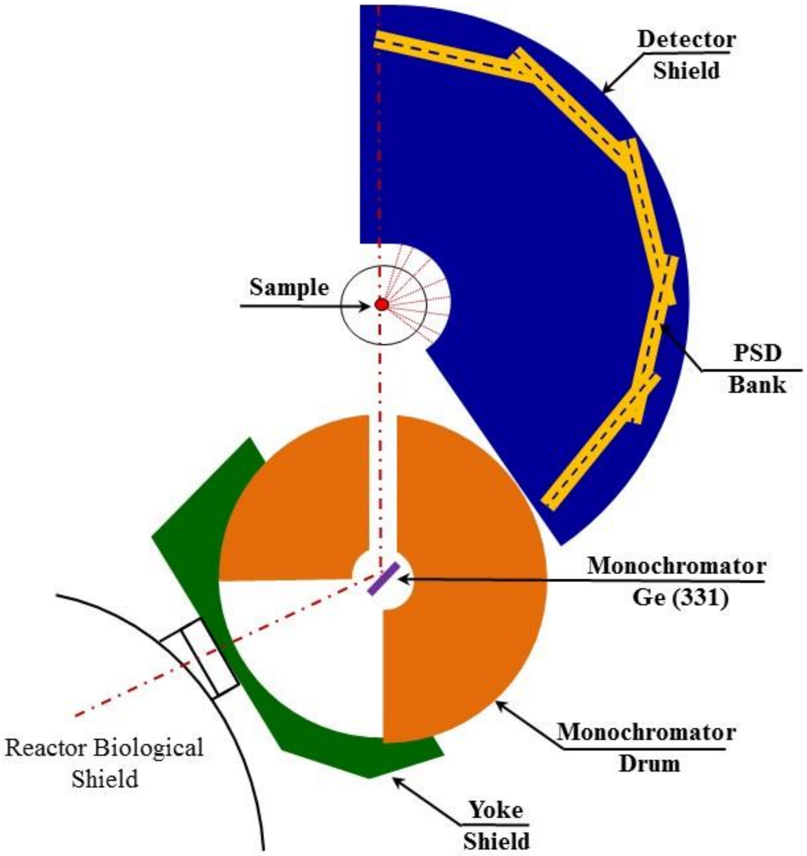

Figure 2.5 Schematic of the Neutron Diffractometer PD2 in Dhruva Reactor.

Table 2.1 The list of various instrumental parameters of the powder neutron diffractometer PD2 in Dhruva Research Reactor.

Instrument	Powder Diffractometer 2
Monochromator	Germanium (331)
Wavelength	1.2443 Å
Beam Size	4 cm. × 1.5 cm.
Flux at sample	8.5×10^5 neutrons/cm2/sec
Angular Range	$4° < 2\theta < 140°$
Q Range	0.4-9.4 $Å^{-1}$
$\Delta d/d$	0.8 %
Detector	5 (1-D PSDs)
Temperature Range	6 K to 1200 K

2.2.4 X-Ray vs. Neutron Diffraction

Why Neutron Diffraction is required? It is the most important thing to understand the utility of neutron diffraction and its advantages over X-ray diffraction. The typical X-ray and neutron diffraction patterns are shown in Figure 2.6.

The neutron diffraction is advantageous due following facilities,

- **Position of Low Z Elements:** The scattering power of the particular element for X-rays depends upon the Z value (atomic number). Therefore, it becomes a problem when we deal with such samples which contain low Z elements (such as O, Li, Na, etc.) in the presence of high Z elements. However, in the case of Neutron diffraction the scattering power does not dependent on the Z value and even light elements such as oxygen etc. give sufficient intensity.

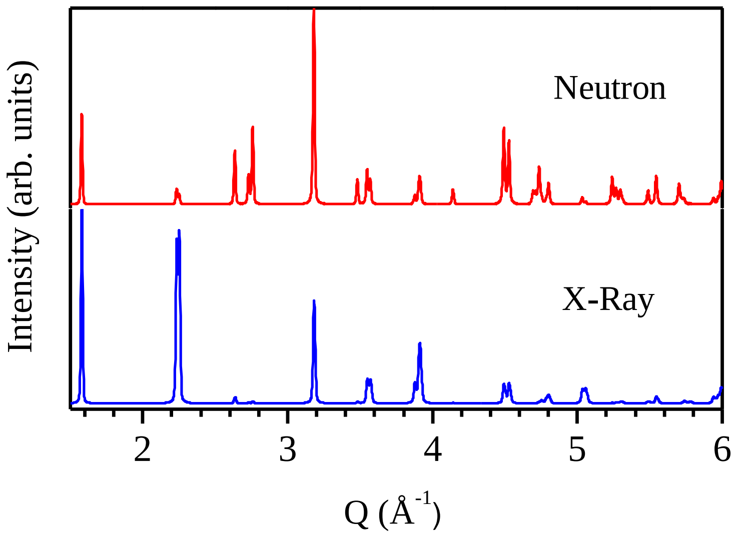

Figure 2.6 Comparision between the X-ray and neutron diffraction patterns.

- **High $\overline{Q}$ Range:** The resolution of the diffractometer varies as a function of $\overline{Q}$ value. The peaks at higher $\overline{Q}$ values get more resolved due to angle dependence. The neutron scattering length is a constant value of the particular isotope and it is independent of $\overline{Q}$. So, we get sufficient intensity even at higher angles, which helps in the determination of precise crystal structure and thermal parameters.
- **Sample Penetration:** The penetration power of the neutron is much higher than the X-rays for the solids. Therefore, the neutron diffraction is a very powerful technique to get the correct information of bulk materials.
- **Magnetic Scattering:** The neutron diffraction is the best technique to probe the magnetic structures and the ordering of the magnetic moments in the magnetic materials.

However, in the present work, we are dealing with non-magnetic ferroelectric materials. The phase transitions in the ferroelectric materials are governed by the shifting and/or tilting of the oxygen octahedron with respect to metal cations. Since oxygen is a low Z element in the presence of high Z elements. In the case of X-ray diffraction, the main scattering occurs from high Z elements present in the sample and it becomes difficult to extract the precise information of the low Z elements. Therefore, it is always preferable to perform neutron diffraction measurement which provides better positions of the low Z elements and reliable thermal parameters.

2.2.5 Rietveld Data Analysis

We fit the experimental data with a calculated one. The powder X-ray and neutron diffraction data were analysed using the Rietveld refinement technique. Rietveld refinement is a least-square fitting technique, which uses the initial values of the proposed model and then the subsequent iterations give fitted structural parameters[69]. The experimental data can be fitted very nicely using the guessed model for structure (lattice parameters, space group, atomic positions, and occupancies), background, and the instrumental parameters such as diffraction geometry, wavelength of the incident radiation, peak shape, etc. We have used **FULLPROF**[70] software for structure refinement.

2.2.6 Raman Spectroscopy

Raman spectroscopy is a powerful optical spectroscopic technique for the characterization of the materials. It is based on the inelastic scattering of the light during light-matter interaction called Raman effect. The process of inelastic scattering of light can be simply understood using an energy level diagram as shown in Figure 2.7. The incident laser light of frequency (ω_0) interacts with the molecules of the solid and transition occurs from the vibrational state to a virtual state. Further, the excited molecules re-emit the light after de-excitation. Depending upon transition from the initial and final vibrational level, we observed three kinds of scattering phenomena called Rayleigh, Stokes and Anti-Stokes scattering. Firstly, when the vibrational state of absorption and emission is the same, the emitted radiation has the frequency same as of the incident light, called “**Rayleigh scattering**”.

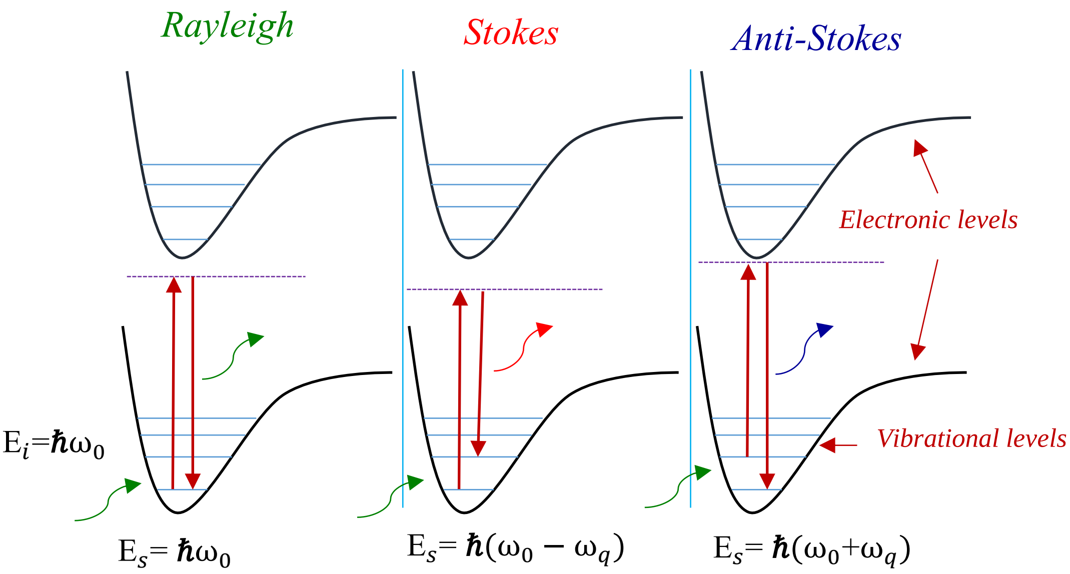

Figure 2.7 Energy level diagram to describe various light scattering phenomena.

In the case of Stokes scattering, the incident laser light excites the molecules of vibrational ground state to a virtual state and after emission of light with lower frequency (ω_S) the molecule return back to first excited vibrational level. In the case of anti-Stokes scattering, the molecules/atoms in the excited vibrational level by absorbing the incident laser light get excited to the virtual level and then after the emission of the light of higher frequency (ω_{AS}), it returns to the ground vibrational level. The Stoke scattering is more probable at ambient temperature because most of the molecules stay in their ground vibrational state rather than a higher vibrational state. Since the frequency of the inelastically scattered radiation depends upon the vibrational energy states of the molecules/ atoms in the crystal, the Raman spectrum is a fingerprint of the investigated material.

Phonons are the quanta of the crystal vibrations. Figure 2.8 shows the dispersion of the optical and acoustic phonons in the case of one-dimensional diatomic chain of atoms. The green dashed line indicates the region which can be probed using the optical Raman spectroscopy. In the case of three-dimensional lattice of n atoms per primitive cell, there are total 3n phonon branches. The 3 branches belong acoustic phonons (AP) and 3n-3 to optical phonons (OP).

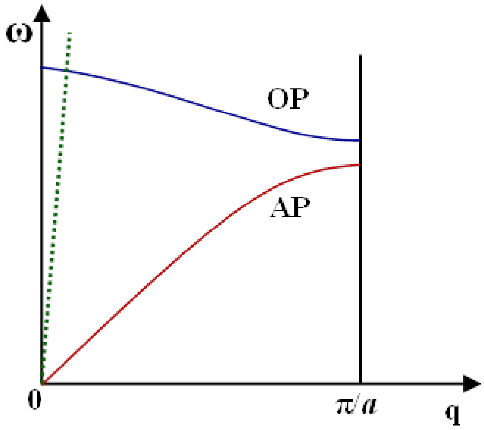

Figure 2.8 Schematic of the phonon dispersion relation for the one dimensional diatomic lattice.

The energy and moment of the system remain conserved in the complete scattering process. If the ω_s is the frequency of the scattered radiation then,

$$\hbar\omega_s = \hbar\omega_0 + \hbar\omega_q \tag{2.8}$$

$$\hbar\, \bar{k}_s = \hbar\, \bar{k}_0 - \hbar\bar{q} \tag{2.9}$$

Where, $\bar{k}_0, \bar{k}_s$ and $\bar{q}$ are the momentum of incident, scattered photons and phonon. Since the value of frequency of the incident light and the scattered light are very close i.e. $\omega_0 \gg \omega_q$, and $|\bar{k}_s| \backsimeq |\bar{k}_0|$ the magnitude of the scattered phonon momentum, $|\bar{q}| = 2|\bar{k}_0|\sin(\theta/2)$. In the backscattering geometry, $\theta \sim 180^{\circ}$ which implies $|\bar{q}| = 2|\mathrm{k}_0|$. It is a very important result, which tells us that using optical light, we can only probe the vibrational modes near the centre of Brillouin zone, i.e. $\bar{q}$~0.

2.2.6.1 Raman Instrumentation

The Raman spectra at ambient conditions were recorded in a micro-Raman spectrograph LabRAM HR 800 evolution with a 50X LWD objective. The excitation source used was 532 nm solid-state laser of power~ 25mW. The Raman instrument has a spectral resolution <1.5 cm^{-1}. The spot size of the beam is of 3-4 μm. The ultra-low frequency cut-off filter is used to record the spectra from 10 cm^{-1}. The low-temperature Raman data were recorded in reflection geometry using triple stage Raman spectrograph (JobinYvon T64000) with Peltier cooled CCD detector. The diode pump laser of 532 nm wavelength was used to excite the Raman signal. The Linkam's THMS600 low-temperature cryostat was used to cool the sample up to liquid nitrogen temperature with the T95 system controller to control the temperature. Data was collected in the temperature range 83 K< T <300 K at a resolution of ~ 4 cm^{-1} in both heating and cooling cycles.

2.2.6.2 Fitting of the Raman Spectra

We have fitted the Raman modes with the damped harmonic oscillator (DHO) model [71]. The central peak is fitted with a Lorentz function. The combined function used for the entire Raman spectra with the central peak is given below with a linear baseline.

$$\mathrm{I}(\omega) = \frac{A_{CP}(\Gamma_{CP}/2)}{\pi[\omega^2 + (\Gamma_{CP}/2)^2]} + [n(\omega) + 1]\sum_{k=1}^{n} \frac{A_k \Gamma_k \omega_k^2 \omega}{[(\omega^2 - \omega_k^2)^2 + (\omega \Gamma_k)^2]} \qquad (2.10)$$

Where, $n(\omega)$ is the Bose-Einstein population factor.

$$n(\omega) = \frac{1}{[e^{hc/\lambda kT} - 1]} \qquad (2.11)$$

A and Γ_{CP} are the proportional constant and the width of the central peak, respectively. A_k, ω_k, and Γ_k are the amplitude, peak position, and damping constant, respectively, of the kth Raman mode.

2.2.7 Electrical Measurements

The electrical measurements of the prepared solid solutions are done using dielectric setup and ferroelectric loop tracer.

2.2.7.1 Dielectric Constant Measurement

Structural phase transitions in the ferroelectric/ piezoelectric materials involve anomalous behaviour in the dielectric response with temperature and frequencies. In general, the ferroelectric materials follow the Curie-Weiss law, when the structural phase transition occurs from the paraelectric to ferroelectric phase.

$$\varepsilon' \sim \frac{C}{T - Tc} \tag{2.12}$$

Where, ε', C, T_C are a real part of dielectric constant, Curie constant, and critical temperature, respectively. This behaviour is directly related to the softening of the optical phonon mode as discussed earlier with the help of Lyddane-Sachs-Teller (**LST**) relation (Equation 1.1). In similar fashion, the anomaly in dielectric constant can be observed when the phase transition occurs from one ferroelectric phase to another ferroelectric phase. The anomalies that arise in the dielectric data show a direct relationship with the involvement of phonons during the structural phase transitions and provide supporting information for the X-ray and neutron diffraction results.

The dielectric constants were measured using a frequency-response analyser (Novocontrol TB-Analyser). A closed-cycle refrigerator with a He-gas exchange was used for cooling the sample down to 5 K. The high-temperature dielectric measurements were carried out by using a furnace with a heating rate of 2 K/min.

2.2.7.2 Polarization Study: Ferroelectric-Loop Measurement

Ferroelectricity in the samples is confirmed by the ferroelectric hysteresis loop measurements. The ferroelectric loop measurements are being done using a ferroelectric loop tracer based on the principle of Swayer-Tower method. The ferroelectric hysteresis loop provides information about the saturation polarization and the coercive electric field (E_C) required to depolarize the sample. These phase transitions can also be identified by changing the behaviour of the ferroelectric loops as a function of temperature. The polarization versus electric field (P-E) hysteresis loops at selected temperatures were studied using a ferroelectric loop (P-E) tracer of M/s Radiant Instruments, USA.

Chapter 3: Structural Phase Transitions in Modified Sodium Niobate: A Powder X-Ray Diffraction Study

This chapter is based on our published article Physical Review Materials, 2017, 1, 074411, contains the results obtained from a combination of dielectric and X-ray diffraction measurements for compositionally designed (1-x) $NaNbO_3$ -x$BaTiO_3$ (NNBTx), which can induce inter-ferroelectric instabilities.

The physics of ABO_3 perovskite oxides and their functional properties are governed by polar lattice distortion and antiferrodistortive (AFD) tilts of BO_6 octahedra network.[31, 72-77] The polar lattice distortion leads to ferroelectricity, while the latter often has a dramatic impact over the stabilization of complex structures and having multiple cell parameters with respect to the high-temperature cubic phase. A balance between both types of lattice distortions is delicate as their mutual couplings are governed by a subtle interplay of short-range covalency (related to B-O bonding) and long-range electrostatic (or elastic) effects[78]. $NaNbO_3$ is a suitable model system for understanding the lattice distortions. This system exhibits one of the most complex sequences of structural phase transitions [33, 38, 54, 55] in the perovskite family (see section 1.6.2.2). The lattice distortion can be tuned by application of chemical pressure which potentially modifies its physical properties.

Sodium niobate and its derivatives are exotic materials that find applications in technology. Sodium niobate is an antiferroelectric material at room temperature and exhibits a unique property of the double hysteresis loop. This unique property can be exploited for novel four-state non-volatile memory effect. Derivatives of alkaline niobate are promising candidates for lead-free and eco-friendly piezo-ceramics.

In search of high-performance lead-free piezoelectric materials, we compositionally designed (1-x)$NaNbO_3$-x$BaTiO_3$, (NNBTx) materials, which can induce inter-ferroelectric instabilities leading to morphotropic phase boundaries near room temperature. The solid solutions of NNBTx are analogous to solid solutions of (1-x)$PbZrO_3$-x$PbTiO_3$, where one end-member is antiferroelectric while the other end-member is ferroelectric in nature and expected to show anomalous behaviour. In addition to this, the formation of long-range polar order is inhibited by random field and random bonds in the solid solutions having multiple cations with different sizes, valences, or polarizabilities occupying crystallographic equivalent sites. As a result, the short-range ordered relaxor (R) state is expected to form. Relaxor-based solid solutions are used in a wide variety of piezoelectric applications owing to their excellent electromechanical properties.

The solid solutions (NNBTx) have been widely investigated due to the relaxor behaviour obtained in various compositions [58, 62, 79]. Recently, Zuo *et.al* [62] have reported a giant electrostrictive effect in the NNBTx relaxor ferroelectrics for the compositions x=0.15-0.25. So far, NNBTx solid solutions have been studied with the main focus on their dielectric properties and relaxor behaviour. The doping of a small amount of $BaTiO_3$ is expected to distort the sodium niobate lattice and show a variety of structural phase transitions as a function of composition and temperature. The aim of the present study is to investigate the effect of chemical pressure (by doping of $BaTiO_3$) on $NaNbO_3$ at room temperature and its consequences on the phase stability of sodium niobate at high temperature.

We have carried out systematic temperature-dependent X-ray diffraction measurements in conjunction with dielectric measurements. The dielectric measurements for NNBTx show anomalies with compositions as well as at different temperatures. To explore if there is any structural change as a function of composition and temperature, we analysed the powder X-ray diffraction data for various compositions and temperatures. We observed appearance/disappearance of the superlattice reflections along with change in the intensities of the main cubic perovskite peaks in powder X-ray diffraction data, which provide clear evidences for structural phase transitions with composition and temperature. For the composition x=0.03, we observed stabilization of a monoclinic phase (**Cc**), which is nor seen for either of the end member nor alkaline niobates. This monoclinic phase is believed to provide for a flexible polarization rotation and also considered to be directly linked to the high-performance piezoelectricity in materials.

3.1 Phase Stability of in NNBTx (0.0 ≤ x ≤ 0.20) at Room Temperature

Figure 3.1 shows the X-ray powder diffraction Bragg profiles of a few selected peaks of NNBTx in the composition range $0.0 \leq x \leq 0.20$. The X-ray diffraction patterns contain main cubic perovskite Bragg peaks at around $2\theta \sim 32.1^\circ$ 40.1° 46° and labelled as $\{110\}_{pc}$, $\{111\}_{pc}$, and $\{200\}_{pc}$, respectively. Other peaks at around $2\theta \sim 36.2^\circ$, 38.5°, and 43.5° and marked with S1, S2 and S3 respectively, are referred to as superlattice reflections. At the visual level, we observed an abrupt change in the peak position of Bragg profile in superlattice reflection S1 followed by a reduction in their width on increasing $BaTiO_3$ content form x=0.01 to 0.02. We also observed a dramatic change in the Bragg profile of $\{111\}_{pc}$ with the enhancement of the intensity of superlattice reflection S3. Further, on increasing $BaTiO_3$ content, x> 0.02, the intensities of S1 and S2 superlattice reflections decrease. The superlattice reflections S2 and S1 disappear in the composition range x>0.07 and x >0.15 respectively. For the composition x> 0.10, we observed the appearance of additional reflections and one of them is marked with **Im**. Appearance/disappearance and susceptible change in main Bragg peaks clearly suggest a change in crystal structure with composition.

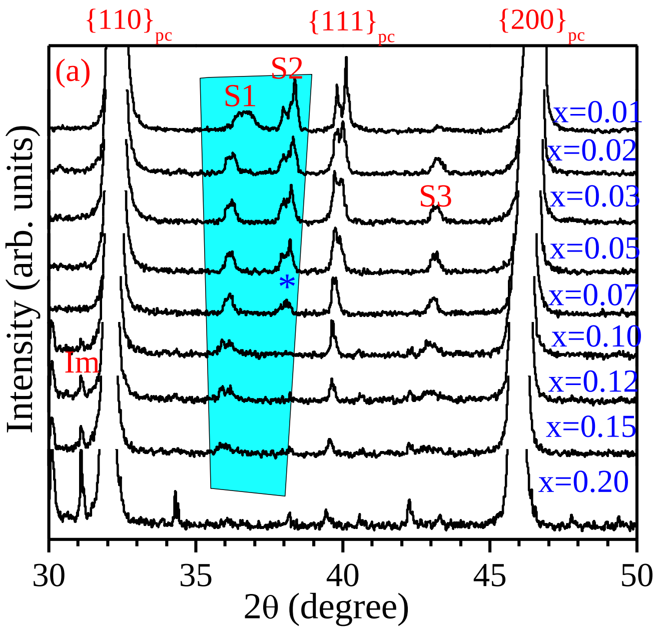

Figure 3.1 Evolution of powder X-ray diffraction patterns, with composition at room temperature.

Pure sodium niobate has antiferroelectric orthorhombic (**Pbcm**) structure at room temperature. Hence, the powder diffraction data of composition x=0.01 was refined using this phase. The fit between the observed and calculated profiles is satisfactory and all the reflections are accounted. Attempts to employ the same orthorhombic structural model in the refinements for x>0.01 are found to be unsatisfactory (see Figure 3.2 (a) and (b)). The most apparent signature of the subtle structural transformation that occurs for x> 0.01 is the inability of orthorhombic structure (space group Pbcm) to account satisfactorily for the superlattice peaks S1 and S3 (around 2θ~ 36.2° and 43.5°). Thus, dramatic change in the Bragg profile and movement of peaks around 36.8 degrees to lower two-theta in powder diffraction provide evidence for structural phase transitions in NNBTx with composition x > 0.01.

To index these superlattice reflections, we explored various possibilities and found that the orthorhombic structure with space group **Pmc2₁** and cell dimensions √2×√2×2 (with respect to elementary cubic perovskite cell) indexed all the reflections. The fit between the observed and calculated profiles is found to be satisfactory (Figure 3.2 (a)). The refined structural parameters are given in Table 3.1. We found that all the reflections present in powder X-ray diffraction in the composition range $0.02 \leq x \leq 0.07$ are accounted using the same structure. This structure is identified as ferroelectric in nature by its symmetry. Structural parameters obtained by detailed Rietveld analysis of powder diffraction data show that the pseudo-cubic cell parameters a_p, b_p and c_p come closer and there is a monotonic increase in the cell parameters as we increase the amount of the dopants.

For the composition $x> 0.07$, attempts to employ the same orthorhombic structural model in the refinement proved unsatisfactory. The most apparent signature of the subtle structural transformation that occurs for composition $x=0.10$ is the inability of the orthorhombic structure to account satisfactory for the S1 superlattice reflection (see Figure 3.2 (b)) top panel. The evolution of powder X-ray diffraction with composition in Figure 3.1 also shows that the superlattice reflection marked with S2 diminishes for $x > 0.07$, which confirm the change in crystal structure at this composition.

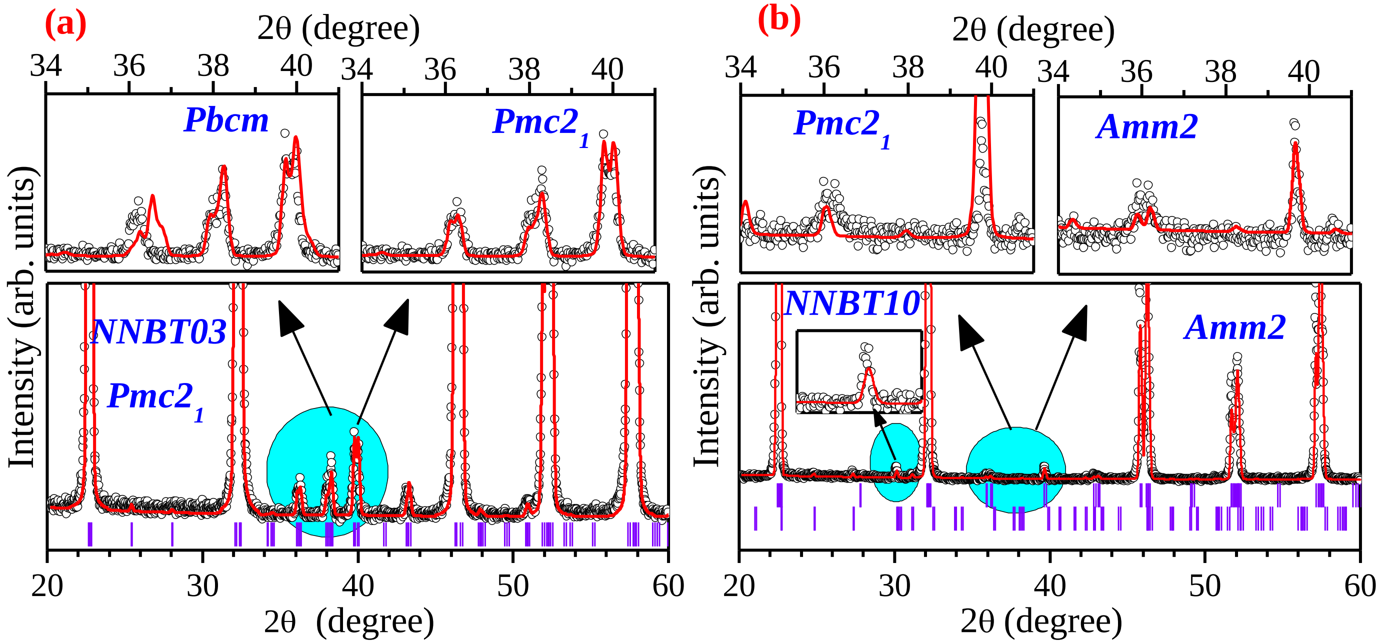

Figure 3.2 Results of Rietveld refinement using different crystal structure with **Pbcm**, **Pmc2$_1$**, and **Amm2** space groups (a and b) with observed (circles) and calculated (solid line) data.

Table 3.1 Structural parameters of NNBTx with x=0.03 obtained by Rietveld refinement of powder X-ray diffraction at room temperature.

		Composition x=0.03 at T= 300 K **Space group Pmc2$_1$**			
Atoms	**Site**	**Positional Coordinates**			
		x	**y**	**z**	**B (Å^2)**
Na1/Ba1	2a	0.000	0.241(3)	0.786(3)	1.13(2)
Na2/Ba2	2b	0.500	0.243(2)	0.770(4)	0.63(4)
Nb/Ti	4c	0.7447(6)	0.7486(7)	0.7932(2)	0.43(2)
O1	2a	0.0000	0.186(6)	0.305(4)	1.18(6)
O2	2b	0.5000	0.289(7)	0.313(2)	1.92(2)
O3	4c	0.224(3)	0.547(3)	0.109(6)	1.35(4)
O4	4c	0.275(3)	-0.022(3)	0.543(3)	1.51(4)

a_o= 7.79290(4) (Å); b_o= 5.52699 (7) (Å); c_o= 5.57476 (7) (Å); unit cell volume= 240.112(5) (Å^3)

R_p= 9.41; R_{wp}= 13.7; R_{exp}= 9.14; χ^2= 2.23

The P–E loops of the NNBTx ceramics are measured at room temperature, which exhibits a well-saturated P–E loop and confirm ferroelectricity in this composition range [62, 79]. Thus, based on the different symmetries of structural distortions reported for perovskite ferroelectric compounds/ solid solutions, different simple symmetry distortions were considered: (i) tetragonal (space group **P4mm**), (ii) orthorhombic (space group **Bmm2**), and (iii) rhombohedral (space group **R3m**) type distortions in structures of $BaTiO_3$ at different temperatures; and (iv) monoclinic distortion of the **Cm** and **Pm** type reported for the morphotropic phase boundary compositions of lead-based solid solutions having perovskite structure. However, these structures are not able to index the S1 superlattice reflection. It is remarkable to notice that S1 and S2 superlattice reflections arise due to in-phase/anti-phase rotation of BO_6 octahedra and are associated with zone boundary M and R points in the

Brillouin zone. However, ferroelectricity is linked with the zone centre (Gamma Point) instability[80]. As per the Glazer classification for tilt systems, S3 is associated with cationic displacement, S3 is not associated with any specific point in the Brillouin zone.

To identify the crystal structure for the composition x > 0.07, we derived the structure by combining irreducible representations (irreps) using the software package ISOTROPY and obtained many space groups as listed in Ref. [37]. We found that the orthorhombic phase with space group **Amm2** accounted nearly all the reflections. In the space group **Amm2**, for the description of the crystal structure, we used the orthorhombic axes: $a_o = a_p$; $b_o = 2b_p$ and $c_o = 2c_p$. The orthorhombic unit cell contains eight formula units. The asymmetric unit of the structure consists of Na/Ba atom at the 4d site at (0, ¾ ±v, 0±w), Nb/Ti atom at the 2b site at (½, 0, ¼±w) and (½, ½, ¼±w). Five oxygen atoms occupies at the 2a site at (0, 0, ¼±w); (0, ½ , ¼±w); 4e site at (½, ¾±v, ¼±w) and 2b site at (½, 0, 0) and (½, ½, 0±w) respectively. The fit between the observed and calculated profiles is quite satisfactory and includes the weak superlattice reflections. However, some reflection appeared at 2θ~24.79˚, 27.3˚ and 30.1˚. One of the strongest reflections, which is marked as **Im** in the powder diffraction pattern, yet cannot be indexed using this crystal structure. The refined structural parameters are given in Table 3.2. We find some discrepancy in intensity (see inset Figure 3.2 (b)). We found that these peaks could correspond to $Ba_3Nb_4Ti_4O_{21}$ and hence, we performed two phase refinement the results suggest that the content of the undesired $Ba_3Nb_4Ti_4O_{21}$ phase is about ~1% and it increases upto 3% on increasing $BaTiO_3$ content to x=0.20.

Table 3.2 Structural parameters of NNBTx with x=0.10 obtained by Rietveld refinement of powder X-ray diffraction at room temperature.

Atoms	**Site**	**Composition x=0.10 at T=300 K Space group Amm2**			
		Positional Coordinates			
		x	**y**	**z**	**B (Å^2)**
Na1/Ba1	4d	0.000	0.759(6)	-0.003(2)	1.03(5)
Nb1/Ti1	2b	0.500	0.000	0.246(7)	0.55(9)
Nb2/Ti2	2b	0.500	0.500	0.247(5)	0.42(1)
O1	2a	0.000	0.000	0.300(8)	1.0391)
O2	2a	0.000	0.500	0.221(5)	1.38(9)
O3	4e	0.500	0.752(6)	0.284(3)	1.58(7)
O4	2b	0.500	0.000	0.009(2)	1.15(7)
O5	2b	0.500	0.500	0.000(1)	1.55(2)

a_o= 3.92523(4) (Å); b_o= 7.91443(6) (Å); c_o= 7.83494 (8) (Å); unit cell volume= 243.400(4) (Å^3)

R_p= 11.4; R_{wp}= 15.2; R_{exp}= 10.14; χ^2= 2.26

For comparison, we plotted the volume (equivalent to cubic perovskite primitive cell) with composition in Figure 3.3. It is evident from this figure that on increasing $BaTiO_3$ content the volume increases, and shows a distinct change in slope at about x=0.09. For a complete understanding of the correlation of structural phase transition on its physical properties, the results obtained from diffraction techniques need to be corroborated by other techniques. We measured the variation of dielectric constant at 10 kHz with the composition (see Figure 3.3) and found that it increases on increasing composition.

3.2 Phase Stability in NNBT03 with Temperature

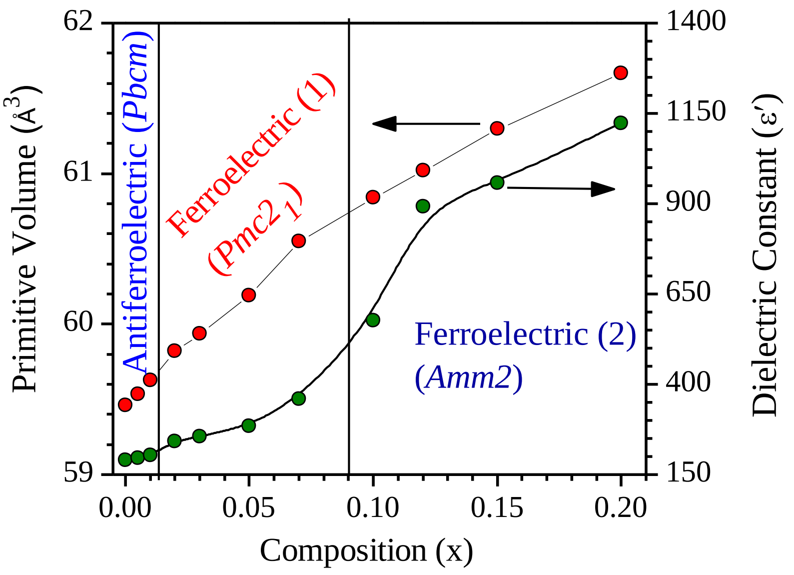

Figure 3.3 Variation of volume (equivalent to cubic perovskite primitive cell) and dielectric constant at 10 kHz with composition.

It is clear from the foregoing results that with increasing the content of $BaTiO_3$ in sodium niobate matrix, its antiferroelectric phase is destabilized and transforms to a ferroelectric phase at room temperature. To investigate the effect of $BaTiO_3$ doping, on the phase stability of $NaNbO_3$ with temperature, we carried out detailed studies for the composition x=0.03, as a function of temperature. The composition was chosen by keeping in mind that it should be closer to pure sodium niobate but with a different structure.

3.2.1 Dielectric Study

The structural phase transition in this material may accompany with the anomaly in physical properties, we have performed a temperature-dependent dielectric measurement. The variation of dielectric constant as a function of temperature at 10 kHz for x=0.03 in the temperature range 5- 640 K is depicted in Figure 3.4. It is evident from this figure that on heating from 5 K, the dielectric constant increases and shows anomalies around 250, 500 and

623 K, respectively. The dielectric data show dispersion with frequency (not shown here). The dispersion behavior is similar to that observed in relaxor ferroelectrics wherein the formation of polar nano-regions affects the relaxation dynamics. To explore the structural changes as a function of temperature, we performed a powder X-ray diffraction study in the temperature range 12- 900 K.

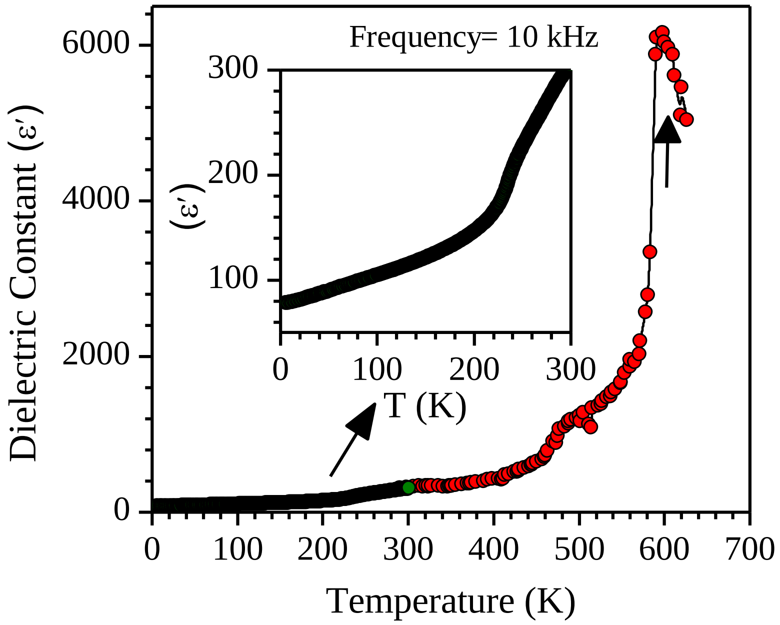

Figure 3.4 The variation of dielectric constant as a function of temperature at 10 kHz for x=0.03 in the temperature range 5- 640 K.

3.2.2 X-Ray Powder Diffraction Study

Figure 3.5 (a and b) depicts a portion of the powder X-ray diffraction patterns of the composition x=0.03 in selected temperatures in the range of 12–873 K. The diffraction data were collected in the heating cycle. At room temperature, the powder diffraction pattern consists of two types of reflections, viz., main peaks of cubic perovskite structure labeled as $\{110\}_{pc}$, $\{111\}_{pc}$ and $\{200\}_{pc}$ and additional reflections are known as the superlattice reflections that are labeled as S1, S2 and S3.

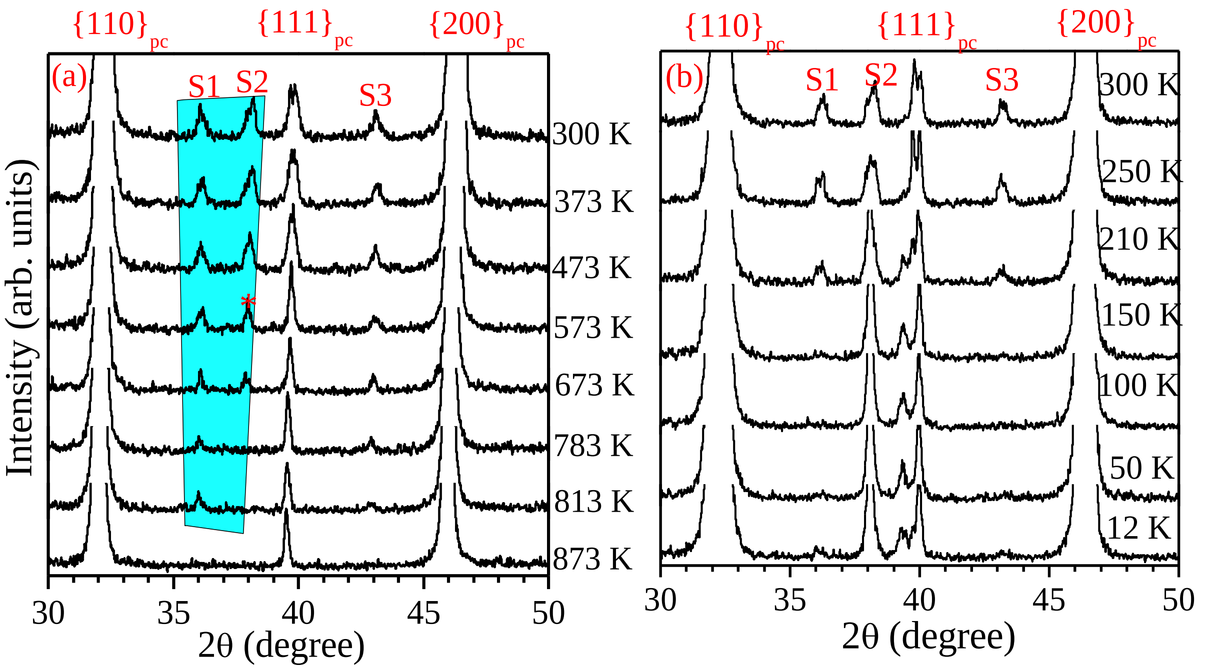

Figure 3.5 Evolution of temperature-dependent powder X-ray diffraction patterns, above (a) and below (b) room temperature for x=0.03.

It is evident from Figure 3.5 (a) that on increasing temperature from 300 K, intensity of S1, S2 and S3 superlattice reflections decreases and finally vanishes above 813 K. The disappearance of superlattice reflections at different temperature (S1~ 813 K and S2-S3 above 673 K) clearly revealed one or more structural phase transformations across these temperatures. In addition to this, we found the splitting of $\{111\}_{pc}$ main perovskite peaks diminishes and becomes singlet at high temperature. Indeed, we found a strong modification in all main peaks of perovskite structure in terms of its splitting and intensities in the entire range. Further, on cooling below room temperature from 300 K, it can be clearly seen (Figure 3.5 (b)) that the intensity of S1 and S3 superlattice reflections decreases while that of S2 superlattice reflection increases. We also see a clear splitting in the main perovskite peak $\{111\}_{pc}$. It is remarkable to notice that we have found a drastic change at a higher angle also. The disappearance of superlattice reflection and splitting in main peak provide a signature for the structural phase transition below 300 K.

3.2.3 Identification of Crystal Structure ($12 \leq T \leq 873$ K)

To obtain the crystal structure of various phases as a function of temperatures, we performed detailed Rietveld analysis of the powder X-ray diffraction patterns in the entire temperature range. At highest measured temperature (873 K), all the Bragg reflections present in the powder diffraction patterns could be indexed using a cubic phase. The tetragonal symmetry (space group **P4/mbm** phase) is found in the temperature regime from 843 K to 773 K and an orthorhombic symmetry with space group **Cmcm** (O1 phase) in the temperature regime from 756 K to 647 K. All the refinements converged smoothly and fitting between the observed and calculated profiles was satisfactory. Attempt to employ the same space group below 647 K, at 573 K, is found to be unsatisfactory, which indicates a different structure. The compound has an orthorhombic **$Pmc2_1$** structure at room temperature, so we tried to refine the powder diffraction data using this space group. But, Rietveld fitting was not significantly improved. Further, we refined the data of 573 K using phase coexistence of orthorhombic phases (**$Pmc2_1$+ Cmcm**) and found that it improved the fit significantly. Finally, below 473 K to 250 K, all data could be refined using the orthorhombic ferroelectric phase O2 (Space group: **$Pmc2_1$**). The Rietveld refinements proceeded smoothly, revealing a monotonic decrease in lattice constants and cell volume with decreasing temperature. However, attempts to employ the same orthorhombic structural model in the refinements below 250 K proved unsatisfactory, and a progressive worsening of the quality of the Rietveld fits with decreasing temperature was found. The most apparent signature of the subtle structural transformation that occurs below 250 K is the inability of orthorhombic structure to account satisfactory for a peak around 40.0°.

Recently, Mishra *et. al.* have employed systematic neutron diffraction measurements as a function of temperature to study the low-temperature structures and to understand the phase transitions of $NaNbO_3$[54, 78] and its solid solution $(Na/Li)NbO_3$[81, 82]. These studies present unambiguous evidence for the presence of the ferroelectric **R3c** phase at low temperature. Therefore, we refined the powder X-ray diffraction data of NNBTx for x=0.03 at 12 K using the rhombohedral **R3c** phase (Figure 3.6). The structural parameters are given in Table 3.3. The unsatisfactory quality of the Rietveld fit of the diffraction data suggests that the rhombohedral phase is not favoured in this compound. We tried to refine the powder X-ray diffraction data using different crystal structures that other perovskites ($PbTiO_3$ and $BaTiO_3$) exhibit at different condition but none of these space groups accounted all the Braggs peaks. We have further extended our search on different crystal structures which have S2 type superlattice reflections (associated with R point instability) and ferroelectric in nature. We found that a monoclinic phase with space group **Cc** accounted nearly all the reflections at the lowest temperature of 12 K. In the space group **Cc**, for the description of the crystal structure, we used the following monoclinic axes: $a_m = a_p+b_p+2c_p$; $b_m = a_p-b_p$ and $c_m = a_p+b_p$. The monoclinic unit cell contains 4 formula units. The asymmetric unit of the structure consists of Na/Ba atom at 4a site (0±u, ¾ ±v, 0±w), Nb/Ti atom at 4a site (¼±u, ¼±v, ¼±w). Three oxygen atoms occupy the 4a site (0±u, ¼±v, 0±w); (¼±u, ½ ±v, 0±w) and (¼±u, 0±v, ½±w), respectively. The fit between the observed and calculated profiles is quite satisfactory and includes the weak superlattice reflections. However, we find some discrepancy in intensity (see Figure 3.6).

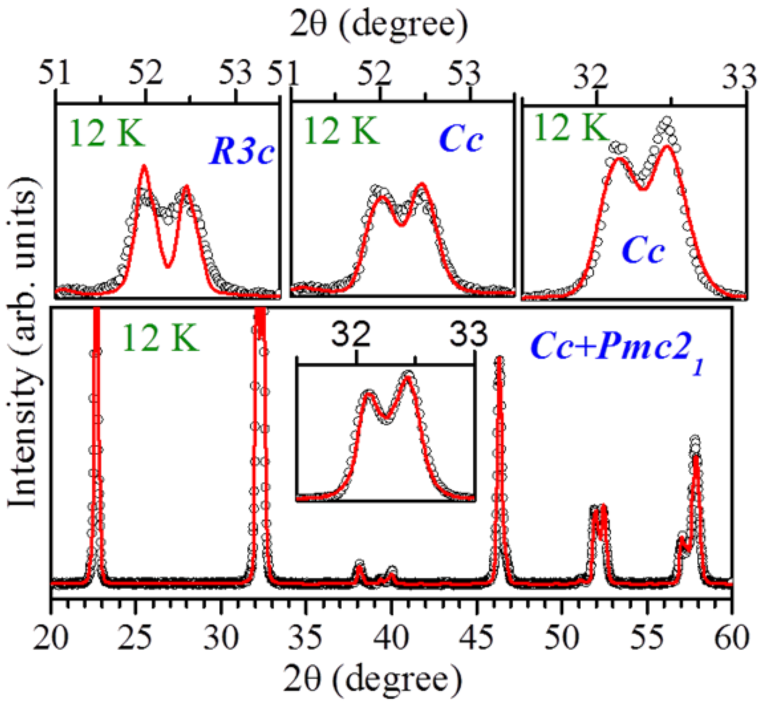

Figure 3.6 The results of Rietveld refinement fitting of the observed (circles) and calculated (solid line) data using different crystal structures with **R3c**, **Pmc2$_1$**, and **Cc** space groups.

A two-phase refinement with both the orthorhombic and monoclinic space groups is found to be successful, and all the observed diffraction peaks could be indexed with the improved fit (Figure 3.6 inset). We find that the orthorhombic and monoclinic phases coexist over a large temperature range from 250 to 12 K. The percentage of the orthorhombic phase continuously decreases with lowering temperature and reaches 21% at 12 K. The structural parameters are given in

Table 3.4. The observed monoclinic phase (**Cc**) in NNBTx with x=0.03 is found to be identical to PZT where piezoresponse is ultra-large. This monoclinic phase is believed to provide a flexible polarization rotation and considered to be directly linked to the high-performance piezoelectricity in materials due to presence of an easier axis for spontaneous polarizations. The coexistence of both the phases indicates that the structural phase transition from orthorhombic to monoclinic phase is of first order. The observed coexisting phases and anomalous smearing of the dielectric response is akin to dipolar glasses and relaxor ferroelectrics. The observed monoclinic phase (Cc) in NNBTx with x=0.03 is found to be identical to PZT where the piezoresponse is ultralarge. This monoclinic phase is believed to provide a flexible polarization rotation and is considered to be directly linked to the high-performance piezoelectricity in materials due to the presence of an easier axis for spontaneous polarization.

Table 3.3 Structural parameters of NNBTx with x=0.03 obtained by Rietveld refinement of powder X-ray diffraction at 12 K.

Atoms	**Site**	**Composition x=0.03 at T= 12 K** **Space group** R3c			
		Positional Coordinates			
		x	**y**	**z**	**B (Å^2)**
Na1/Ba1	6a	0.000	0.0000	0.269(3)	0.32(7)
Nb/Ti	6a	0.2675(5)	0.2521(1)	0.0119(3)	0.36(5)
O1	18b	0.113(2)	0.350(3)	0.08106	0.58(5)

a_h= b_h= 5.5092 (2) (Å); c_h= 13.7044 (3) (Å), unit cell Volume= 360.22 (2) (Å^3)

R_p= 19.4; R_{wp}= 25.6; R_{exp}=11.27; χ^2= 5.17

Table 3.4 Structural parameters of NNBTx with x=0.03 obtained by Rietveld refinement of powder X-ray diffraction at 12 K using two phase model monoclinic phase (space group **Cc**) and orthorhombic (space group: **Pmc2$_1$**).

Atoms	**Composition x=0.03 at T= 12 K** **Space group Cc (phase fraction 79%)**					**Composition x=0.03 at T= 12 K** **Space group Pmc2$_1$ (phase fraction 21%)**				
	Site	**Positional Coordinates**				**Site**	**Positional Coordinates**			
		x	**y**	**z**	**B (Å^2)**		**x**	**y**	**z**	**B (Å^2)**
Na1/Ba1	4a	0.000	0.7500	0.0000	0.38(7)	2a	0.000	0.251(4)	0.753(3)	0.04(3)
Na2/Ba2						2b	0.500	0.267(4)	0.751(2)	0.02(1)
Nb/Ti	4a	0.2675(5)	0.2521(1)	0.2711(4)	0.36(5)	4c	0.7472(7)	0.7493(5)	0.7682(2)	0.18(2)
O1	4a	0.034(2)	0.295(3)	0.040(1)	1.21(6)	2a	0.0000	0.253(3)	0.285(6)	0.51(1)
O2	4a	0.312(3)	0.457(2)	0.058(1)	0.42(2)	2b	0.5000	0.260(3)	0.3213(6)	0.98(8)
O3	4a	0.253(3)	0.031(1)	0.599(6)	1.43(4)	4c	0.234(3)	0.494(4)	0.109(6)	0.95(4)
O4						4c	0.296(7)	-0.022(3)	0.483(3)	0.98(9)

a_m= 9.5328(4) (Å); b_m= 5.5110 (2) (Å); c_m= 5.512 (2) (Å), β= 124.63 (1)(degree) ; unit cell volume= 239.87(2) (Å^3)

a_o= 7.7569(9) (Å); b_o= 5.5439 (2) (Å); c_o= 5.5216 (7) (Å), unit cell volume= 237.44(5) (Å^3)

R_p= 13.5; R_{wp}= 18.9; R_{exp}=11.81; χ^2= 2.56

3.2.4 Variation of Structural Parameters

The variation of the pseudo-cubic cell parameters obtained after Rietveld refinement of diffraction data for composition x=0.03 is shown in Figure 3.7 (a). It is evident from the figure that on increasing temperature from 12 K to 250 K, the a_p and c_p parameters increase while the b_p parameter first decreases upto 160 K and finally increases with the increase in temperature.

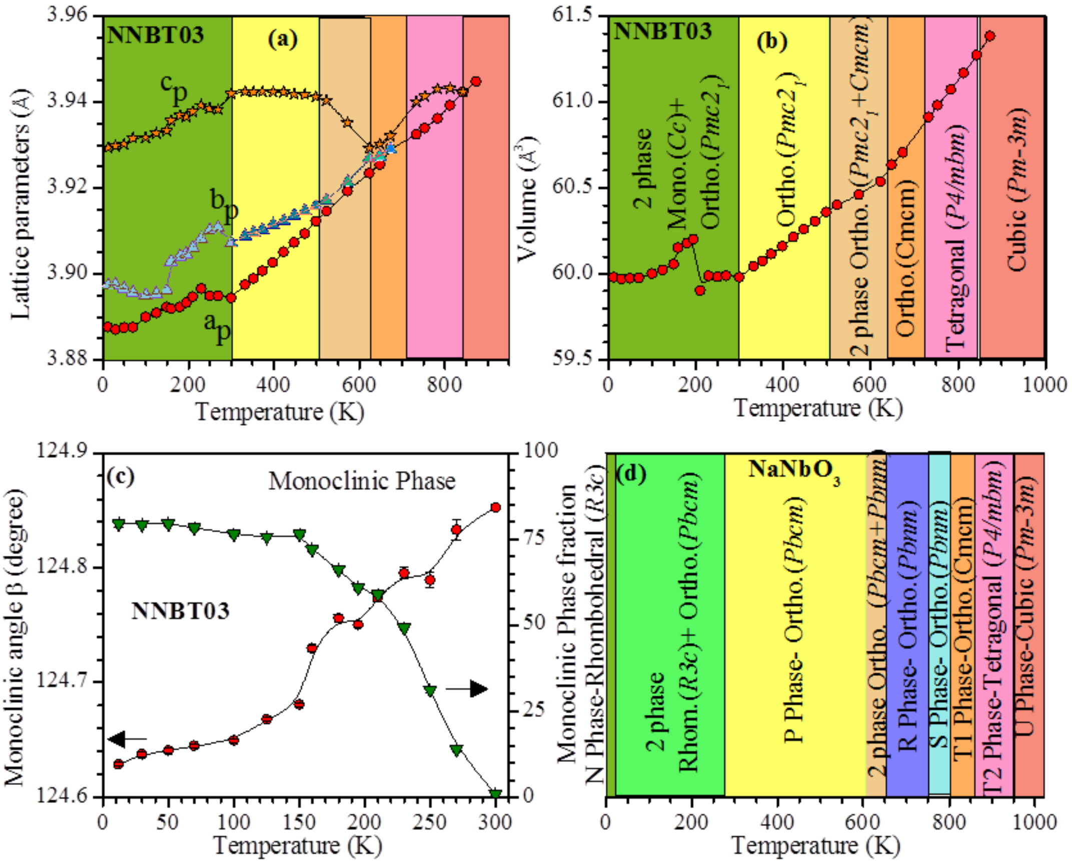

Figure 3.7 The variation of (a) equivalent lattice parameters (b) volume and (c) monoclinic angle and phase fraction with temperature for the composition x=0.03. To compare the effect on chemical pressure on the phase stability of pure sodium niobate[33], the phase diagram is shown in Figure (d).

Above room temperature in the ferroelectric orthorhombic phase (O2 phase), the a_p and b_p parameters increase while the c_p parameter decreases with increase in temperature. All the cell parameters come closure and show discontinuous jump at 573 K, which indicates the first-order phase transition. Upon increasing the temperature around 673 K all the cell parameters increase continuously. Cell parameters a_p and c_p come closure and get merged at 783 K, which is due to the orthorhombic to the tetragonal phase transition. Finally, both the cell parameters approach each other at 873 K and the structure becomes cubic perovskite. Variation of equivalent to cubic perovskite primitive cell volume for the composition x=0.03 is shown in Figure 3.7(b). It is evident from this figure that on increasing temperature, the volume increases and shows an anomaly around 270 K providing a signature of strong first-order phase transition from monoclinic to orthorhombic phase. The variation of monoclinic angle and phase is plotted in Figure 3.7 (c). It is evident from this figure that on the increasing temperature the monoclinic phase fraction decreases and vanishes near 300 K.

3.3 Discussion

Dielectric susceptibility is a measure of the cooperative behavior of dipoles. These dipoles can be categorized into different groups based on their dynamics, and each group has a different contribution to the susceptibility. In general thermal motions prevent dipoles from aligning with the applied electric field. On the other hand, the number of dipoles increases above the critical activation energy. The combined effects of these two factors give rise to the susceptibility peak at a certain temperature. The presence of polar nano-region or random electric fields due to hetrovalent ion strongly influences the dynamics of dipoles.

The temperature-dependent dielectric measurement for composition x=0.03 at given frequency show anomalies around 250, 500 and 623 K, respectively. It is important to notice that we have also seen a change in the crystal structure across these temperatures. The essential structural characteristic of relaxor is compositional disorder i.e. the disorder in the arrangement of different ions on crystallographic equivalent sites. However, the ground state of the complex perovskites should be compositionally ordered, e.g. each type of the cations should be located in its own sublattice, and makes a superstructure with complete translational symmetry. This is because the electrostatic and elastic energies of the structure are minimized in the ordered state due to the difference in both the charge and the size of different ions. Thermal motion is capable of destroying the order at a certain non-zero temperature. This occurs in the form of structural phase transition and shows an anomaly in dielectric data.

As shown in Figure 3.4 the increase of dielectric constant with the increasing composition of $BaTiO_3$ can be understood in terms of mismatch of the ionic radii of cations. In ABO_3 perovskite structure, A- cation is coordinated with 12 oxygen ions and B- cation to 6. The mismatch in radii of A [Na (1.39 Å) and Ba (1.69 Å)] and B cations [(Ti (0.64 Å) and Nb (0.604 Å)] results in slight increase in the volume of the unit cell on doping, and allows larger off-centre displacements of ions which is directly related to the polarization strength. In addition to this, heterovalent ions (with different charges) generate electric field which affects dipole distribution in compounds. We also observed the lowering of the measured ferroelectric transition temperature. This can be rationalized by changes in the unit cell. The phenomenon of transition temperature decreasing with the substitution of larger cations for smaller cations was observed in various perovskites and related structures.

Distinct changes and appearance/disappearance of the superlattice reflections observed in the composition and temperature dependence of powder diffraction patterns of compositionally modified $NaNbO_3$ clearly reveal that it undergoes structural phase transitions. Now we discuss the salient feature of these transitions with composition, temperature, and compare with pure sodium niobate reported in the literature. Using detailed neutron scattering experiment and lattice dynamical calculations, we have shown that structural phase transitions in sodium niobate are linked to freezing of zone boundary phonons along the line T (lying between the M and R points) with (q=1/2, 1/2, g) (where g= 1/12, 1/6, and 1/4).

At ambient condition, the characteristic peaks of the anti-ferroelectric phase appeared around 37.1 degree and associated with condensation of T point phonon. However, the appearance of superlattice reflection S1 and S2 marked in present powder diffraction are result of the freezing of M and R points instability. On increasing $BaTiO_3$ content in $NaNbO_3$ for x=0.02, we found the characteristic antiferroelectric peaks disappear and become ferroelectric in nature. Further, increasing $BaTiO_3$ concentration, the superlattice peaks associated with R point disappear and only superlattice peaks arising due to M point is left in the powder diffraction patterns. It is clear from this discussion that increasing the concentration of $BaTiO_3$ suppressed the anti-phase rotation of octahedra.

To gain a better understanding of the compositional dependence of the polar and anti-ferrodisrtive distortion, we computed the amplitude mode of these distortions with respect to the cubic phase and shown in Figure 3.8. As said earlier that on increasing concentration of $BaTiO_3$ in $NaNbO_3$, One observes structural phase transitions. These transitions are mainly associated with polar (GM4-) and antiferrodistortive distortions (R and M points). It is evident from this figure that on increasing the concentration of $BaTiO_3$ polar mode (GM4-) first decreases up to x=0.05 and then increases. On the other hand, value of one of antiferrodistortive mode (M3+) increases up to x=0.07 and then decreases with concentration. However, value (R4+) of antiferrodistortive mode decreases sharply and vanishes for x> 0.07. Figure 3.8 (b) shows the variation of distortion and c/a ratio of primitive lattice parameters which also shows anomaly across the phase transition compositions. It is evident from this that suppression of in-phase rotation of octahedra and increment in tetragonality (c/a ration) promotes the polar mode.

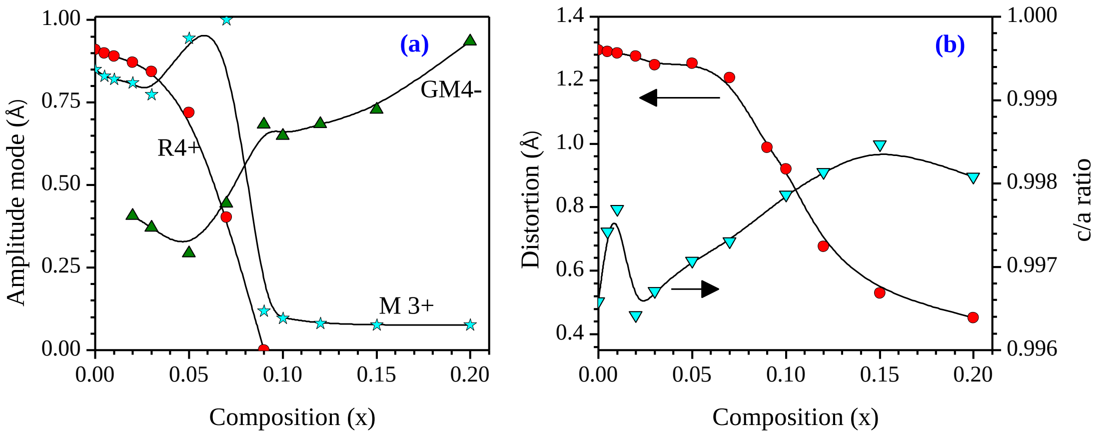

Figure 3.8 The variation of (a) amplitude of polar and antiferrodistortive mode and (b) distortion and tetragonality with composition at room temperature.

Now, we see the effect of chemical pressure on phase stability of sodium niobate with temperature. In contrast to sodium niobate which has an antiferroelectric and centrosymmetric structure at room temperature, NNBTx with x=0.03 is ferroelectric with non-centrosymmetric structure. The absence of orthorhombic S, R (space group: Pbnm with different cell size), and P (space group: **Pbcm**) phases of sodium niobate (see Figure 3.7 (d)) clearly suggest that phonons related to T points instabilities do not play a role in structural phase transitions in NNBTx with x=0.03. Instead of the phase transition from orthorhombic O1 (space group: Cmcm) to ferroelectric orthorhombic O2 (space group: **Pmc2$_1$**) phase is linked with the freezing of a zone centre phonon. This clearly highlights that the microscopic origin of these phase transitions is significantly different in the two materials. This shows that a slight variation of composition from pure sodium niobate to NNBTx with x=0.03 dramatically changes the underlying physics of their behavior.

3.4 Conclusion

We have carried out a systematic composition and temperature-dependent X-ray measurements in conjunction with dielectric measurements in NNBTx[3]. The dielectric measurements exhibit anomalies with compositions and at different temperatures for NNBT03. To explore if there is any structural change as a function of composition and temperature, we analyzed the powder X-ray diffraction data for various compositions and temperatures. We observed appearance/disappearance of the superlattice reflections along with the change in the intensities of main perovskite peaks in powder X-ray diffraction data, which provide clear evidences for structural phase transitions with composition and temperature. We found that suppression of in-phase rotation of octahedra and increment in tetragonality (c/a ratio) promotes polar mode. It is interesting to note that a slight variation in composition in NNBTx around x=0.03 dramatically change the phase transition behavior and its underlying physics in terms of the phonon softening and the Gibbs free energy variations.

Chapter 4: Structural Phase Transitions in NNBTx (x=0.03 & 0.05) : A Powder Neutron Diffraction Study

This chapter is based on our published article Appl. Phys. Lett. 112, 182905. It contains the results obtained from a combination of dielectric and neutron diffraction measurement for compositionally design of (1-x)$NaNbO_3$-x$BaTiO_3$:NNBTx for x~0.03 and 0.05, which showed ferroelectric behaviour at ambient conditions as described in chapter 3.

In the previous chapter, we found that the ferroelectric rhombohedral phase of pure sodium niobate gets suppressed for the composition x=0.03 using a temperature-dependent powder X-ray diffraction study. These phase transitions are associated with the position of oxygen atoms. Neutron diffraction study offers certain advantages over X-rays especially in the accurate determination of the oxygen positions.

In this present study, we have carried out a systematic temperature-dependent neutron diffraction measurements in conjunction with dielectric spectroscopy of NNBTx with x=0.03 and 0.05 from 6 to 300 K. The temperature-dependent dielectric constant measurement shows dispersion with frequency, which suggests a relaxor ferroelectric behaviour. It also exhibits anomalies at different temperatures in cooling and heating cycles and exhibits a large thermal hysteresis of ∼150 K. This provides a signature for the first-order nature of phase transition across this temperature. To explore if there is any structural change as a function of temperature, we analysed the powder neutron diffraction data. We observed stabilization of the monoclinic phase (**Cc**) which is identical to PZT where piezoresponse is ultra-large. This monoclinic phase is believed to provide a flexible polarization rotation and also considered to be directly linked to the high-performance piezoelectricity in materials.

4.1 Variation of Dielectric Constant as a function of Temperature

Figure 4.1 show the variation of dielectric constant as a function of temperature for NNBT03 at selected frequencies namely 1, 10 and 100 kHz. It is evident from this figure that on cooling from room temperature, the magnitude of dielectric permittivity value decreases from 300 (at 300K) to 70 (at 5 K) with an anomaly around 160 K. Further, on heating from 5 K, it increases and shows anomaly around ~ 250 K. The dielectric data show dispersion with frequency.

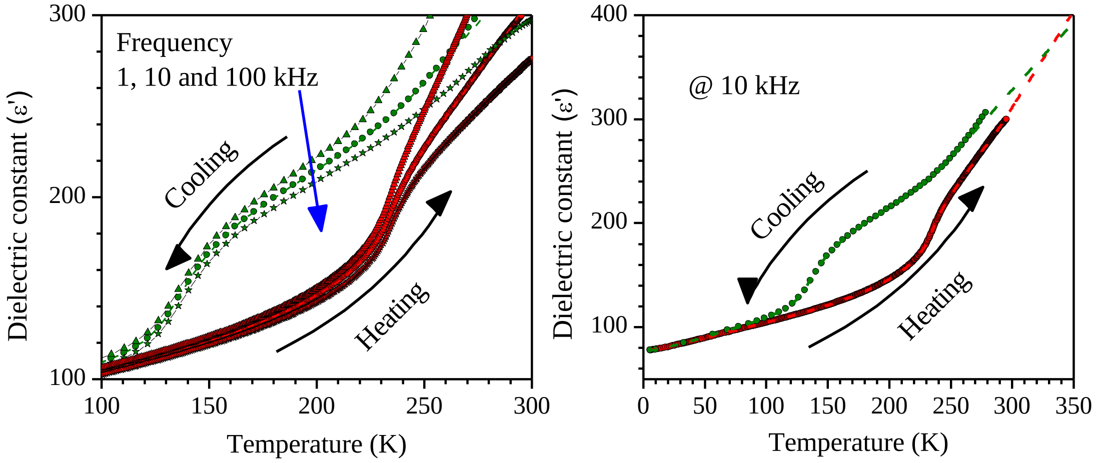

Figure 4.1 Temperature variation of dielectric constant of $0.97NaNbO_3$-$0.03BaTiO_3$: NNBT03 at selected frequencies.

The observed weak relaxor behaviour in NNBTx is due to the competing structural instabilities, rather than due to the structural heterogeneities in the classical relaxor Pb $(Mg_{1/3}Nb_{2/3})O_3$ (PMN)[83]. It is also important to notice that these anomalies occur at different temperatures in cooling and heating cycles and exhibit a large thermal hysteresis of ~150 K. This provides a signature for the first-order nature of the phase transition across this temperature. To explore if there is any structural change as a function of temperature, we have performed a powder neutron diffraction experiment.

4.2 Evolution of Powder Neutron Diffraction as a function of Temperature

Figure 4.2 and Figure 4.3 depicts a portion of the powder neutron diffraction patterns of (1-x) $NaNbO_3$ -x$BaTiO_3$ for x=0.03 and 0.05, at selected temperatures in the range of 6–300 K for cooling and heating cycles. The powder diffraction pattern consists of two types of reflections, viz., main peaks of the perovskite structure (as seen in cubic phase) and additional reflections known as superlattice reflections. These superlattice reflections are a result of the octahedral tilting and are associated with zone boundary instability. The main peaks of perovskite structure can be noticed at around 2θ ~ 18.3°, 25.8°, 32.1°, 37.1° and 41.8° and superlattice peaks appear around 2θ ~ 28.9°, 30.6°, 34.6°, 37.1° and 40.8° at room temperature. It is evident from Figure 4.2 and Figure 4.3 that there is a drastic change in the profile near 2θ ~ 30.6°, 32.1° and 34.6° in the diffraction pattern below 200 K during cooling and above 190 K in heating cycles, respectively. As we lowered the temperature from 300 K, the intensity of the superlattice reflections at around 2θ ~ 28.9° and 34.6° decreases while the intensity of peak around 2θ ~30.6° increases. We also see a splitting in the main perovskite peak around 32.1°. The disappearance of superlattice reflection and the splitting in the main peaks provide a signature for structural phase transition in both compounds.

One of the end-member, sodium niobite is an antiferroelectric phase with space group **Pbcm** at room temperature 300 K. The antiferroelectric phase consists of two or more sublattice polarizations of antiparallel nature, which in turn give rise to superlattice reflections in the diffraction patterns. We have observed such reflections in the antiferroelectric phase, and the strongest one of them appears at 2θ ~ 29.5°. These characterstic antiferroelectric reflections are not present in the powder neutron diffraction pattern of NNBT03 at room temperature, which suggests that it has a different crystal structure at 300 K.

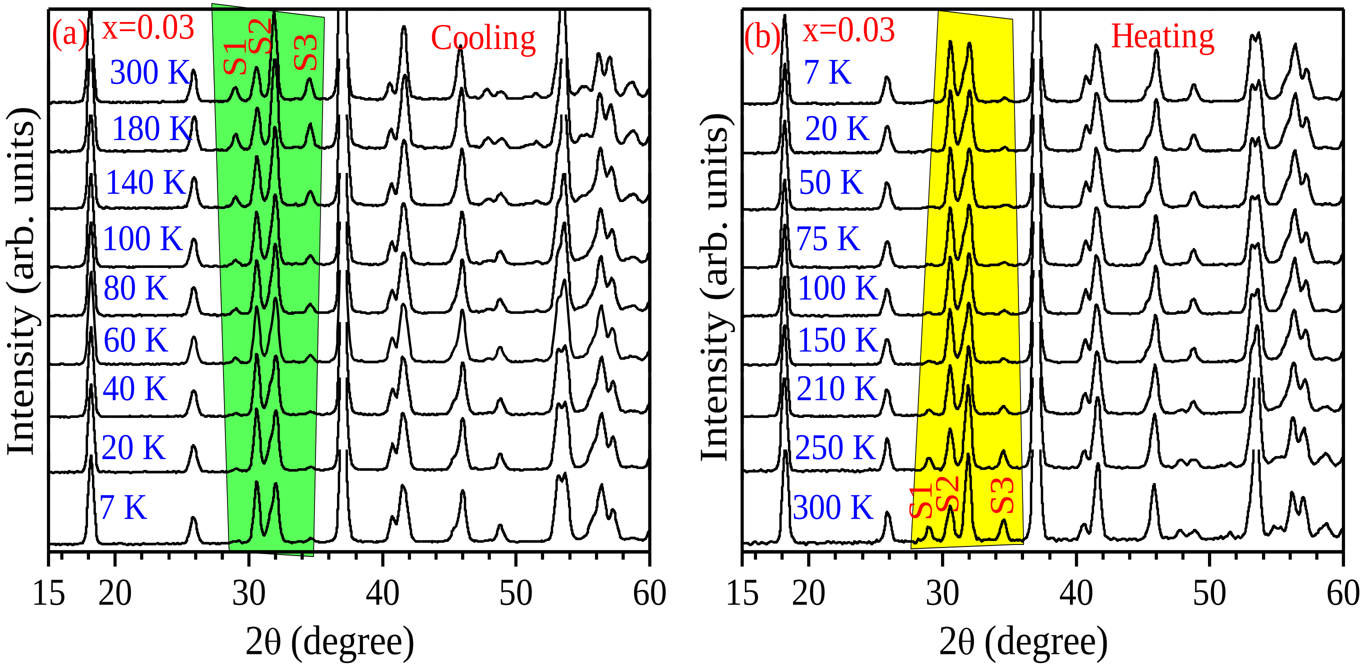

Figure 4.2 Evolution of the neutron diffraction pattern for (1-x)$NaNbO_3$-x$BaTiO_3$ for x=0.03 with temperature in (a) cooling cycle, and (b) heating cycle.

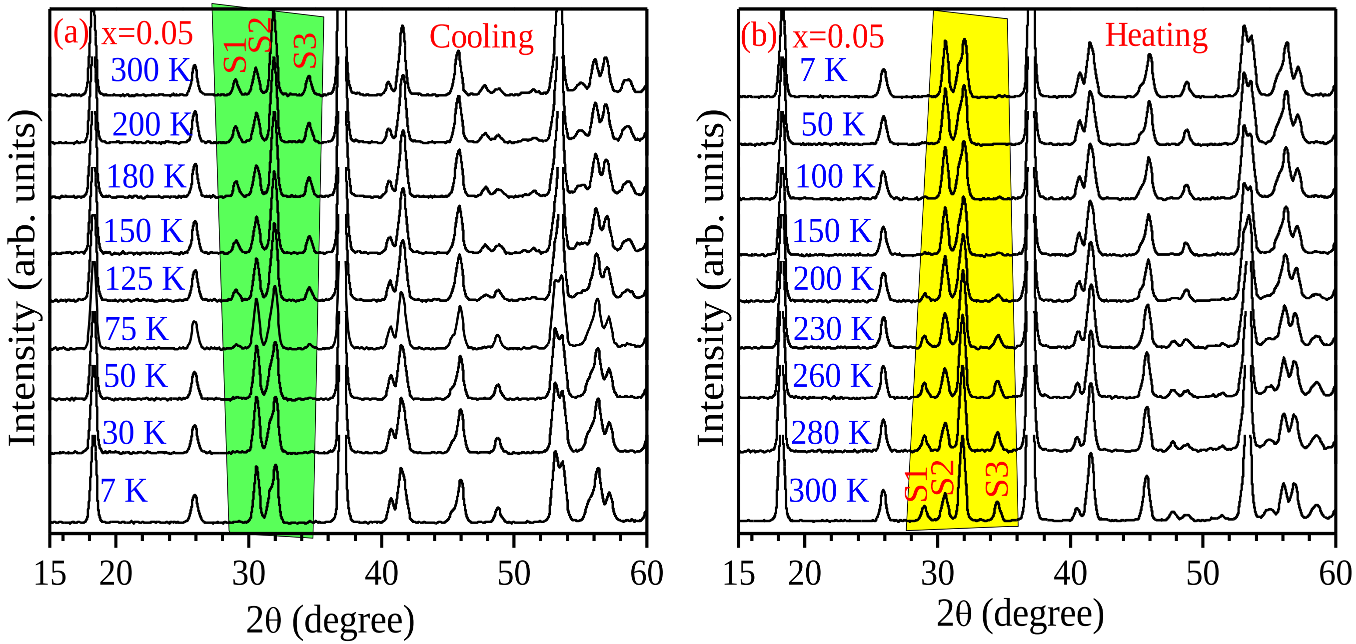

Figure 4.3 Evolution of the neutron diffraction pattern for (1-x)$NaNbO_3$-x$BaTiO_3$ for x=0.05 with temperature in (a) cooling cycle, and (b) heating cycle.

4.3 Identification of crystal structure in temperature range 6 K to 300 K

The doping of small amount of ions such as K^+, Li^+ in pure $NaNbO_3$ imposes chemical pressure which results in the deviation of the crystal structure from its current antiferroelectric phase and stabilization of ferroelectric orthorhombic phase with space group **Pmc2₁** and cell dimensions $2\times\sqrt{2}\times\sqrt{2}$ (with respect to elementary cubic perovskite cell). We refined powder neutron diffraction using this phase and found that all the peaks in the powder neutron diffraction patterns at 300 K could be indexed. The fit between the observed and calculated profiles is found to be satisfactory (Figure **4.4** (a)). This structure is identified as ferroelectric in nature by its symmetry. The structural parameters calculated through Rietveld refinement are given in Table **4.2**. To confirm the ferroelectric nature of system, we carried out P-E hysteresis loop at room temperature for composition x=0.03 and shown in Figure **4.4** (b). It is evident from this figure that composition x=0.03 has ferroelectric loop with applied voltage. This confirms the ferroelectric nature for the samples. We have also carried out P-E hysteresis loop at selected low temperatures (Figure **4.4** (b)). It is evident from this figure that on decreasing temperature, the spontaneous polarization decreases, which is consistent with change in crystal structure.

Detailed Rietveld refinement of the powder-diffraction data shows that diffraction patterns could be indexed using the orthorhombic structure (space group **Pmc2₁**) up to 150 K in cooling cycle. The Rietveld refinements proceeded smoothly, revealing a monotonic decrease in lattice constant and cell volume with decreasing temperature. However, attempts to employ the same orthorhombic structural model in the refinements proved unsatisfactory at lower temperatures, and a progressive worsening of the quality of the Rietveld fits with decreasing temperature was found. The most apparent signature of the subtle structural transformation that occurs below 150 K is the inability of orthorhombic structure to account satisfactory for the peaks around

30.8°. Recently, Mishra *et al.* have employed systematic neutron diffraction measurements as a function of temperature to study the low temperature structures and to understand the phase transitions of $NaNbO_3$ and its solid solution [81, 82] (Na/Li) NbO_3. These studies present unambiguous evidence for the presence of the ferroelectric **R3c** phase at low temperature.

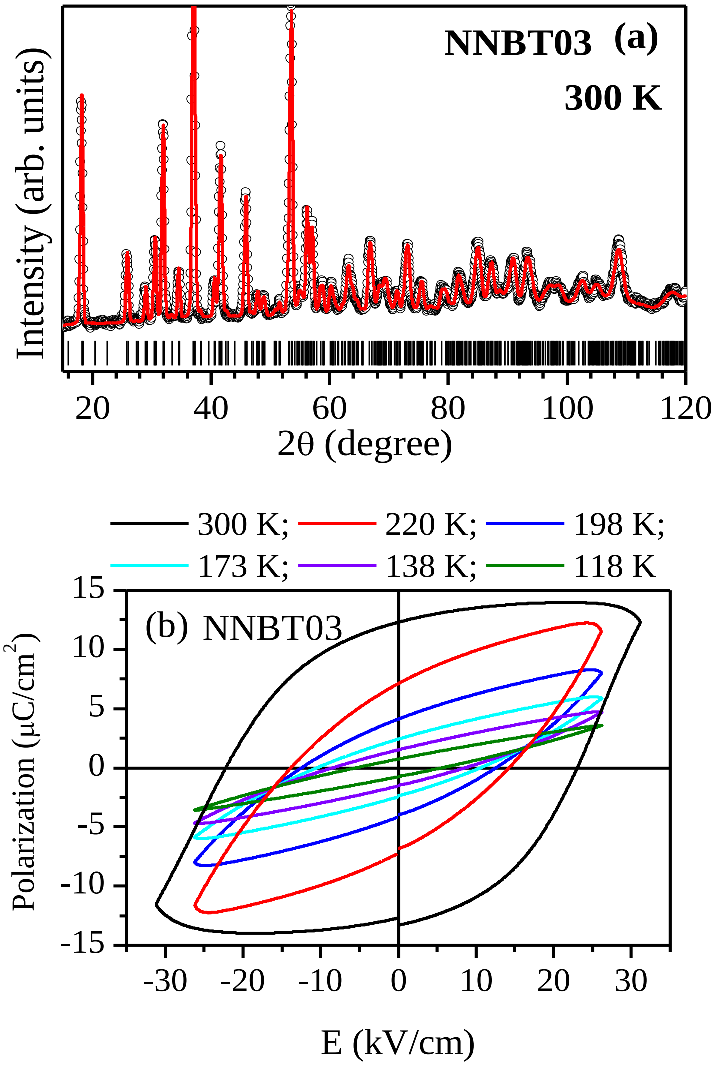

Figure 4.4 (a) Observed (dot), and calculated (continuous line) profiles obtained after the Rietveld refinement using orthorhombic (**Pmc2₁**) for x=0.03. (b) Polarization vs. Electric Field (P-E) curve for NNBT03 at selected low temperatures.

Thus, we refined powder neutron diffraction data at 6 K using rhombohedral **R3c** phase (see inset in Figure **4.5**). The unsatisfactory quality of the Rietveld fit of the diffraction data suggests that the possibility of rhombohedral phase is not favoured in this compound. We tried to refine the powder neutron diffraction data using different crystal structure of classical perovskite ($PbTiO_3$ and $BaTiO_3$) present at different condition but none of these space groups accounted for the Braggs peaks marked with arrow and account the splitting in peaks appeared 32.2°. We have further explored various possibilities as in our X-ray diffraction study and we found that monoclinic phase with space group **Cc** accounted nearly all the reflections at lowest temperature. In the space group **Cc**, for the description of the crystal structure, we used the following monoclinic axes: $a_m= a_p+b_p+2c_p$; $b_m= a_p-b_p$ and $c_m= a_p+b_p$. The monoclinic unit cell contains 4 formula units. The asymmetric unit of the structure consists of Na/Ba atom at the 4a site at (0±u, ¾ ±v, and 0±w), Nb/Ti atom at the 4a site at (¼±u, ¼±v, ¼±w). Three oxygen atoms occupies at the 4a site at (0±u, ¼±v, 0±w); (¼±u, ½ ±v, 0±w) and (¼±u, 0±v, ½±w), respectively. The fit between the observed and calculated profiles is quite satisfactory and include the weak superlattice reflections. However, we find some discrepancy in intensity (see inset Figure **4.5**). A two-phase refinement with both the orthorhombic and monoclinic space groups is found to be acceptable, and all the observed diffraction peaks could be indexed. We find that the orthorhombic and monoclinic phases coexist over a large temperature range from 150 to 6 K in cooling cycle and from 6 to 240 K in heating cycle. The percentage of the orthorhombic phase continuously decreases with lowering temperature and reaches 26 % at 6 K for x=0.03 and becomes zero for x=0.05. The coexistence of both the phases indicates that the structural phase transition from orthorhombic to monoclinic phase is of first order for both compounds. The structural parameters calculated through Rietveld refinement are given in Table **4.2**.

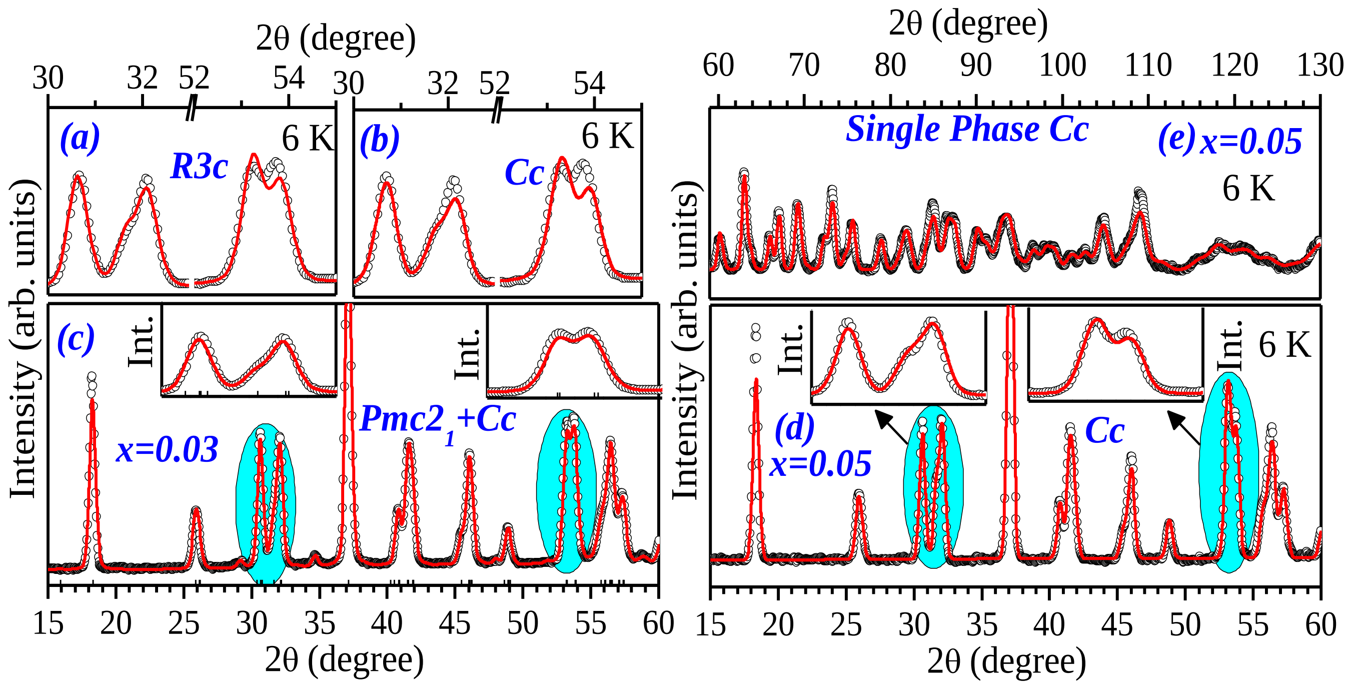

Figure 4.5 Observed (dot) and calculated (continuous line) profiles obtained after the Rietveld refinement using (a) rhombohedral (**R3c**), (b) monoclinic (**Cc**), (c) using both orthorhombic (**Pmc2₁**) and monoclinic phases (**Cc**) for x=0.03, and (d and e) single phase monoclinic phase (**Cc**) for x=0.05 at 6 K. The insets of (c and d) show quality of fitting in highlighted regions using phase coexistence for x=0.03 and single phase for x=0.05 respectively. In all the refinements, the data over full angular range has been used, although in the figures only a limited range is shown to highlight the changes clearly.

Table 4.1 Structural parameters of NNBTx with x=0.03 obtained by Rietveld refinement of powder neutron diffraction data at 6 K using two phase model monoclinic phase (space group: **Cc**) and orthorhombic phase (space group: **Pmc2$_1$**).

Atom		**Composition x=0.03 at T= 300 K**				**Composition x=0.05 at T= 300 K**			
	Site	**Positional Coordinates**				**Positional Coordinates**			
		x	**y**	**z**	**B (Å^2)**	**x**	**y**	**z**	**B (Å^2)**
Na1/Ba1	2a	0.000	0.2523(3)	0.2414(1)	0.30(2)	0.000	0.2649(2)	0.2991(2)	0.25(2)
Na2/Ba2	2b	0.500	0.7690(3)	0.7632(1)	0.90(2)	0.500	0.7725(2)	0.8013(2)	0.55(3)
Nb/ Ti	4c	0.7484(4)	0.7463(1)	0.2427(3)	0.12(6)	0.7497(5)	0.7504(1)	0.3261(2)	0.21(3)
O1	2a	0.00	0.1978(3)	0.7206(5)	0.64(4)	0.00	0.1947(5)	0.800(1)	0.84(3)
O2	2b	0.500	0.7013(3)	0.2051(4)	0.62(1)	0.500	0.7088(4)	0.2919(6)	1.39(1)
O3	4c	0.2231(9)	0.4576(3)	0.4355(3)	0.63(3)	0.2308(7)	0.4637(3)	0.5112(3)	0.54(8)
O4	4c	0.2744(1)	0.0250(1)	-0.008(2)	0.60(9)	0.2780(4)	0.0310(1)	0.0759(2)	0.80(4)
		a_o= 7.7797(4) (Å); b_o= 5.5159 (3) (Å); c_o= 5.5618(2) (Å),				a_o= 7.8031(2) (Å); b_o= 5.5259 (2) (Å); c_o= 5.5646 (2) (Å),			
		unit cell volume=238.66(2) (Å^3)				unit cell volume= 239.94(1) (Å^3)			
		R_p= 2.79; R_{wp}= 3.82; R_{exp}=3.40; χ^2= 1.26				R_p= 3.24; R_{wp}= 4.38 R_{exp}=3.12; χ^2= 1.97			

Table 4.2 Structural parameters of NNBTx with x=0.03 obtained by Rietveld refinement of powder neutron diffraction data at 6 K using two phase model monoclinic phase (space group **Cc**) and orthorhombic (space group: **Pmc2$_1$**).

Atom	**Composition x=0.03 at T= 6 K Space group Cc (phase fraction 74%)**					**Composition x=0.03 at T= 6 K Space group Pmc2$_1$ (phase fraction 26 %)**				
	Site	**Positional Coordinates**				**Site**	**Positional Coordinates**			
		x	**y**	**z**	**B (Å^2)**		**x**	**y**	**z**	**B (Å^2)**
Na1/Ba1	4a	0.000	0.7500	0.0000	0.07(3)	2a	0.000	0.240(1)	0.269(3)	0.03(3)
Na2/Ba2						2b	0.500	0.7684(4)	0.7854(2)	0.04(1)
Nb/Ti	4a	0.2640(1)	0.2506(3)	0.2699(2)	0.04(5)	4c	0.7506(7)	0.7533(5)	0.2477(3)	0.04(2)
O1	4a	0.0265(3)	0.3036(3)	0.0675(3)	0.18(6)	2a	0.0000	0.216(3)	0.7304(6)	0.50(2)
O2	4a	0.3102(2)	0.4664(4)	0.0600(2)	0.02(2)	2b	0.5000	0.260(3)	0.3213(6)	0.26(4)
O3	4a	0.2472(3)	0.0302(3)	0.5698(6)	0.06(3)	4c	0.225(3)	0.494(4)	0.109(6)	0.38(3)
O4						4c	0.287(1)	0.0152(3)	0.000(3)	0.08(2)
	a_m= 9.5054(4) (Å); b_m= 5.5012 (2) (Å); c_m= 5.5512 (2) (Å),					a_o= 7.7681(1) (Å); b_o= 5.5191 (2) (Å); c_o= 5.5571 (1) (Å),				
	β= 124.63 (1) (degree); unit cell volume= 238.94 (2) (Å^3)					unit cell volume= 238.25 (5) (Å^3)				
	R_p= 2.78; R_{wp}= 3.73; R_{exp}=3.39; χ^2= 1.21									

The observed coexisting phases and anomalous smearing of the dielectric response is akin to dipolar glasses and relaxor ferroelectrics. The observed monoclinic phase (**Cc**) is found to be identical to PZT where piezoresponse is ultra large. This monoclinic phase is believed to provide for a flexible polarization rotation and considered to be directly linked to the high performance piezoelectricity in materials due to presence of more easy axis for spontaneous polarizations.

4.4 Variation of structural parameters with temperature

The variation of lattice parameters obtained from the Rietveld refinements for composition x=0.03 and 0.05 with temperature are plotted in Figure **4.6** and Figure **4.7**. It is evident from the figure that for composition x=0.03, in the cooling cycle, the a_o and c_o lattice parameters of the orthorhombic phase decrease and show an anomaly around 120 K. In the heating cycle, the lattice parameters for both phases (orthorhombic and monoclinic) increase and show an anomaly around 250 K. These are the temperature, where we see an anomaly in dielectric studies of the compound. These small anomalous jumps of less than about 0.05 % in lattice constants may reflect release of some strain in the sample that builds up during the process of the phase transition. A small hysteresis in the lattice constants of the same order of 0.05 % also indicates that the relaxation process is much slower than the time scale of several hours in the experiment. It is also important to notice that the monoclinic phase has a higher volume compared with the orthorhombic phase. However, for the composition x=0.05, the lattice parameters decrease on decreasing temperature and increases on increasing temperature. The variation of phase fraction with temperature suggests that the monoclinic phase is dominant below 75 K for both the compounds. It is also clear that the composition x=0.05 completely transforms into monoclinic phase and becomes single phase below 50 K. On the other hand, the composition x=0.03 does not completely transform into monoclinic phase even at the lowest temperature (6 K).

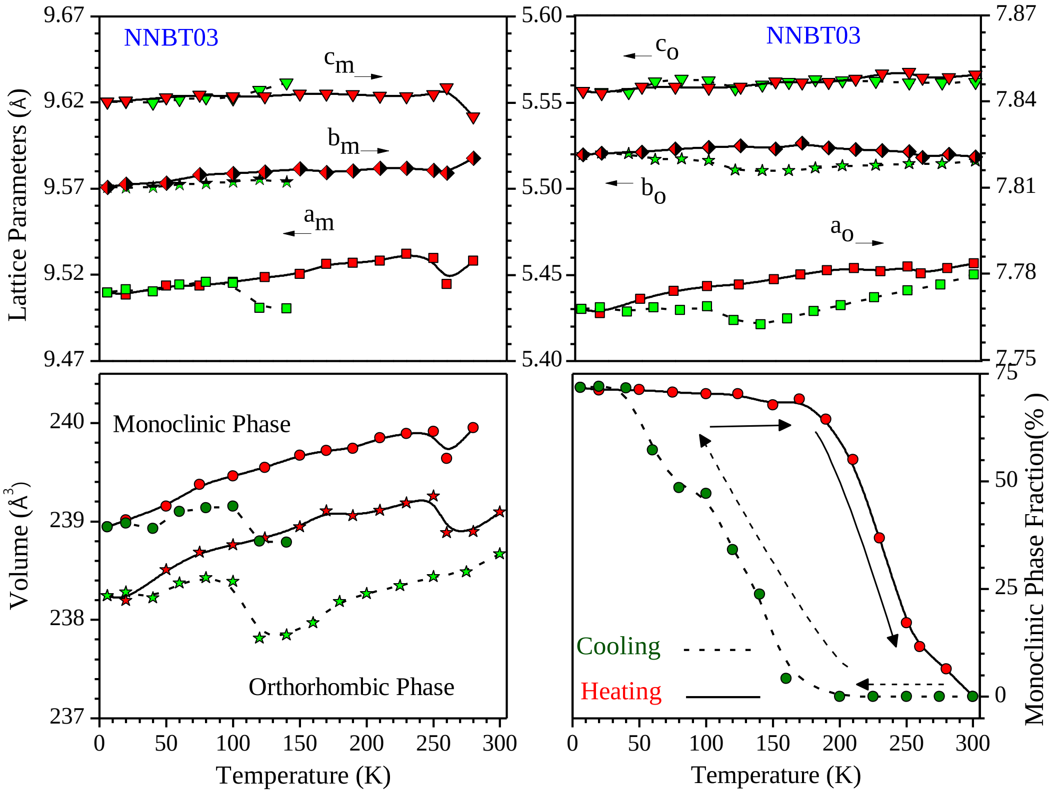

Figure 4.6 Evolution of structural parameters obtained after Rietveld analysis of powder neutron diffraction data of the composition NNBT03 with temperature. Solid and dash lines correspond to heating and cooling cycles respectively.

The thermal hysteresis for composition x=0.03 is larger than that of x=0.05. This suggests that addition of increasing amounts of $BaTiO_3$ in $NaNbO_3$ suppresses the thermal hysteresis.The structural phase transition temperature from orthorhombic to monoclinic phase decreases on increasing concentration of BaTiO3. Variation of lattice parameter for the orthorhombic phase for composition x=0.03 also exhibits a thermal hysteresis which can be signature for ferroelastic type phase transition[41-43]. It is well documented in literature that strain plays a major role in structural phase transition in perovskite structure and which is responsible for ferroelastic phase transition[41-43]. In the present case, the composition x=0.03 exhibits phase coexistence and the low-temperature monoclinic phase has a higher volume compared to the high-temperature orthorhombic phase. Hence as the monoclinic phase grows, it creates strain in the system.

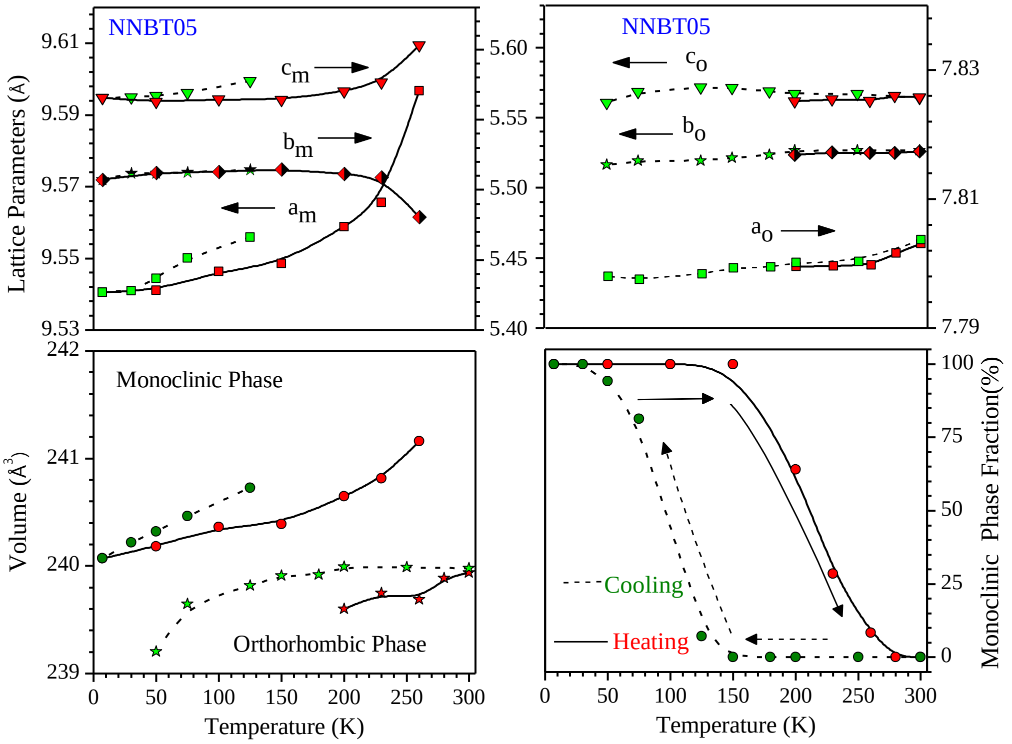

Figure 4.7 Evolution of structural parameters obtained after Rietveld analysis of powder neutron diffraction data of the composition NNBT05 with temperature. Solid and dash lines correspond to heating and cooling cycles respectively.

4.5 Conclusion

In conclusion[4], we have carried out systematic temperature-dependent neutron diffraction measurements in conjunction with dielectric spectroscopy from 6 to 300 K. The temperature dependent dielectric constant measurements show dispersion with frequency and exhibit anomalies at different temperatures in cooling and heating cycles. To explore structural change as a function of temperature, we analyzed the powder neutron diffraction data collected in the same temperature range. The disappearance of certain superlattice reflections and appearance of splitting in main cubic perovskite peaks at low temperatures provide a signature of structural phase transition. Detailed Rietveld analysis of powder neutron diffraction data reveals that the ferroelectric orthorhombic and rhombohedral structural models are unsatisfactory. We have explored various possibilities and found that the monoclinic phase with space group **Cc** accounted nearly all the reflections at lowest temperature. This monoclinic phase is believed to provide for a flexible polarization rotation and considered to be directly linked to the high performance piezoelectricity in materials. The coexistence of both the phases indicates that the structural phase transition from orthorhombic to monoclinic phase is of first order. The coexisting phases and reported anomalous smearing of the dielectric response are akin to dipolar glasses and relaxor ferroelectrics.

Chapter 5: Probing of Phonon Anomalies in Modified Sodium Niobate: A Raman Scattering Study

This chapter is based on our published article J. Raman Spectrosc. 2019, 50, 1177. It contains the results obtained from Raman spectroscopic study as a function of composition in modified sodium niobate [(1-x)$NaNbO_3$-x$BaTiO_3$:NNBTx] for x=0.0 to 0.15 at room temperature.

For a proper understanding of the properties of the materials, the structural information obtained from diffraction techniques should be supplemented and supported by other techniques. The structural phase transitions in these compounds are governed by the softening of various phonon modes, which can be probed via various experimental methods including Raman spectroscopy, infrared spectroscopy, and inelastic neutron scattering. Raman spectroscopy is sensitive to local structure changes and is a suitable tool to investigate the phase transitions in these materials[84-92]. With this aim in mind, we performed Raman spectroscopy measurements to provide a deep insight into the structural phase transitions and the role of phonons on changing the composition.

5.1 Group-Theoretical Analysis for Raman Active Modes

As described in Chapter 3, we studied dielectric and structural properties of NNBTx using a combination of impedance spectroscopy and X-ray diffraction techniques [93]. Based on the appearance and/or disappearance of the superlattice reflections in the X-ray diffraction data, we observed that on increasing concentration of $BaTiO_3$ in $NaNbO_3$ matrix, there are drastic changes in the intensities of main perovskite peaks and superlattice reflections on increasing the dopant concentration (see Figure 3.1). The X-ray diffraction patterns for upto $x<0.02$ could be indexed using the **AFE** (**Pbcm**) phase. On increasing the concentration $x \geq 0.02$, we found that the superlattice reflection around 36.2˚ could not be indexed using the same **AFE** phase model and crystal structure transforms from the antiferroelectric orthorhombic **AFE** (**Pbcm**) phase to the ferroelectric orthorhombic **FE1** (**Pmc2$_1$**) phase. Further, increase in the dopant concentration leads to suppression of another superlattice reflection S2 at 2θ~ 38.5˚ and diffraction pattern could be indexed [93] using ferroelectric orthorhombic **FE2** (**Amm2**) phase for x≥0.10.The peaks marked with an asterisk correspond to $Ba_3Nb_4Ti_4O_{21}$ and the results of the two phase refinement suggest that the content of the undesired $Ba_3Nb_4Ti_4O_{21}$ phase is about ~1% and it increases upto 3% on increasing $BaTiO_3$ content to x=0.20.

Details of the normal mode analysis performed using free access site Bilbao Crystallographic Server [94] for these three phases are given below:

1) **Orthorhombic AFE (for composition 0≤x<0.03):** At ambient condition, pure $NaNbO_3$ has **AFE** orthorhombic (**Pbcm**) symmetry with unit cell dimensions $\sqrt{2}a_P \times \sqrt{2}a_P \times 4a_P$ (with respect to cubic perovskite with lattice parameter a_P). It has eight numbers of formula units (total 40 atoms) and total 120 possible normal modes. The asymmetric unit contains two types of sodium atoms (Na), one type of niobium atom (Nb) and four types of oxygen atoms. Table 5.1 contains the details of the group-theoretical analysis for the **AFE** orthorhombic phase.
2) **Orthorhombic FE1(for composition 0.02<x<0.07):**The structure of the NNBTx (x=0.02 <x< 0.07) at room temperature was found to be orthorhombic (**Pmc2$_1$**) symmetry with unit cell dimensions $2a_P \times \sqrt{2}a_P \times \sqrt{2}a_P$ and four numbers of formula units, i.e. total 20 atoms. There should be a total 60 possible normal modes. The group-theoretical analysis gives 57 Raman active modes represented by $\Gamma_{Raman}=16A_1+13A_2+12B1+16B_2$.These Raman active modes are simultaneously IR active due to non-centrosymmetry of the crystal structure

except A_2 mode. Table 5.2 contains the details of the group-theoretical analysis for the **FE1** orthorhombic phase.

3) **Orthorhombic FE2 (for composition $0.10 \leq x \leq 0.15$):** The structure of the NNBT10 at room temperature was found to be orthorhombic (**Amm2**) symmetry with cell dimensions $a_P \times 2a_P \times 2a_P$ and four numbers of formula units, i.e., total 20 atoms. In the primitive unit cell, there are 10 atoms. There should be total 30 possible normal modes. The group-theoretical analysis gives 27 Raman active modes represented by $\Gamma_{Raman}=9A_1+2A_2+7B_1+9B_2$. Table 5.2 contains the details of the group-theoretical analysis for the **FE2** orthorhombic phase.

Table 5.1 Atomic site symmetries and normal mode analysis performed for the pure $NaNbO_3$.

Atoms	Wyckoff Site	Position	Site sym.	Irreducible Representations
(Na/Ba)1	4c	(¼+u, ¾,0)	C_2^x	$A_g+A_u+2B_{1g}+2B_{1u}+2B_{2g}+2B_{2u}+B_{3g}+B_{3u}$
(Na/Ba)2	4d	(¼+u, ¾+v, ¼)	C_s^{xy}	$2A_g+A_u+2B_{1g}+B_{1u}+B_{2g}+2B_{2u}+B_{3g}+2B_{3u}$
Nb/Ti	8e	(¼+u,¼+v,⅛+w)	C_1	$3A_g+3A_u+3B_{1g}+3B_{1u}+3B_{2g}+3B_{2u}+3B_{3g}+3B_{3u}$
O1	4c	(¼+u, ¼, 0)	C_2^x	$A_g+A_u+2B_{1g}+2B_{1u}+2B_{2g}+2B_{2u}+B_{3g}+B_{3u}$
O2	4d	(¼+u, ¼+v, ¼)	C_s^{xy}	$2A_g+A_u+2B_{1g}+B_{1u}+B_{2g}+2B_{2u}+B_{3g}+2B_{3u}$
O3	8e	(½+u,0+v,⅛+w)	C_1	$3A_g+3A_u+3B_{1g}+3B_{1u}+3B_{2g}+3B_{2u}+3B_{3g}+3B_{3u}$
O4	8e	(0+u,½+v,⅛+w)	C_1	$3A_g+3A_u+3B_{1g}+3B_{1u}+3B_{2g}+3B_{2u}+3B_{3g}+3B_{3u}$

$\Gamma_{Total}= 15A_g+13A_u+17B_{1g}+15B_{1u}+15B_{2g}+17B_{2u}+13B_{3g}+15B_{3u}$
$\Gamma_{Acoustic}= B_{1u}+B_{2u}+B_{3u}$
$\Gamma_{Optical}= 15A_g+13A_u+17B_{1g}+14B_{1u}+15B_{2g}+16B_{2u}+13B_{3g}+14B_{3u}$
$\Gamma_{IR}= 14B_{1u}+16B_{2u}+14B_{3u}$
$\Gamma_{Silent}= 13A_u$
$\Gamma_{Raman}= 15A_g+17B_{1g}+15B_{2g}+13B_{3g}$

Table 5.2 Atomic site symmetries and normal mode analysis performed for the NNBTx (x=0.02 < x< 0.07).

Atoms	Wyckoff Site	Position	Site sym.	Irreducible Representations
(Na/Ba)1	2a	(0, ¼, ¾+w)	C_s^{yz}	$2A_1+A_2+B_1+2B_2$
(Na/Ba)2	2b	(½, ¼, ¾+w)	C_s^{yz}	$2A_1+A_2+B_1+2B_2$
Nb/Ti	4c	(¾+u, ¾+v, ¾+w)	C_1	$3A_1+3A_2+3B_1+3B_2$
O1	2a	(0, ¼+v, ¼+w)	C_s^{yz}	$2A_1+A_2+B_1+2B_2$
O2	2b	(½, ¼+v, ¼+w)	C_s^{yz}	$2A_1+A_2+B_1+2B_2$
O3	4c	(¼+u, ½+v, ⅛+w)	C_1	$3A_1+3A_2+3B_1+3B_2$
O4	4c	(¼+u, 0+v, ½+w)	C_1	$3A_1+3A_2+3B_1+3B_2$

$\Gamma_{\text{Total}}= 17A_1+ 13A_2+ 13B_1+ 17B_2$
$\Gamma_{\text{Acoustic}}= A_1+B_1+B_2$
$\Gamma_{\text{Optical}}= 16A_1+ 13A_2+ 12B_1+ 16B_2$
$\Gamma_{\text{IR}}= 16A_1+ 12B_1+ 16B_2$
$\Gamma_{\text{Raman}}= 16A_1+ 13A_2+ 12B_1+ 16B_2$

Table 5.3 Atomic site symmetries and normal mode analysis performed for the NNBTx (x=0.10-0.15).

Atoms	Wyckoff Site	Position	Site sym.	Irreducible Representations
Na/Ba	4d	(0, ¾+v, 0+w)	C_s^{yz}	$2A_1+A_2+B_1+2B_2$
(Nb/Ti)1	2b	(½, 0, ¼+w)	C_{2v}	$A_1+ B_1+B_2$
(Nb/Ti)2	2b	(½,½, ¼+w)	C_{2v}	$A_1+ B_1+B_2$
O1	2a	(0, 0, ¼+w)	C_{2v}	$A_1+ B_1+B_2$
O2	2a	(0, ½, ¼+w)	C_{2v}	$A_1+ B_1+B_2$
O3	4e	(½, ¾+v, ¼+w)	C_s^{yz}	$2A_1+A_2+B_1+2B_2$
O4	2b	(½, 0, 0+w)	C_{2v}	$A_1+ B_1+B_2$
O5	2b	(½,½, 0+w)	C_{2v}	$A_1+ B_1+B_2$

$\Gamma_{\text{Total}}= 10A_1+2A_2+8B_1+10B_2$
$\Gamma_{\text{Acoustic}}= A_1+ B_1+B_2$
$\Gamma_{\text{Optical}}= 9A_1+2A_2+7B_1+9B_2$
$\Gamma_{\text{IR}}= 9A_1+7B_1+9B_2$
$\Gamma_{\text{Raman}}= 9A_1+2A_2+7B_1+9B_2$

5.2 Evolution of Raman Spectra of NNBTx (0.0 ≤ x ≤ 0.20)

$NaNbO_3$ belongs to the ABO_3 type perovskite family and at the highest temperature it has a paraelectric cubic phase. This cubic phase unit cell contains six oxygen atoms, which reside at the face centred positions and form oxygen octahedron. Inside the void of the octahedron, there is a metal cation B (in present case Nb^{5+}). Eight A type (Na^+) cations occupy the corners of the unit cell. This cubic ($\mathbf{Pm\overline{3}m}$) phase is characterized by second order Raman scattering. At lower temperatures, the structure gets slightly distorted and the effect of these distortions changes the symmetry and number of formula units in unit cell of daughter phase. As a result, appearance or disappearance of Raman modes in the Raman spectra are observed and can be treated as a signature for structural phase transitions. We observed a clear appearance and disappearance of first-order Raman modes in the Raman spectra of NNBTx as a function of composition and details are discussed below.

Figure 5.1 shows the evolution of Raman spectra collected at ambient conditions as a function of composition in the range 10 to 1000 cm^{-1}. Raman spectrum of $NaNbO_3$ is similar as reported by various authors[85-87, 95-98]. The spectra could be decomposed into two main regions involve vibrations of the Na^+ against the NbO_6 octahedra and the isolated vibrations of NbO_6 octahedra, namely, the external and internal modes. Under the consideration of external modes, the vibrational bands below 100 $cm^{-1}$are the translational modes (**Tr**), which belong to the motion of the Na^+ ions against the NbO_6 octahedra. The bands at 93.4, 123.6, 143.2 and 155.3 cm^{-1} are the librational modes (**L**) of NbO_6 octahedra. These are the roto-vibrational modes of the NbO_6 octahedra. The internal modes appear at relatively higher wavenumbers and these comprise the bending of bond angles (O-Nb-O) and the stretching motion of the bonds (Nb-O) within the octahedron. Following the literature for the NbO_6 octahedron in the perovskite lattice structures [99], the vibrations of isolated equilateral octahedron consist of $A_{1g}(\nu_1)+E_g(\nu_2)+2F_{1u}(\nu_3, \nu_4)+F_{2g}(\nu_5)+F_{2u}(\nu_6)$ normal modes.

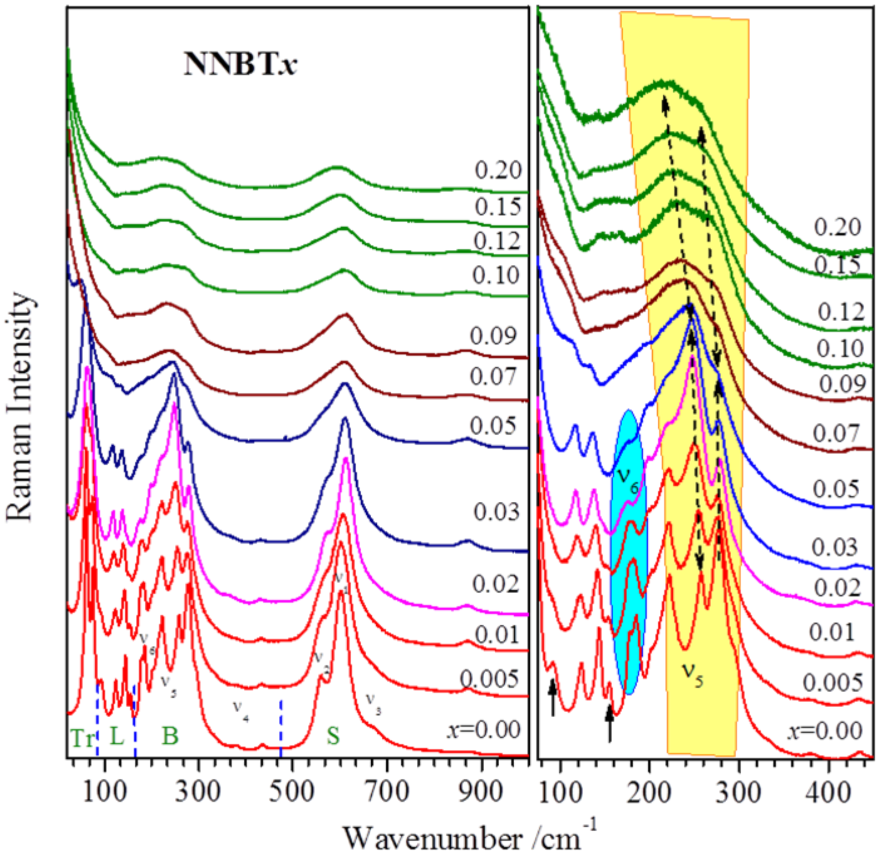

Figure 5.1 (Left panel) Evolution of the Raman spectra collected in ambient conditions for various compositions of NNBTx (x=0.0 to 0.20). The zoom view of the spectra up to 450 cm^{-1} is shown in the right panel. For clarity, the intensity of each spectrum in the right panel is normalized to unity from 75 to 450 cm^{-1}. The Raman spectra may be grouped as translational (Tr), librational (L), bending (B) and stretching (S) modes. The region that shows maximum change in Raman spectra is highlighted by yellow and blue colours. The librational modes around wavenumber 93.4 and 155.3 cm^{-1} are marked with arrows.

The ν_1, ν_2, and ν_3 modes belong to the stretching motion and ν_4, ν_5, and ν_6 are the bending modes of a perfect octahedron[86, 96]. Out of these six modes only ν_1, ν_2, and ν_5 are Raman active and ν_3, ν_4 are IR active. The triply-degenerate mode ν_6 is a silent mode. However, depending on the site symmetry these modes get split and non-Raman active modes may become Raman active. For the spectrum of pure $NaNbO_3$, the bands located in the range 160 to 190, 190 to 300, 370 to 440 and around 560, 600, 670 cm^{-1} are assigned in literature as υ_6, υ_5, υ_4 [bending modes (**B**)] and ν_2, ν_1, and ν_3 [stretching modes (**S**)] respectively. Further, on increasing the dopant concentration, the entire Raman spectrum shifts towards the lower wavenumber side and dramatic changes are seen in the relative intensities of the librational and bending modes of the Raman profiles (shown in right-hand side zoomed part of Figure 5.1). The Raman spectra for the composition $x<0.05$ looks similar because both **AFE** (**Pbcm**) and **FE1** (**Pmc2_1**) phases have a similar number of Raman active modes (60 and 57 Raman active mode). However, for the composition $x\geq0.5$, the spectrum becomes diffusive as a result of doping and may be associated with the increase of disorder in the crystal.

5.3 Fitting of Raman Bands:

As said earlier, NNBTx undergoes structural phase transitions around $x>0.02$ and 0.10. Therefore, we have taken $x=0.0$, 0.03 and 0.10 as a representative of these three phases namely: **AFE, FE1,** and **FE2** phases, respectively. To quantify the Raman mode intensities and peak positions, we have fitted the whole Raman spectra using damped harmonic oscillator (DHO) model (see Equation 2.10).

Figure 5.2 (a) shows the fitting of the Raman spectra obtained for $NaNbO_3$ at ambient conditions. A total 22 peaks were used to get good fitting of the observed data. However, we estimated total 60 Raman active modes using group-theoretical calculations. The fitted Raman bands showed good agreement with the previous reports on pure bulk sodium niobate.

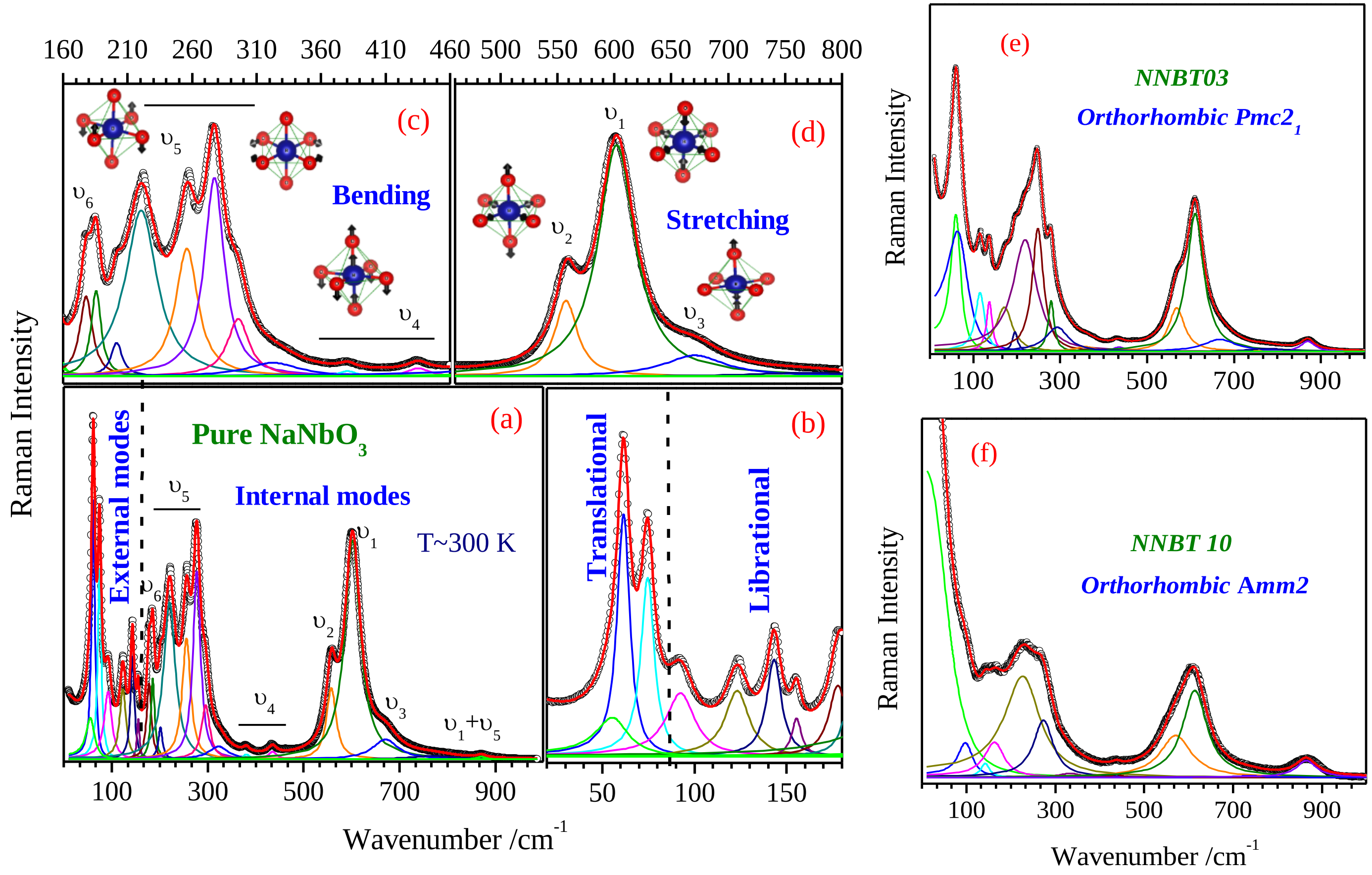

Figure 5.2 Fitting of Raman spectroscopy data of pure (a) NaNbO$_3$, (e) NNBT03 and (f) NNBT10. Open circles (black) and solid line (red) represent the observed and fitted profile of Raman spectra. (b), (c), and (d) show the expanded view of fitted Raman spectra of NaNbO$_3$ in different region.

Figure 5.2 (b), (c) and (d) are close views of the translational (**Tr**), librational (**L**), bending (**B**) and stretching (**S**) modes of the same profile. Figure 5.2 (e) and (f) show the fitting of the observed Raman data of these compositions, respectively.

Normal mode analysis suggests 57 Raman active modes for the FE1 ($Pmc2_1$) phase, but 17 peaks gave a good fitting of the Raman spectra observed for NNBT03. The Raman spectrum looks similar as reported by Sheratori *et al.*[96] For FE2 (Amm2) phase, factor group analysis suggested a total of 27 Raman active modes, but only 12 peaks were sufficient for fitting of the observed broad Raman spectra of NNBT10. The number of calculated and fitted Raman modes may be different due to less resolved and broad features of the observed spectra. Similar broadening in the Raman spectra was also observed in PMN-PT solid solution and explained in terms of coexistence of polar nano-regions and chemically ordered clusters[92]. They show that presence of the polar nano-regions (PNR) is due to the ions at the B site: Nb, Mg and Ti being displaced from their high symmetry positions, give rise to formation of local electric dipoles. The presence of chemically ordered clusters additionally complicates an understanding of the Raman spectra. As the Raman cross-section depends mainly on the bond polarizabilities, i.e., the number of electrons involved in the bond, it is highly possible that the Raman spectra will not reflect the signature of all regions. In the case of PMN-PT, the following sequence of the Raman mode intensities is expected: Nb-O > Ti-O >> Mg-O. As a consequence, the contribution of Mg-rich regions is too weak to be observed, as far as the bending and stretching modes are considered. Consequently, the unambiguous Raman mode assignment is rather delicate.

Positions of the peaks for NNBTx (x=0.0, 0.03 and 0.10) are compared with the previously reported values for bulk sodium niobate given in Table 5.4. The Raman profiles of the samples with x= 0.02, 0.07 and 0.09 indicate some minor features which suggest mix phases that are consistent with the X-ray diffraction results discussed below. We have analysed all the spectra and the variation of the peak positions as obtained through the fittings is shown in Figure 5.3.

Table 5.4 Comparison of the Raman band positions (cm^{-1}) observed in the present study for NNBTx with the reported data of the $NaNbO_3$ in previous studies. The assignment of the modes has been made following the literature for vibrations of isolated equilateral NbO_6 octahedra in the perovskite lattice structures[85, 99].

$NaNbO_3$[86] AFE (Pbcm) Phase	$Li_{0.12}Na_{0.88}NbO_3$[100] FE ($Pmc2_1$) Phase	Present Study			
		$NaNbO_3$	NNBT03	NNBT10	Assignment
		57.4			Na^+
60.2		61.9	62.6	68.8	
73.0	81	74.9	74.4	----	
89.5		93.4	----	----	NbO_6^- libration
115.1		----	----	----	
121.0	120.1	123.6	116.5	101.5	
136.9		----	137.2	----	
142.1		143.3	----	143.1	
	149.1				
153.4		155.5	----		
175.1		177.9	173.7	166.8	$\upsilon_6\ (F_{2u})$
183.2		185.7	----	----	
	194				
201.0		201.6	195.9	----	$\upsilon_5\ (F_{2g})$
218.8	226	220.4	222.8	211.4	
247.6		256.2	249.4	234.4	
255.1	254	277.5	279.2	275.2	
276.1	285.4	296.0	308.8	----	
295.9		324.0	----	----	
378.5		380.7	359.3	335.3	$\upsilon_4\ (F_{1u})$
435.3	436.7	435.4	435.8	437.9	
557.2	564.9	557.8	568.6	572.9	$\upsilon_2\ (E_g)$
602.6	618.4	602.4	611. 2	615.0	$\upsilon_1\ (A_{1g})$
671.5		671.6	669.2	737.0	$\upsilon_3\ (F_{1u})$
		769.6	780.5		
867.3	873	870.8	869. 9	865.2	$\upsilon_5 + \upsilon_1$

5.4 Discussion:

In pure $NaNbO_3$, the two main peaks due to translation of Na^+ ion against the NbO_6^- octahedra clearly indicate that there are two types of interactions between these ions due to two distinct types of Na^+ ions (sitting at different sites). The separation between these two peaks decreases and both shift towards lower wavenumber side continuously on increasing the doping concentration. The broadening and merging of these peaks could be related to the presence of more types of interactions in the crystal due to the incorporation of different types of ions (Na^+ and Ba^{+2}) with different sizes. Also, the different types of atoms will show different types of bonding with oxygen atoms. The overall translational modes get broadened beyond our detection range on increase of dopant concentration x>0.05.

The most prominent changes could be seen in the librational modes around wavenumber 93.4 cm^{-1} and 155.5 cm^{-1} (Figure 5.1). These modes disappear at x~0.03, and all the librational modes get broadened at a higher concentration of dopant for x>0.05. In a previous phonon dynamics study on $NaNbO_3$, Mishra *et al.*[38] proposed that the Raman modes at around 93 $cm^{-1}$and 123 cm^{-1} belong to A_{1g} modes and they appear due to folding of the corresponding specific zone centre points[38]. They identified that the mode at 93 cm^{-1} appears due to folding of T point in the Brillouin zone of the cubic phase and involves significant motion of Na, Nb, and O atoms located at 4d (¼+u, ¾+v, ¼), 8e (¼+u, ¼+v, ⅛+w), and (½+u, 0+v, ⅛+w) sites, respectively. This T point mode along with R_{25} and M and Δ point mode instabilities is responsible for antiferroelectricity in $NaNbO_3$. In our investigation we observe that the modes around 93.4,123.6 and 155.5 cm^{-1} disappear when the structure transforms from orthorhombic **AFE** (**Pbcm**) phase to orthorhombic **FE1** (**Pmc2$_1$**) phase at x~0.03 and can be treated as a signature of the structural phase transition in this compound.

Bending modes ν_6, $\nu_{5,}$ and ν_4 of the NbO_6 octahedra are very much sensitive to the changes in the lattice parameters of the unit cell. We observed that the continuous expansion in the volume of the unit cell leads to an increase in the average Nb-O bond length and corresponding decrease in the force constants. Due to this effect overall bending modes are shifted towards the lower wavenumber side with anomalous broadening with increasing the concentration of $BaTiO_3$ in the $NaNbO_3$ matrix. The bending mode ν6 arises due to the distortion of the perfect oxygen octahedra. In the case of perfect octahedra, we do not get the intensity of the ν_6 mode [86]. The presence of this band near 185 cm^{-1} is clearly visible for pure $NaNbO_3$, which indicates that the NbO_6^- octahedra are slightly distorted. However, the intensity of this band decreases continuously with increased broadening. This could be the result of Ti^{+4} ion substitution with Nb^{+5} and doping of the relatively large ion Ba^{+2} at A site which increases the overall volume of the perovskite cell and making the octahedra less distorted. The internal bending modes υ_5 become broad and converge with the υ_4 at x>0.05. The continuous change in the relative intensities and broadening of these bending modes is observed.

Figure 5.3 shows the variation of the peak positions and damping constant for the NNBTx solid solution ($x=0.0 \leq x \leq 0.15$). Shift in peak position and damping constant of the main bending modes near about 277 and 255 cm^{-1} is remarkable (Figure 5.3 (d) and (e) respectively) and show anomalous variation around x=0.02, which indicates the changes in the microscopic environment of the NbO_6^- octahedra due to the changes in the Nb-O bond lengths with cell expansion. The higher wavenumber modes ν_1, ν_2 and ν_3 (which are due to stretching motion of internal octahedra) get broadened on increasing the dopant concentration. Also, we got only a very feeble signature of ν_3 mode which indicates significant reduction in the distortions of NbO_6 octahedra for x>0.05. Variation of the peak positions and damping constant of stretching modes present around 601 cm^{-1} and 560 cm^{-1} are plotted in Figure 5.3 (b) and (c) respectively.

The peak position shows anomalous behaviour at x>0.02 and 0.10 with a change in slope. All these modes are broad because of the disorder in the system at both A and B sites for higher concentrations.

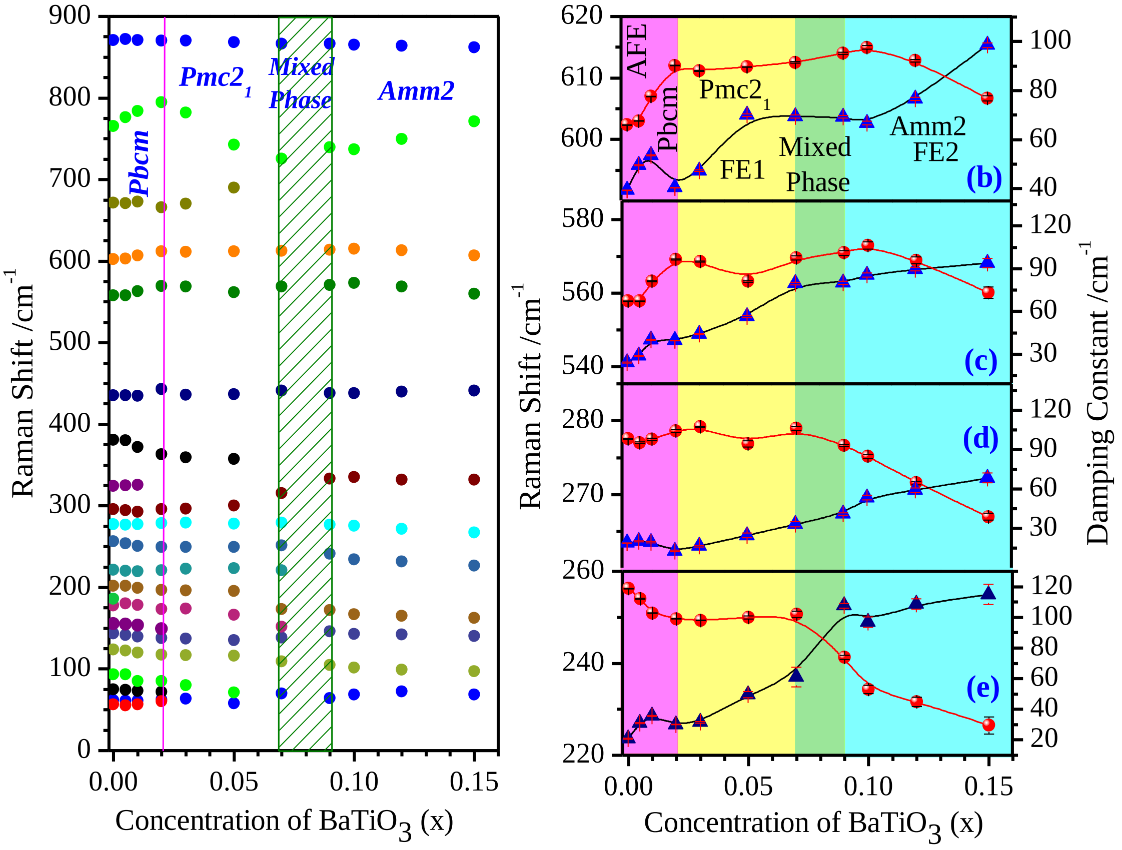

Figure 5.3 (a) Raman shift vs. composition plot for the NNBTx solid solution (x=0.0 to 0.15). Dashed lines show the boundary between the structural phases observed during the indexing of X-ray diffraction patterns. Variation of the peak positions (red circles) and damping constant (blue triangles) of stretching modes present at (b) ~601 cm^{-1}, (c) ~560 cm^{-1}and bending modes at (d) ~277 cm^{-1}, (e) ~255 cm^{-1} are shown in right panel.

To relate the results of Raman spectroscopic measurements with the X-ray diffraction study, we have obtained the structural parameters using Rietveld refinement of the X-ray diffraction data of these compositions as shown in Figure 5.4. We have plotted the cell parameters of these phases in terms of the cell parameters of the equivalent elementary perovskite (i.e., pseudo-cubic unit cell). We notice some phase coexistence for x= 0.02 and in the range $0.07 \leq x \leq 0.10$, which may be due to first-order nature of the phase transitions. In Figure 5.4, we have plotted the structural parameters corresponding to the majority phases only. The variation of pseudo-cubic unit cell parameters clearly shows the monotonic increase in the lattice parameters and volume and jumps at phase transition boundaries (Figure 5.4 (a)).

Figure 5.4 (b) shows the variation of volume of oxygen octahedra in the **AFE** (**Pbcm**) and **FE1** (**Pmc2$_1$**) phase. There is only one type of Nb atom and hence only one type of octahedra. However, in case of **FE2** (**Amm2**), there are two types of Nb atoms. So, we get two types of octahedra present in the structure and all the octahedra dipoles are aligned in the same direction (i.e. Nb displacement is in the same direction). The volume of octahedra shows small change around x~0.02 when structure transforms from **AFE** to **FE1** phase and there is a bifurcation with abrupt change at around x~0.10, which corresponds to **FE2** phase. The axial Nb-O bond lengths of oxygen octahedra first increases slowly up to x~0.07 and then there is a huge jump and bifurcation due to the presence of two types of Nb atoms present in orthorhombic **FE2** (**Amm2**) symmetry (Figure 5.4 (c)). This increase in bond lengths is consistent with the low wavenumber shift of the bending modes obtained in the Raman profile. The plot of variation of axial and planar Nb-O-Nb bond angles with $BaTiO_3$ content (x) (Figure 5.4 (d)) suggests that first, these angles change a little bit during the transition from **AFE** (**Pbcm**) to **FE1** (**Pmc2$_1$**) phase then there is almost linear increment in the axial bond angle and it becomes 180 degrees around x~0.10 which suggest that there is a suppression of one octahedra tilt. The planar Nb-O-Nb bond angle also increases discontinuously at x~0.10, which is related to the decrease in distortion in the NbO_6 octahedra on increasing the $BaTiO_3$ content in the NNBTx solid solution.

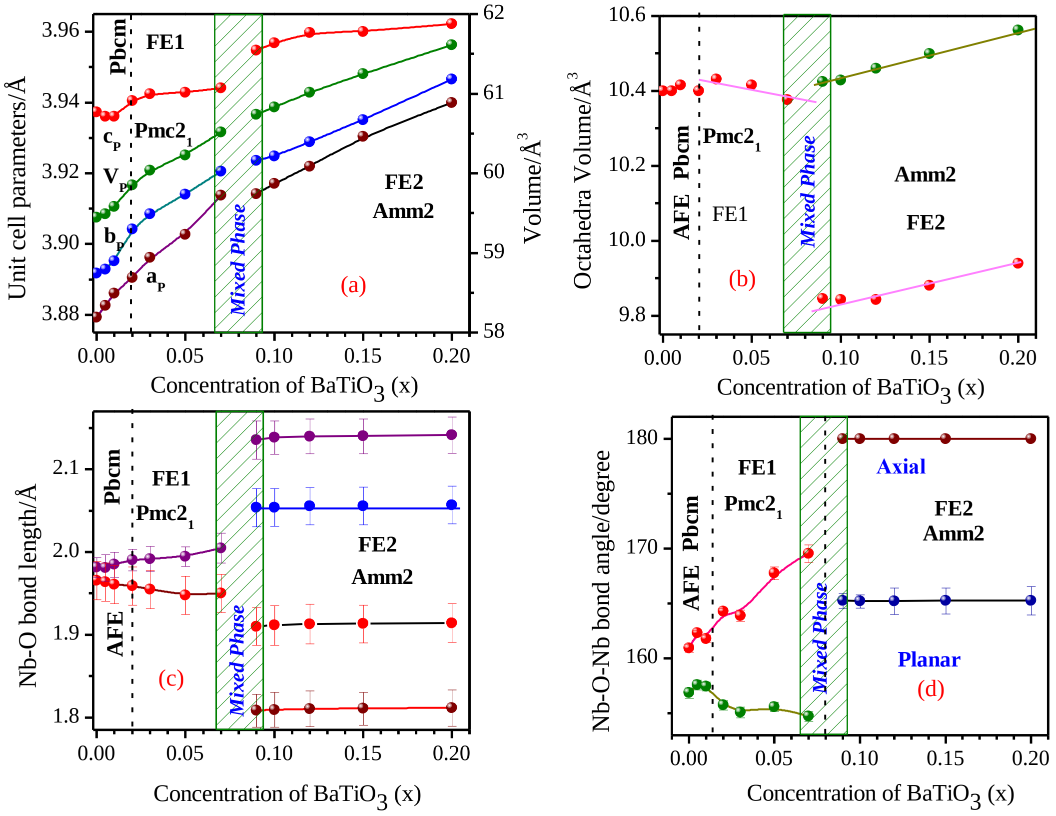

Figure 5.4 (a) Variation of cell parameters of different phases in terms of equivalent elementary perovskite cell parameters (ap, bp, and cp) as a function of composition. The relation between elementary perovskite cell and different orthorhombic phases are as: **AFE** phase (ao= √2 ap, bo=√2 bp and co= 4 cp), **FE1** phase (ao= 2 ap, bo=√2 bp and co= √2 cp) and **FE2** phase (ao= ap, bo=2 bp and co= 2 cp). (b), (c) and (d) show the variation of octahedral volume, axial Nb-O bond lengths and Nb-O-Nb bond angles, respectively.

5.5 Conclusion:

In summary, we observed a distinct change in Raman profile across the composition x= 0.0, 0.03 and 0.10. The characteristic antiferroelectric mode at 93.4, 123.6 along with a mode at 155.5 cm^{-1} present in NaNbO$_3$ in Raman spectra disappears on doping. These suggest the suppression of the antiferroelectric phase and confirm a structural phase transition across x>0.02. Further, on increasing the concentration of dopant above x> 0.05, the Raman spectra become diffusive. We observed a distinct change in terms of redistribution of intensities and positions of Raman lines in bending (in range of 100-300 cm^{-1}) and stretching modes (>550 cm^{-1}). Shifting of Raman spectra towards lower wavenumber and change in the intensities of ν6 mode (which reflects a measure of the distortion in the NbO_6 octahedra) with increment of the dopant could be explained in terms of bond lengths and Nb-O-Nb bond angles. These results from Raman scattering are consistent with previous powder X-ray diffraction studies, which showed drastic changes in the intensities of main perovskite peaks and superlattice reflections on increasing concentration of $BaTiO_3$ in $NaNbO_3$ matrix.

Chapter 6: Probing of Phonon Anomalies in NNBT05 below 300 K: A Raman Scattering Study

This chapter is based on our published article J. Raman Spectrosc. 2019, 50, 1949. It contains the results of the Raman spectroscopic study of the modified sodium niobate NNBT05.

In our previous chapters, we investigated the structural phase transition at low temperature using X-ray and neutron diffraction techniques in conjunction with dielectric measurements for x=0.03 and 0.05. It was observed from the low-temperature diffraction studies that the room-temperature orthorhombic phase with space group **$Pmc2_1$** undergoes a first-order phase transition with large hysteresis and transforms to the monoclinic phase with space group **Cc**. The present chapter contains the evidence of the low-temperature structural phase transition in NNBT05 using Raman spectroscopic study.

The structural phase transitions in the perovskite-type solid solutions involve complex patterns of cationic displacements and octahedra tilts and/or rotations, which are very complex to characterize only by diffraction experiments due to coexistence of different symmetries at short and long scale[101, 102]. The characterization of the complex physical behaviour of these materials require a technique capable of probing the local structure. Raman spectroscopy is one of the important tools which are sensitive to the chemical bonding at local regions in solids. It provides clear evidence of phase transitions at low temperature for disordered substituted perovskites in terms of change in the intensities and positions of the Raman bands[101, 103]. In this regard, various researchers have used Raman spectroscopy to get better information of the structural phase transitions especially in case of morphotropic phase boundary (MPB)[19, 101, 102, 104-107]. Historically, a morphotropic phase boundary (MPB) in (1-x)$PbZrO_3$-x$PbTiO_3$ (PZT) is referred to as the change in the crystal structure of the ferroelectric material from rhombohedral to tetragonal phase on changing its composition or by application of external pressure[44]. It is found that this phase transition in MPB region is mediated by an intermediate phase of monoclinic symmetry. The monoclinic phases are believed to provide easy polarization rotation on application of external electric field and affect the electromechanical properties of these materials**.** The solid solutions of NNBT05 is analogous to solid solutions of PZT, where one end-member is antiferroelectric while the other end-member is ferroelectric in nature and expected to show anomalous behaviour. We observed stabilization of the monoclinic phase (**Cc**) which is identical to PZT where piezoresponse is ultra-large. The aim of the present study is to provide evidence of the low-temperature phase transition in the lead-free piezo-ceramic NNBT05 using Raman spectroscopic technique.

6.1 Evolution of Raman Spectra of NNBT05 at Low temperature

The parent compound $NaNbO_3$ has a cubic perovskite structure at high temperature which has a single ABO_3 formula unit in its primitive cell. In perovskite structure, the A atoms reside at the eight corners of the cubic cell, the B atom resides at the body centred position and the six oxygen atoms occupy face-centred positions. These six oxygen atoms form an octahedron. The Raman modes arise due to the vibrations of these atoms from their mean positions. The Raman modes in specific ranges are denoted by **Tr**, **L**, **B** and **S**, which are referred to as translational, librational, bending and stretching modes, with similar representation as for $NaNbO_3$ [95, 96]. The translational modes (**Tr**) arise due to the translational motion of the Na ions against the NbO_6 octahedra. Librational modes (**L**) appear due to the roto-vibrational motion of the oxygen octahedra. These are collectively named as external modes for the ABO_3 type system. The internal modes of the octahedra, namely, the bending (**B**) and stretching (**S**) modes arise due to the bending and stretching motion of the O-Nb-O bonds of the oxygen octahedra.

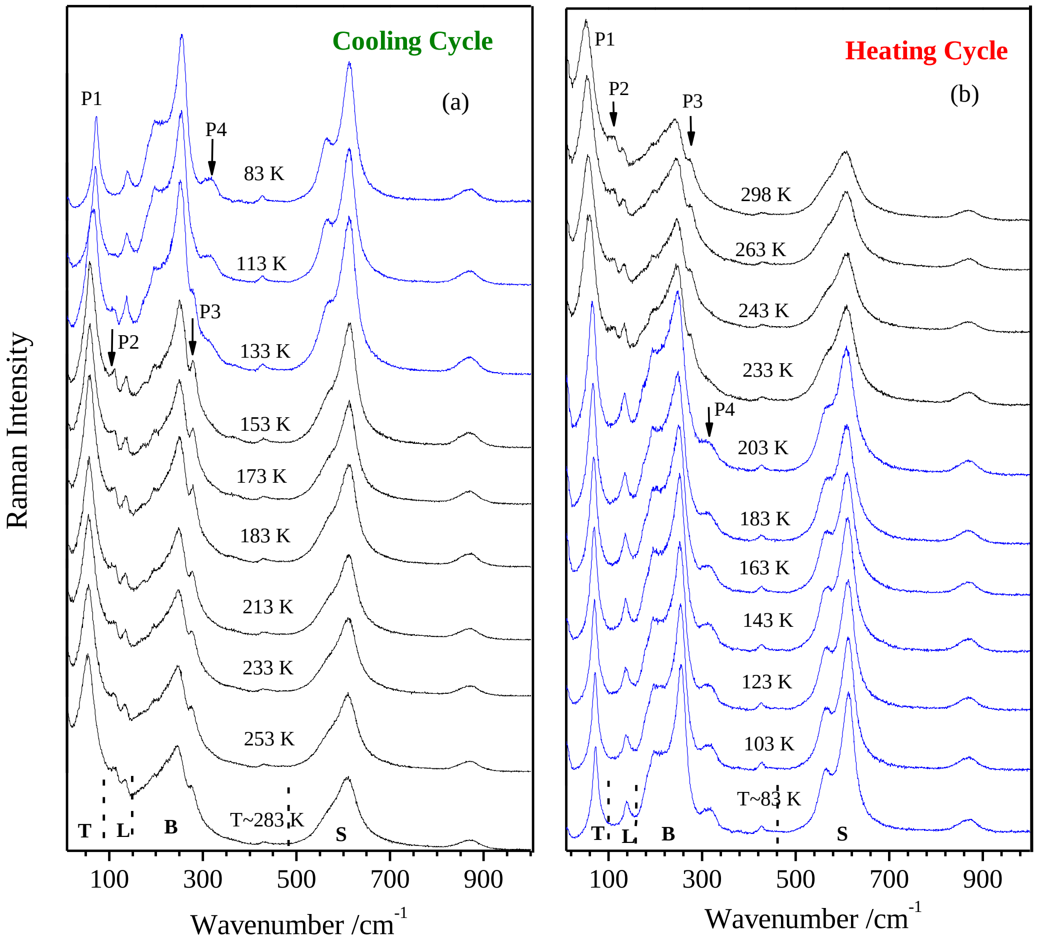

Figure 6.1 Evolution of the Raman spectra collected at various temperatures for NNBT05 in (a) cooling and (b) heating cycles. The main changes appear in the peaks P1, P2, P3 and P4 indicated using arrows.

Figure 6.1 shows the evolution of the low-temperature Raman spectra of NNBT05 at various temperatures in both cooling and heating cycles. The distinct changes in the Raman spectra are observed in the low wavenumber modes of the Raman spectra for T < 133 K in the cooling cycle. The peaks containing the most prominent changes are denoted as P1, P2, P3, and P4. The changes in the behaviour in these peaks could be taken as the signature of phase transition at low temperature. The Raman librational and bending modes around 112.8 (P2) and 277.1 cm^{-1} (P3) respectively, disappear on cooling along with the abrupt shift in the translational band centred at around 58.7 cm^{-1} (P1). It is also observed that on cooling the relative intensity of the Raman band centred at around 318.8 cm^{-1} (P4) increases after the phase transition. Along with these features, the bending mode ~219.6 cm^{-1} mode splits into two modes below 133 K, which may be due to the increased sharpening of the Raman peaks on lowering the temperature. The intensity of the very weak intensity mode ~361.7 cm^{-1} almost disappears on cooling. After cooling the sample to 83 K, Raman spectrum is also measured on heating from 83 K to 298 K. We found that changes as observed in the cooling cycle on cooling below 133 K are also found to recover in the heating cycle above 173 K (Figure 6.1 **(**b)). The changes in the Raman spectra occur at different temperatures in the heating and cooling cycles as in a hysteresis loop, which indicates the first-order nature of the phase transition.

6.2 Group-Theoretical Analysis and Fitting of the Raman Bands

As discussed in previous chapters[93], the structure of the ambient phase of NNBT05 is found to be ferroelectric with orthorhombic symmetry (space group: **$Pmc2_1$**; tilt system: $a^-a^-c^+$) in the X-ray and neutron diffraction study. The standard factor group analysis has been performed for the Raman modes in this structure[94]. The orthorhombic unit cell contains a total of 20 atoms and hence 60 normal modes. Out of these, 57 modes are Raman active (Table 5.2) and represented as $\Gamma_{Raman}=16A_1+13A_2+12B_1+16B_2$. Due to the non-centrosymmetric structure, these Raman active modes are simultaneously IR active except the A_2 mode. However, we could fit only a total of 16 bands to the Raman spectra (Figure 6.2 **(**a**)**)using the standard damped harmonic oscillators (see Equation 2.10). This number is less as compared to the expected number of modes due to the not properly resolved peaks in the experimental Raman spectrum and accidental degeneracy. The low-temperature Raman spectra show completely distinct features of the low-wavenumber Raman modes. The low- temperature neutron diffraction shows that NNBT05 has less symmetric monoclinic structure (Space group: **Cc**; tilt system: $a^-a^-c^-$)[4]. The primitive cell contains total 10 atoms and hence total 30 normal modes. The group-theoretical analysis suggests total 27 Raman active modes (Table 6.1) represented as Γ_{Raman}=13A′+14A″. However, only total 15 damped harmonic oscillators (Figure 6.2(b)) could be fitted to the Raman spectra. The fitted number of Raman modes and positions are compared (Table 6.2) with the previously studied[100] $Li_{0.12}Na_{0.88}NbO_3$ and NNBT03, which have **Pmc2$_1$** Phase at room temperature (300 K).

Table 6.1 Atomic site symmetries and normal mode analysis performed for NNBT05 for the monoclinic phase with space group **Cc**.

Atoms	**Wyckoff Site**	**Position**	**Site sym.**	**Irreducible Representations**
(Na/Ba)	4a	(0+u, ¼+v,0+w)	C_s	3A′+3A″
Nb/Ti	4a	(¼+u,¼+v, ¾+w)	C_s	3A′+3A″
O1	4a	(0+u, ¼+v,½+w)	C_s	3A′+3A″
O2	4a	(¼+u, ½+v, 0+w)	C_s	3A′+3A″
O3	4a	(¼+u,0+v, 0+w)	C_s	3A′+3A″

Γ_{Total}= 15A′+15A″
$\Gamma_{Acoustic}$= 2A′+A″
Γ_{Optic}= 13A′+14A″
Γ_{IR}= 13A′+14A″
Γ_{Raman}= 13A′+14A″

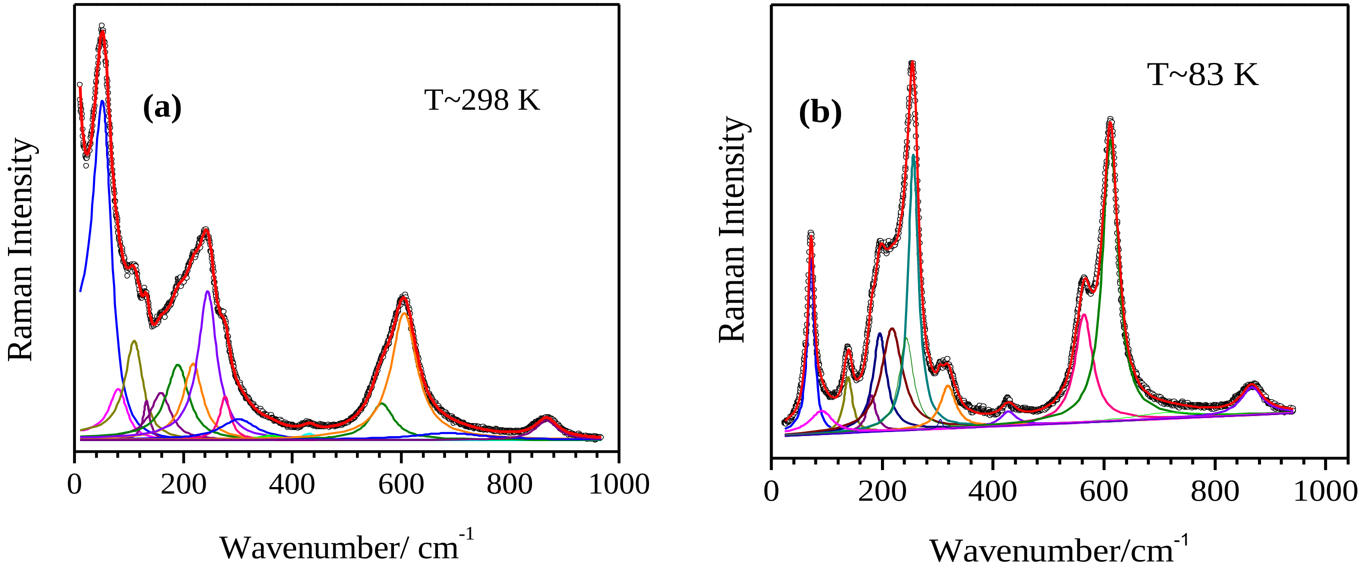

Figure 6.2 Fitting of Raman spectroscopy data of modified sodium niobate NNBT05 at room temperature (a) and T~83 K (b). Open circles (black) and solid line (red) represent the observed and fitted profile of the Raman spectra respectively**.**

Table 6.2 Comparison of the Raman band positions (cm^{-1}) observed in the heating cycle of the present study for NNBTx with the reported data of the $Li_{0.12}Na_{0.88}NbO_3$ in previous studies. The assignment of the modes has been made following the literature for vibrations of isolated equilateral NbO_6 octahedra in the perovskite lattice structures.

$Li_{0.12}Na_{0.88}NbO_3$[100] Pmc2$_1$ Phase (300 K)	**NNBT03[6] Pmc2$_1$ Phase (300 K)**	**Present Study**		
		NNBT05 (T~298 K)	**NNBT05 (T~83 K)**	**Assignment**
	62.6	58.7	72.2	Na^+
81	74.4	84.8	95.1	
120.1	116.5	112.8	----	NbO_6^{-}libration
149.1	137.2	132.7	138.9	
	173.7	161.2	180.5	υ_6 (F_{2u})
194	195.9	192.4	196.2	
226	222.8	219.6	218.9	υ_5 (F_{2g})
	----	----	243.2	
254	249.4	245.9	256.3	
285.4	279.2	277.1		
	308.8	305.7*	304	
	359.3	361.7*	318.8	υ_4 (F_{1u})
436.7	435.8	431.6	427.7	
564.9	568.6	565.05	564.1	υ_2 (E_g)
618.4	611.2	606.4	611.7	υ_1 (A_{1g})
	669.2	691.0*	717.4*	υ_3 (F_{1u})
	780.5			
873	869.9	867.4	866.7	$\upsilon_5 + \upsilon_1$

*Very weak.

6.3 Discussion

The positions of the fitted Raman bands are shown in **Figure** 6.3. It is found from the fitting of the Raman bands that on cooling, the width and the position of the Raman band at the lowest wavenumber ~58.7 cm^{-1} (P1) changes abruptly at the lowest temperature.

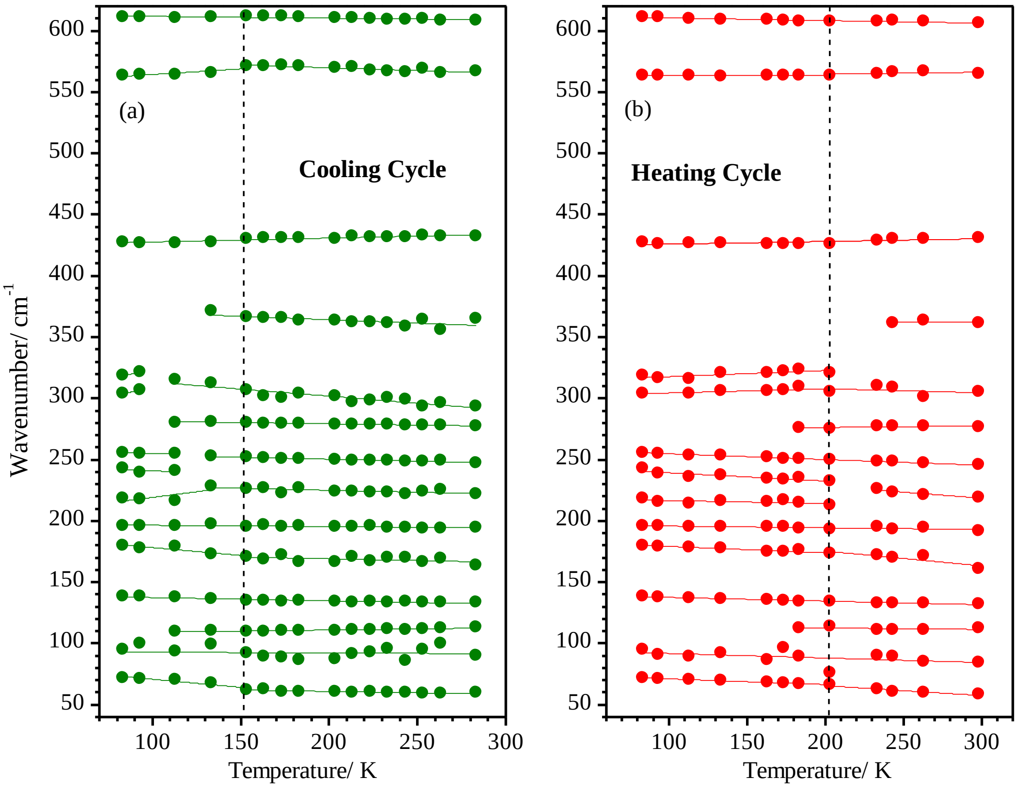

Figure 6.3 Raman shift (wavenumber) vs. temperature (93<T<300K) plot for (a) cooling and (b) heating cycles for NNBT05 solid solution. The vertical dashed lines indicate the phase transition temperatures in the heating and cooling cycles. The data points are linearly fitted.

This mode is the main translational mode arising due to the motion of the A-type atom (Na/Ba) against the BO$_6$ oxygen octahedra[95]. We also find an abrupt increase in the Raman bandwidth of the P1 band in the heating cycle, which is a clear indication of the splitting of the P1 band into two unresolved modes [Figure 6.4]. This feature may be related to the splitting of the Wyckoff site of the A-type atom, because in the room temperature orthorhombic phase (Space group: **Pmc2$_1$**) there are two distinct sites of the A-type atoms. However, the low-temperature phase has only one A-type atom. The shift of the centre of this Raman band as a function of temperature in the heating and cooling cycles is shown in Figure 6.5.

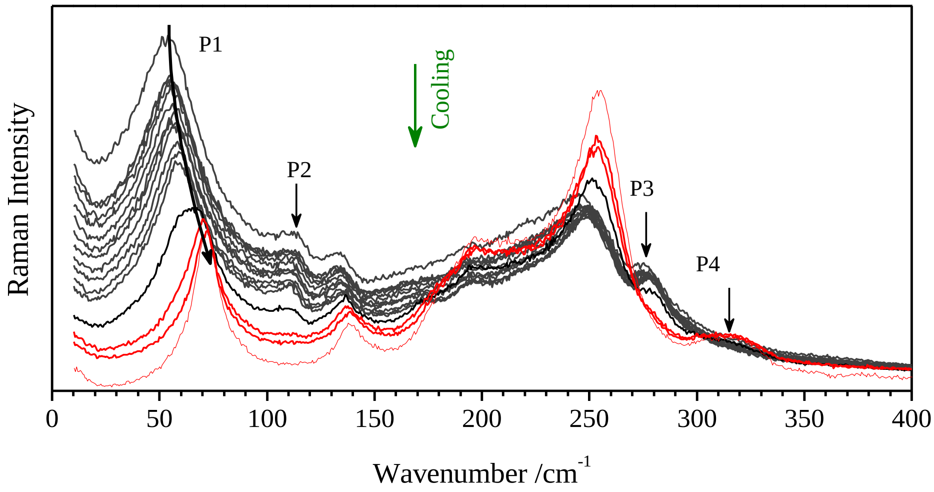

Figure 6.4 A qualitative representations of the changes that appear in the P1, P2, P3 and P4 Raman bands near the phase transition in the cooling cycle.

The peak position shows discontinuity at different temperatures with thermal hysteresis in the heating and cooling cycle due to the first-order nature of the phase transition. The Raman band at around 112.8 cm^{-1} (P2) belongs to the librational modes. It is observed that the relative intensity of this mode decreases on cooling and it disappears at the lowest temperature [Figure 6.4]. The Raman band P2 is the same librational mode[95] which disappears in the low-temperature phase transition in $NaNbO_3$ when the structure transforms from antiferroelectric orthorhombic phase (space group: **Pbcm**) to ferroelectric rhombohedral (space group: **R3c**) phase. The disappearance of this P2 mode indicates the suppression of the in-phase tilting of the oxygen octahedra[89].

We note that interesting changes also appear in the intensity of the Raman band P3 and P4. These bands belong to the internal modes of the oxygen octahedra and arise due to bending motion [Figure 6.4]. The P3 band disappears and the P4 band gains intensity during the phase transition. These bending modes of the internal octahedra are sensitive to the environment inside the oxygen octahedra, i.e. the changes in the position of the B cation inside the octahedral cage due to the ferro-distortions in the structure.

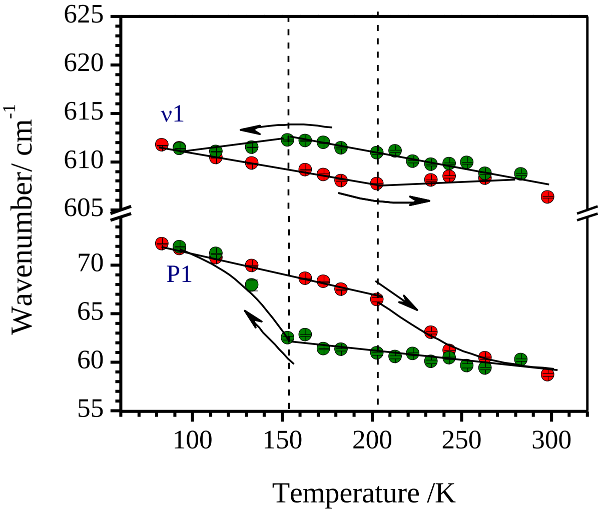

Figure 6.5 Variation of the peak positions of the P1 and ν1 Raman bands in heating (Red circles) and cooling cycles (Green circles). The solid lines are guide to eye.

Figure 6.6 shows a qualitative representation of the changes occurring in the stretching modes of the oxygen octahedra. These modes arise due to the stretching motion of the Nb-O bonds inside the NbO_6 octahedra. It is evident from the data that there is an anomalous change in the position of the main stretching Raman band ν_1 in the cooling cycle. Figure 6.5 shows the variation of the peak position of this $\nu_1$band in heating and cooling cycles. First the band wavenumber increases with decrease in temperature then at ~153 K, it shows redshift in the cooling cycle. Similar anomalous changes are observed in the cooling cycle at ~203 K, where, first the band wavenumber decreases and then shows blueshift. These trends clearly show that there is hardening of this ν_1 band during the phase transition at low temperature. Figure 6.7 shows the variation of the damping constant of the main stretching band ν_1 as a function of temperature during the phase transition at low temperature. The damping constant shows the normal behaviour of increasing with temperature, which corresponds to the decrease in the phonon lifetime on increasing the temperature.

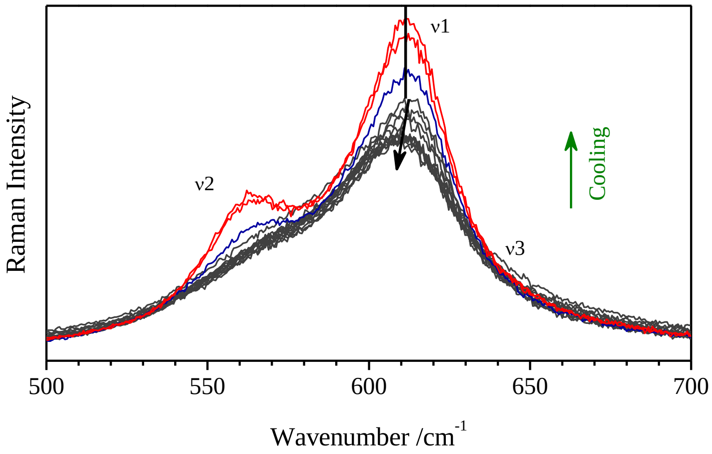

Figure 6.6 A qualitative representations of changes that appear in the stretching bands ν_1, ν_2 and ν_3 near the phase transition in the cooling cycle.

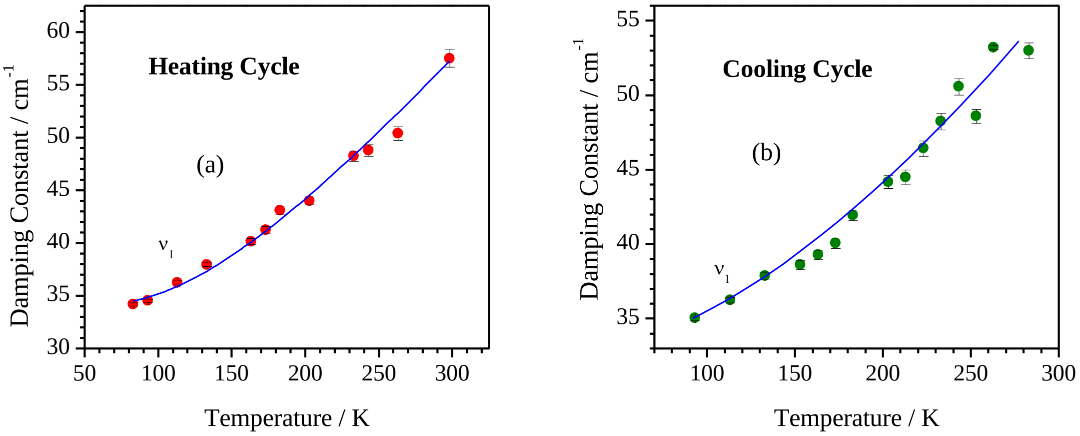

Figure 6.7 Variation of the damping constant of the main stretching band ν_1 Raman bands in (a) heating (Red circles) and (b) cooling (Green circles) cycle during phase transition at low temperature. The blue lines are guide to eye.

6.4 Conclusion

In summary[7], the detailed low-temperature Raman spectroscopy experiment has been performed for the identification of the involvement of phonons during the structural phase transition for NNBT05. The Raman bands at wavenumber ~112.8 and 277.1 cm^{-1} disappear at low temperature during phase transition. Further, the bending mode ~219.6 cm^{-1} mode splits into two modes below 133 K, which may be due to the increased sharpening of the Raman peaks on lowering the temperature. The variation in the peak positions of the main translational and stretching band at 58.7 and 606.4 cm^{-1} respectively as a function of temperature showed hysteresis behaviour. This hysteresis behaviour provides direct evidence of the first-order phase transition at low temperature for the modified sodium niobate NNBT05.

NOMENCLATURE

Abbreviations:

MPB	Morphotropic Phase Boundary
PPB	Polymorphic Phase Boundary
PZT	Lead (Pb) Zirconate Titanate
KNN	Potessium Sodium Niobate
XRD	X-Ray diffraction
NBT	Sodium Bismusth Titanate
KBT	Potessium Bismuth Titanate
BT	Barium Titanate
LO	Longitudinal Optic
TO	Transverse Optic
LST	Lyddane-Sachs-Teller Relation
CZ	Calcium Zirconate
BCT	Barium Calcium Titanate
BZT	Barium Zirconate Titanate
PSD	Position Sensitive Detectors
AP	Acoustic Phonons
OP	Optic Phonons
FE	Ferroelectric
AFE	Antiferroelectric
LNN	Lithium Sodium Niobate
DFT	Density Functional Theory
PNR	Polar Nano Regions
PD2	Powder Diffractometer 2
PVA	Poly Vinyl Alcohol
PZN	Lead Zirconate Niobate
PMN	Lead Magnisium Niobate
AFD	Antiferrodistortive

Tr	Translation Modes
L	Libration Modes
S	Stretching Modes
B	Bending Modes

Symbols:

d_{33}	Piezoelectric Coefficient (pC/N)
E_C	Coercive Field (kV/cm)
P_R	Residual Polarization (μC/cm^2)
P_s	Spontaneous Polarization (μC/cm^2)
Q_{33}	Electrostriction Coefficient (m^4/C^2)
k_p	Electromechanical Coupling Coefficient (%)
E_i, E_f	Initial and final energies
k_i,k_f	Initial and final momentum
d_{33}	Piezoelectric Coefficient (pC/N)
E_C	Coercive Field (kV/cm)
P_R	Residual Polarization (μC/cm2)
Ps	Spontaneous Polarization (μC/cm2)
Q_{33}	Electrostriction Coefficient (m4/C2)
k_p	Electromechanical Coupling Coefficient (%)
ε'	Dielectric Constant
T_C	Critical Temperature (K)
E_i, E_f	Initial and final energies
$\bar{k}_i,\ \bar{k}_f$	Initial and final momentum of radiation
$\bar{q}$	Phonon momentum
$\bar{k}_s,\ \bar{k}_0$	Momentum of scattered and incident light
$\bar{Q}$	Scattering Vector
x	Mole fraction
a_p,b_p, c_p	Pseudocubic Lattice Parameters
V_P	Pseudocubic Volume
a,b, c	Lattice Parameters

Γ	Damping Constant
ω	Wavenumber
A	Amplitude
h	Plank Constant
c	Speed of light
λ	Wavelength
k	Boltzmann Constant
T	Temperature
C	Curie constant

REFERENCES

[1] R.J. Tilley, Perovskites: structure-property relationships, John Wiley & Sons, 2016.

[2] S. Priya, S. Nahm, Lead-free piezoelectrics, Springer Science & Business Media, 2011.

[3] M. Jauhari, S. Mishra, R. Mittal, P. Sastry, S. Chaplot, Physical Review Materials, 1 (2017) 074411.

[4] S. Mishra, M. Jauhari, R. Mittal, P. Krishna, V. Reddy, S. Chaplot, Applied Physics Letters, 112 (2018) 182905.

[5] D. Pandey, A.K. Singh, S. Baik, Acta Crystallographica Section A: Foundations of Crystallography, 64 (2008) 192-203.

[6] M. Jauhari, S.K. Mishra, R. Mittal, S.L. Chaplot, 50 (2019) 1177-1185.

[7] M. Jauhari, S.K. Mishra, H.K. Poswal, R. Mittal, S.L. Chaplot, Journal of Raman Spectroscopy, 50 (2019) 1949-1955.

[8] M.E. Lines, A.M. Glass, Principles and applications of ferroelectrics and related materials, Oxford university press, 2001.

[9] G.A. Samara, Ferroelectricity revisited—advances in materials and physics, in: Solid State Physics, Elsevier, 2001, pp. 239-458.

[10] T. Zheng, J. Wu, D. Xiao, J. Zhu, Progress in Materials Science, 98 (2018) 552-624.

[11] A.J. Moulson, J.M. Herbert, Electroceramics: materials, properties, applications, John Wiley & Sons, 2003.

[12] J. Scott, science, 315 (2007) 954-959.

[13] J.F. Scott, Ferroelectric memories, Springer Science & Business Media, 2013.

[14] C.-H. Hong, H.-P. Kim, B.-Y. Choi, H.-S. Han, J.S. Son, C.W. Ahn, W. Jo, Journal of Materiomics, 2 (2016) 1-24.

[15] B. Jaffe, Piezoelectric ceramics, Elsevier, 2012.

[16] Y. Saito, H. Takao, T. Tani, T. Nonoyama, K. Takatori, T. Homma, T. Nagaya, M. Nakamura, Nature, 432 (2004) 84-87.

[17] S. Zhang, R. Xia, T.R. Shrout, Lead-free piezoelectric ceramics vs. PZT?, in: 2006 15th ieee international symposium on the applications of ferroelectrics, IEEE, 2006, pp. 201-207.

[18] Z.-G. Ye, Handbook of advanced dielectric, piezoelectric and ferroelectric materials: Synthesis, properties and applications, Elsevier, 2008.

[19] M. Deluca, H. Fukumura, N. Tonari, C. Capiani, N. Hasuike, K. Kisoda, C. Galassi, H. Harima, Journal of Raman Spectroscopy, 42 (2011) 488-495.

[20] J. Rödel, W. Jo, K.T. Seifert, E.M. Anton, T. Granzow, D. Damjanovic, Journal of the American Ceramic Society, 92 (2009) 1153-1177.

[21] M.D. Maeder, D. Damjanovic, N. Setter, Journal of Electroceramics, 13 (2004) 385-392.

[22] H. Ghayour, M. Abdellahi, Powder technology, 292 (2016) 84-93.

[23] J. Rödel, K.G. Webber, R. Dittmer, W. Jo, M. Kimura, D. Damjanovic, Journal of the European Ceramic Society, 35 (2015) 1659-1681.

[24] D. DAMJANOVIC, N. KLEIN, J. LI, V. POROKHONSKYY, Functional Materials Letters, 03 (2010) 5-13.

[25] X. Tian, Z. Wu, Y. Jia, J. Chen, R. Zheng, Y. Zhang, H. Luo, Applied Physics Letters, 102 (2013) 042907.

[26] A.V. Ulinzheyev, O.E. Fesenko, V.G. Smotrakov, Ferroelectrics Letters Section, 12 (1990) 17-21.

[27] R.S. Solanki, S.K. Mishra, A. Senyshyn, S. Yoon, S. Baik, N. Shin, D. Pandey, Applied Physics Letters, 102 (2013) 052903.

[28] L. Cross, R. Newnham, Ceramics and Civilization, 3 (1987) 289-305.

[29] U. Müller, Symmetry relationships between crystal structures: applications of crystallographic group theory in crystal chemistry, OUP Oxford, 2013.

[30] R. Blinc, Ferroelectrics, 74 (1987) 301-303.

[31] K.M. RABE, AHN, Charles, TRISCONE, Jean-Marc, Physics of ferroelectrics : a modern perspective., Springer, Berlin 2007.

[32] A. Glazer, Acta Crystallographica Section B, 28 (1972) 3384-3392.

[33] S.K. Mishra, R. Mittal, V.Y. Pomjakushin, S.L. Chaplot, Physical Review B, 83 (2011) 134105.

[34] T. Riste, E.J. Samuelsen, K. Otnes, J. Feder, Solid State Communications, 9 (1971) 1455-1458.

[35] D. Wang, R.J. Angel, Acta Crystallographica Section B, 67 (2011) 302-314.

[36] M. Towler, R. Dovesi, V.R. Saunders, Physical Review B, 52 (1995) 10150.

[37] H.T. Stokes, E.H. Kisi, D.M. Hatch, C.J. Howard, Acta Crystallographica Section B, 58 (2002) 934-938.

[38] S.K. Mishra, M.K. Gupta, R. Mittal, M. Zbiri, S. Rols, H. Schober, S.L. Chaplot, Physical Review B, 89 (2014) 184303.

[39] M.T. Dove, American Mineralogist, 82 (1997) 213-244.

[40] M.T. Dove, Introduction to lattice dynamics, Cambridge university press, 1993.

[41] A. Bratkovsky, V. Heine, E.K.H. Salje, Philosophical Transactions of the Royal Society of London. Series A: Mathematical, Physical and Engineering Sciences, 354 (1996) 2875-2896.

[42] E. Salje, Ferroelectrics, 104 (1990) 111-120.

[43] E.K.H. Salje, S.A. Hayward, W.T. Lee, Acta Crystallographica Section A, 61 (2005) 3-18.

[44] M. Ahart, M. Somayazulu, R. Cohen, P. Ganesh, P. Dera, H.-k. Mao, R.J. Hemley, Y. Ren, P. Liermann, Z. Wu, Nature, 451 (2008) 545.

[45] P. Panda, B. Sahoo, Ferroelectrics, 474 (2015) 128-143.

[46] T. Takenaka, K.-i. Maruyama, K. Sakata, Japanese journal of applied physics, 30 (1991) 2236.

[47] E. Hollenstein, M. Davis, D. Damjanovic, N. Setter, Applied Physics Letters, 87 (2005) 182905.

[48] J. Wu, D. Xiao, J. Zhu, Chemical reviews, 115 (2015) 2559-2595.

[49] H. Birol, D. Damjanovic, N. Setter, Journal of the European Ceramic Society, 26 (2006) 861-866.

[50] Y. Hiruma, H. Nagata, T. Takenaka, Journal of Applied Physics, 104 (2008) 124106.

[51] W. Liu, X. Ren, Physical Review Letters, 103 (2009) 257602.

[52] S. Lanfredi, M.H. Lente, J.A. Eiras, Applied Physics Letters, 80 (2002) 2731-2733.

[53] H.D. Megaw, Ferroelectrics, 7 (1974) 87-89.

[54] S.K. Mishra, N. Choudhury, S.L. Chaplot, P.S.R. Krishna, R. Mittal, Physical Review B, 76 (2007) 024110.

[55] S.K. Mishra, M.K. Gupta, R. Mittal, S.L. Chaplot, T. Hansen, Applied Physics Letters, 101 (2012) 242907.

[56] J. Macutkevic, A. Molak, J. Banys, Ferroelectrics, 479 (2015) 48-55.

[57] P. Kumari, R. Rai, S. Sharma, M. Shandilya, A. Tiwari, Adv. Mater. Lett, 6 (2015) 453-484.

[58] J.T. Zeng, K.W. Kwok, H.L.W. Chan, Journal of the American Ceramic Society, 89 (2006) 2828-2832.

[59] I.P. Raevskii, L.M. Proskuryakova, L.A. Reznichenko, E.K. Zvorykina, L.A. Shilkina, Soviet Physics Journal, 21 (1978) 259-261.

[60] S. Xie, K. Zhu, J. Qiu, H. Guo, Frontiers of Mechanical Engineering in China, 4 (2009) 345-349.

[61] R. Aoyagi, M. Iwata, M. Maeda, Dielectric and Piezoelectric Properties of (Na, Ba)(Nb, Ti) O3 Lead-Free Piezoelectric Ceramics, in: Key Engineering Materials, Trans Tech Publ, 2010, pp. 55-58., R. Aoyagi *et al.*, Piezoelectric Properties of NaNbO3-BaTiO3 Ceramics, 2007 Sixteenth IEEE International Symposium on the Applications of Ferroelectrics, DOI: 10.1109/ISAF.2007.4393365

[62] R. Zuo, H. Qi, J. Fu, J. Li, M. Shi, Y. Xu, Applied Physics Letters, 108 (2016) 232904.

[63] R. Zuo, H. Qi, J. Fu, Applied Physics Letters, 109 (2016) 022902.

[64] H. Qi, H. Zhang, R. Zuo, Journal of the American Ceramic Society, 100 (2017) 3990-3998.

[65] X. Lu, L. Hou, L. Jin, L. Wang, Y. Tian, K. Yu, Q. Hu, L. Zhang, X. Wei, Ceramics International, 44 (2018) 5492-5499.

[66] D.S. Sivia, Elementary scattering theory: for X-ray and neutron users, Oxford University Press, 2011.

[67] J. Als-Nielsen, D. McMorrow, Elements of modern X-ray physics, John Wiley & Sons, 2011.

[68] B.T.M. Willis, C.J. Carlile, Experimental neutron scattering, Oxford University Press, 2017.

[69] R.A. Young, The rietveld method, International union of crystallography, 1993.

[70] J. Rodríguez-Carvajal, CEA/Saclay, France, (2001).

[71] J. Toulouse, F. Jiang, O. Svitelskiy, W. Chen, Z.G. Ye, Physical Review B, 72 (2005) 184106.

[72] J.F. Scott, Science, 315 (2007) 954.

[73] M. Fujimoto, The Physics of Structural Phase Transitions, Springer New York, NY, 2005.

[74] A. Ulrich, A.S. Nicola, Journal of Physics: Condensed Matter, 26 (2014) 122203.

[75] A.I. Mohammad, M.R. James, E.S. Jonathan, Journal of Physics: Condensed Matter, 25 (2013) 175902.

[76] S.F. Yuk, K.C. Pitike, S.M. Nakhmanson, M. Eisenbach, Y.W. Li, V.R. Cooper, Scientific Reports, 7 (2017) 43482.

[77] J. Hong, D. Vanderbilt, Physical Review B, 87 (2013) 064104.

[78] W. Zhong, D. Vanderbilt, Physical Review Letters, 74 (1995) 2587-2590.

[79] R. Zuo, H. Qi, J. Fu, J.-F. Li, L. Li, Applied Physics Letters, 111 (2017) 132901.

[80] A.D. Bruce, R.A. Cowley, Structural phase transitions, Taylor & Francis, 1981.

[81] S.K. Mishra, A.B. Shinde, P.S.R. Krishna, Journal of Applied Physics, 115 (2014) 174104.

[82] S.K. Mishra, P.S.R. Krishna, A.B. Shinde, V.B. Jayakrishnan, R. Mittal, P.U. Sastry, S.L. Chaplot, Journal of Applied Physics, 118 (2015) 094101.

[83] F. Li, S. Zhang, T. Yang, Z. Xu, N. Zhang, G. Liu, J. Wang, J. Wang, Z. Cheng, Z.-G. Ye, J. Luo, T.R. Shrout, L.-Q. Chen, Nature Communications, 7 (2016) 13807.

[84] R.A. Shakhovoy, S.I. Raevskaya, L.A. Shakhovaya, D.V. Suzdalev, I.P. Raevski, Y.I. Yuzyuk, A.F. Semenchev, M. El Marssi, Journal of Raman Spectroscopy, 43 (2012) 1141-1145.

[85] Z.X. Shen, X.B. Wang, M.H. Kuok, S.H. Tang, Journal of Raman Spectroscopy, 29 (1998) 379-384.

[86] Z.X. Shen, X.B. Wang, S.H. Tang, M.H. Kuok, R. Malekfar, Journal of Raman Spectroscopy, 31 (2000) 439-443.

[87] R.J.C. Lima, P.T.C. Freire, J.M. Sasaki, A.P. Ayala, F.E.A. Melo, J. Mendes Filho, K.C. Serra, S. Lanfredi, M.H. Lente, J.A. Eiras, Journal of Raman Spectroscopy, 33 (2002) 669-674.

[88] R.J.C. Lima, W. Paraguassu, P.T.C. Freire, J.M. Sasaki, F.E.A. Melo, J. Mendes Filho, S. Lanfredi, Journal of Raman Spectroscopy, 36 (2005) 28-32.

[89] K.K. Mishra, V. Sivasubramanian, A.K. Arora, Journal of Raman Spectroscopy, 42 (2011) 517-521.

[90] S.J. Lin, D.P. Chiang, Y.F. Chen, C.H. Peng, H.T. Liu, J.K. Mei, W.S. Tse, T.R. Tsai, H.P. Chiang, Journal of Raman Spectroscopy, 37 (2006) 1442-1446.

[91] P. Colomban, Francois Romain, A. Neiman, I. Animitsa, Solid State Ionics, 145 (2001) 339-347.

[92] A. Slodczy, P. Colomban, Materials, 3 (2010) 5007-5028.

[93] M. Jauhari, S.K. Mishra, R. Mittal, P.U. Sastry, S.L. Chaplot, Physical Review Materials, 1 (2017) 074411.

[94] E. Kroumova, M.I. Aroyo, J.M. Perez-Mato, A. Kirov, C. Capillas, S. Ivantchev, H. Wondratschek, Phase Transitions, 76 (2003) 155-170.

[95] Y. Shiratori, A. Magrez, W. Fischer, C. Pithan, R. Waser, The Journal of Physical Chemistry C, 111 (2007) 18493-18502.

[96] Y. Shiratori, A. Magrez, J. Dornseiffer, F.-H. Haegel, C. Pithan, R. Waser, The Journal of Physical Chemistry B, 109 (2005) 20122-20130.

[97] E. Bouziane, M.D. Fontana, M. Ayadi, Journal of Physics: Condensed Matter, 15 (2003) 1387.

[98] Y. Shiratori, A. Magrez, M. Kato, K. Kasezawa, C. Pithan, R. Waser, The Journal of Physical Chemistry C, 112 (2008) 9610-9616.

[99] Y.D. Juang, S.B. Dai, Y.C. Wang, J.S. Hwang, M.L. Hu, W.S. Tse, Journal of Applied Physics, 88 (2000) 742-745.

[100] P.S.R. Krishna, S.K. Mishra, A.B. Shinde, S. Kesari, R. Rao, Ferroelectrics, 510 (2017) 34-42.

[101] A. Slodczyk, P. Colomban, Materials, 3 (2010) 5007-5028.

[102] N. Zhang, H. Yokota, M. Glazer, D. A. Keen, S. Gorfman, P. Thomas, W. Ren, Z.-G. Ye, Local-scale structures across the morphotropic phase boundary in PbZr 1− x Ti x O 3, 2018.

[103] G. Gouadec, P. Colomban, A. Slodczyk, M. Pham Thi, Stress and temperature driven phase transitions in single crystalline KNbO3 and textured KNL-NTS ceramics: A Raman andthermal expansion study, 2014.

[104] A. Filho, K. Lima, A. Ayala, I. Guedes, P. Freire, J. Filho, E. Araujo, J. Eiras, Monoclinic phase of PbZr0.52Ti0.48O3 ceramics: Raman and phenomenological thermodynamic studies, 1999.

[105] A.G. Souza Filho, K.C.V. Lima, A.P. Ayala, I. Guedes, P.T.C. Freire, F.E.A. Melo, J. Mendes Filho, E.B. Araújo, J.A. Eiras, Physical Review B, 66 (2002) 132107.

[106] J. Cheng, Y. Yang, Y.-H. Tong, S.-B. Lu, J.-Y. Sun, K. Zhu, Y.-L. Liu, G.G. Siu, Z.K. Xu, Journal of Applied Physics, 105 (2009) 053519.

[107] P. Colomban, F. Romain, A. Neiman, I. Animitsa, Solid State Ionics, 145 (2001) 339-347.

Chapter 7: Conclusion and Future Work

This chapter provides the summary and conclusion of the present work. Recommendations for future work are also described.

7.1 Conclusion

We have studied the structural phase transitions and phonon anomalies in the lead- free alkaline niobate based piezoelectric solid solutions NNBTx as a function of composition (x=0 to 0.15) and temperature. Phase transitions were studied using powder X-ray and neutron diffraction, dielectric, ferroelectric measurements, and Raman spectroscopy.

The main conclusions are:

1. The solid solutions of $NaNbO_3$ and $BaTiO_3$: NNBTx are synthesized for the composition range x=0.0 to 0.20 using solid-state reaction method.
2. The X-ray diffraction study shows that the phase transitions involve change in the tilting patterns of the oxygen octahedra and cationic displacements. The signature of these changes was reflected in the diffractogram in terms of appearance and/or disappearance of superlattice (additional) reflections and the splitting of the main perovskite peaks.
3. The crystal structure and sequence of phase transitions as a function of composition were identified using the X-ray, neutron diffraction and Raman spectroscopy studies. On increasing the concentration of $BaTiO_3$ in the antiferroelectric $NaNbO_3$ matrix, we observed two ferroelectric phases get stabilized at x~0.03 and x~0.10. These have orthorhombic structures with space group **$Pmc2_1$** and **Amm2**.

4. It is observed that the suppression of in-phase rotation of octahedra and increment in tetragonality (c/a ratio) promotes polar mode with the increment of concentration of

$BaTiO_3$. The slight variation in composition in NNBTx around x=0.03 dramatically changes the phase transition behavior (antiferroelectric to ferroelectric) and its underlying physics in term of the phonon softening and the Gibbs free energy variations.

5. The ferroelectric compounds NNBT03 and 05 are characterized as a function of temperature using X-ray and neutron diffraction studies. The NNBT03 shows a total five structural phase transitions in the temperature range 12 K to 900 K in X-ray diffraction study.
6. The low-temperature phase of NNBT03 and 05 compounds is found to be monoclinic with space group **Cc**. The neutron diffraction studies of NNBT05 provided the evidence of stabilization of functional monoclinic (**Cc**) phase. This functional monoclinic phase is believed to provide exceptionally good electromechanical performance due to easy polarization rotation in various lead-based piezo-ceramics.
7. The structural phase transitions as a function of composition is also studied by Raman spectroscopic technique. Some characteristic antiferroelectric modes were found to disappear during the phase transition at x>0.02. The change in the slope of the wavenumber shift and damping constant of specific Raman bands also indicated another phase transition as a function of composition at x>0.07. The Raman spectroscopic results are found to be consistent with the X-ray diffraction studies.
8. The evidence of low-temperature phase transition in NNBT05 was also provided using Raman spectroscopic technique. The thermal hysteresis found in the specific Raman band positions provided the evidence of the first-order nature of the phase transition at low temperature.

7.2 Recommendation for Future Work

The Recommendation for future work is as follows:

1. It is interesting to investigate the nature of phase transitions and phase stability for the extended range of composition x>0.20.
2. The studies of structural phase transitions of the similar kind of solid solutions are very important to understand the underlying physics of high electromechanical response of these materials. This understanding opens the door for the discovery of new generation high-performance materials for direct applications in future technology.
3. These compounds undergo a complex sequence of phase transitions with temperature. To identify the structure of these compositions, a high-resolution powder X-ray (synchrotron) and neutron diffraction is highly recommended.

SUMMARY

Piezoelectric materials are used to convert the mechanical energy into electrical energy and vice versa in various devices, which are applicable in day to day life[1]. Most of the piezoelectric materials used for technological applications contain lead (Pb), which is a toxic element[2]. In search of high-performance lead-free and environment-friendly piezoelectric materials, we compositionally designed (1-x)$NaNbO_3$-x$BaTiO_3$: NNBTx solid solution, which can induce inter-ferroelectric instabilities leading to morphotropic phase boundaries (MPBs) near room temperature.

The physics of perovskite oxides and their functional properties are governed by lattice distortions. We have synthesized solid solution of NNBTx for various composition ($0.0 \leq x < 0.20$) using a conventional solid-state reaction method. Using a combination of dielectric and powder x-ray diffraction studies, it is observed that on the increment of $BaTiO_3$ concentration in $NaNbO_3$ matrix, the parent antiferroelectric orthorhombic **AFE** phase (with space group **Pbcm**) of $NaNbO_3$ is destabilized and it transforms into a ferroelectric orthorhombic phase with space group **Pmc2$_1$** (**FE1**) at x>0.02. The further increase in the doping concentration x~0.10, the structure transforms into another ferroelectric orthorhombic phase with space group **Amm2** (**FE2**). The increase in dielectric constant was observed with the increment in the doping concentration[3]. It is found that as the doping concentration of $BaTiO_3$ in the $NaNbO_3$ matrix increases, the strain developed due to chemical pressure initiates electric dipoles to align in a ferroelectric manner. We have also studied the changes in the sequence of structural phase transitions as a function of temperature for NNBTx (x=0.03 and 0.05) solid solutions[3]. The stabilization of functional monoclinic phase (with space group **Cc)** of NNBTx (x=0.03 and 0.05) at low temperature was confirmed at the lowest temperature using x-ray and neutron

diffraction studies[3, 4]. This monoclinic phase is believed to provide for a flexible polarization rotation[5]. The coexistence of room temperature orthorhombic phase and low-temperature monoclinic phase in a wide temperature range evident that the structural phase transition from orthorhombic to monoclinic phase is of first order.

The structural phase transitions in these compositions are governed by softening of various phonon modes which can be probed using Raman spectroscopy. The Raman spectroscopic measurements were performed to provide a deep insight into the structural phase transitions and the role of phonons on changing the composition and temperature. Raman Spectroscopic measurements as a function of composition for NNBTx (x=0 to 0.20) provided clear evidence of phase transitions in terms of disappearance of some characteristic modes and change in the positions of the Raman bands[6]. The detailed low-temperature Raman spectroscopy experiment for NNBT05 as a function of temperature from 83 K to 298 K, provided evidence of the first-order nature of the phase transition at low temperature[7]. The results of Raman spectroscopic measurements were found to be consistent with the X-ray and neutron diffraction studies.

These assignments of structural phase transitions and phonon anomalies for NNBTx solid solution presented in the thesis are important for the understanding of the good electromechanical performance of lead-free piezo-ceramics.

LIST OF FIGURES

LIST OF TABLES

Thesis Highlight

Name of the student: MRINAL JAUHARI
Name of the CI/OCC: BARC, Mumbai Enrolment No. PHYS01201504026
Thesis Title: Structural phase transitions and phonon anomalies in alkaline niobate based functional materials
Discipline: Physical Sciences Sub-Area of Discipline: Solid State Physics
Date of viva voce: 26/09/2020

In search of high-performance lead-free and environment-friendly piezoelectric materials, we compositionally designed (1-x)$NaNbO_3$-x$BaTiO_3$: NNBTx (0.0 < x < 0.20) solid solution, which can induce inter-ferroelectric instabilities leading to morphotropic phase boundaries (MPBs) near room temperature. Using a combination of dielectric and powder x-ray diffraction studies, it is observed that on the increment of $BaTiO_3$ concentration in $NaNbO_3$ matrix, the parent antiferroelectric orthorhombic **AFE** phase (with space group **Pbcm**) of $NaNbO_3$ is destabilized and it transforms into a ferroelectric orthorhombic phase with space group **Pmc2$_1$** (**FE1**) at x>0.02. The further increase in the doping concentration x~0.10, the structure transforms into another ferroelectric orthorhombic phase with space group **Amm2** (**FE2**). The increase in dielectric constant was observed with the increment in the doping concentration. We have also studied the changes in the sequence of structural phase transitions as a function of temperature for NNBTx (x=0.03 and 0.05) solid solutions. The stabilization of functional monoclinic phase (with space group **Cc)** of NNBTx (x=0.03 and 0.05) at low temperature was confirmed at the lowest temperature using x-ray and neutron diffraction studies. This monoclinic phase is believed to provide for a flexible polarization rotation.

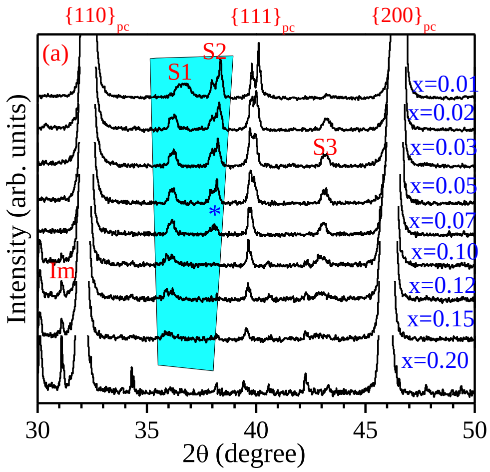

Figure 1 *Evolution of powder X-ray diffraction patterns, with composition at room temperature.*

Raman Spectroscopic measurements as a function of composition for NNBTx (x=0 to 0.20) provided clear evidence of phase transitions in terms of disappearance of some characteristic modes and change in the positions of the Raman bands. The detailed low-temperature Raman spectroscopy experiment for NNBT05 in the temperature range 83 K to 298 K, provided evidence of the first-order nature of the phase transition at low temperature. The results of Raman spectroscopic measurements were found to be consistent with the X-ray and neutron diffraction studies.